

## **NOTE TO USERS**

**This reproduction is the best copy available.**

UMI<sup>®</sup>



UNDERSTANDING THE MECHANICAL PROPERTIES OF NANOTWINNED  
COPPER USING MOLECULAR DYNAMICS SIMULATION

by

Ishraq Shabib

B.Sc., M.A.Sc.

A thesis submitted to

the Faculty of Graduate Studies and Research

in partial fulfillment of the requirements for the degree of

Doctor of Philosophy

Ottawa-Carleton Institute for Mechanical and Aerospace Engineering

Department of Mechanical and Aerospace Engineering

Faculty of Engineering

Carleton University

Ottawa, Ontario

Canada

September 2009

Copyright © Ishraq Shabib 2009



Library and Archives  
Canada

Published Heritage  
Branch

395 Wellington Street  
Ottawa ON K1A 0N4  
Canada

Bibliothèque et  
Archives Canada

Direction du  
Patrimoine de l'édition

395, rue Wellington  
Ottawa ON K1A 0N4  
Canada

*Your file* *Votre référence*  
ISBN: 978-0-494-60119-8  
*Our file* *Notre référence*  
ISBN: 978-0-494-60119-8

**NOTICE:**

The author has granted a non-exclusive license allowing Library and Archives Canada to reproduce, publish, archive, preserve, conserve, communicate to the public by telecommunication or on the Internet, loan, distribute and sell theses worldwide, for commercial or non-commercial purposes, in microform, paper, electronic and/or any other formats.

The author retains copyright ownership and moral rights in this thesis. Neither the thesis nor substantial extracts from it may be printed or otherwise reproduced without the author's permission.

---

In compliance with the Canadian Privacy Act some supporting forms may have been removed from this thesis.

While these forms may be included in the document page count, their removal does not represent any loss of content from the thesis.

**AVIS:**

L'auteur a accordé une licence non exclusive permettant à la Bibliothèque et Archives Canada de reproduire, publier, archiver, sauvegarder, conserver, transmettre au public par télécommunication ou par l'Internet, prêter, distribuer et vendre des thèses partout dans le monde, à des fins commerciales ou autres, sur support microforme, papier, électronique et/ou autres formats.

L'auteur conserve la propriété du droit d'auteur et des droits moraux qui protègent cette thèse. Ni la thèse ni des extraits substantiels de celle-ci ne doivent être imprimés ou autrement reproduits sans son autorisation.

---

Conformément à la loi canadienne sur la protection de la vie privée, quelques formulaires secondaires ont été enlevés de cette thèse.

Bien que ces formulaires aient inclus dans la pagination, il n'y aura aucun contenu manquant.

■ ■ ■  
**Canada**

## ABSTRACT

In this research large scale Molecular Dynamics (MD) simulations have been performed to explore the underlying deformation mechanisms responsible for the observed properties of nanotwinned copper samples under approximately uniaxial tensile load. This research also aims to develop a solid understanding of the influences of twin width, grain size, and temperature on the deformation characteristics and properties of these materials. Observed deformation mechanisms include twin boundary (TB) migration, extended partial and full dislocation emissions from the grain boundaries (GBs) and TB/GB junctions, twinning fault formation, dislocation nucleation from the TB steps, and GB sliding, where the dominance of one mechanism over another is found to be dictated by the planar fault energy densities of various defects. Simulation results have revealed that the TBs act as obstacles to dislocation movements that lead to the strengthening of nanotwinned structures. However, easy glide of dislocations parallel to the TBs contribute primarily to the plastic strain or ductility of these materials. At higher strains, the strengthening effects reach a maximum when abundant dislocations begin crossing the TBs, which causes rapid softening. The strengths of the nanotwinned models are found to exhibit an inverse relationship with the twin width and temperature. Simulation results have shown that a material's toughness can be enhanced by introducing nanotwins within nanocrystalline grains, and the enhancement is more pronounced for the higher twin density structures. At extremely low tem-

perature, toughness values are elevated further due to depressed dislocation activities inside the grains. The deformation behavior in different grains with respect to their orientation has also been investigated, and the nanotwinned grains are found to be highly anisotropic in their plastic response; ductile along TBs but strong across them. A random polycrystalline nanotwinned sample gains strength and toughness through the combined response of variously oriented grains. The study has also revealed that, unlike twin-width refinement, grain-size refinement may not always yield superior properties, and may deteriorate material toughness.

## ACKNOWLEDGMENTS

First of all I want to express my sincere gratitude to the Almighty for giving me the strength, knowledge, and patience to complete this task, which I believe is the most significant accomplishment in my life.

I would like thank my thesis supervisor Professor Ron Miller whose exceptional knowledge in the field of materials science, excellent guidance, and encouragement helped me successfully complete this research. He showed utmost patience in reading and correcting my paper and thesis drafts. I thank him for his constructive criticisms. I am also grateful for his financial support to complete my studies. It is an honor to work with him and to learn so many things in depth.

I also gratefully acknowledge the cooperation that I received from Neil McFadyen in setting up LAMMPS in the department cluster, which helped me tremendously to complete the large scale simulations. I want to give my special thanks to Marlene Groves, Nancy Powell, and Christie Egbert for their administrative support. I would also like to express my gratitude to the Department of Mechanical and Aerospace Engineering and the Faculty of Graduate Studies and Research of Carleton University for the financial support throughout my doctorate program.

I would like to share this moment of happiness with my parents, my sister, and my wife who rendered gargantuan love, encouragement, and moral support throughout my research work. Without their loving support and understand-

ing I would never have completed my work. I hope I will never forget the company I had with Fred Barrett, Bashir Morshed, Alireza Khoddamzadeh, Subray Hegde, Roni Daher, and Fahad Al-Sulaiman. Thank you all for the encouragements, and the moments that we shared together. It is also my pleasure to thank all the Bangladeshi friends in Ottawa for their friendship and hospitality.

To my parents

# Contents

<b>Table of Contents</b>	<b>viii</b>
<b>List of Figures</b>	<b>xi</b>
<b>List of Symbols</b>	<b>xiii</b>
<b>List of Abbreviations</b>	<b>xvii</b>
<b>1 Introduction</b>	<b>1</b>
1.1 Materials at the nanoscale . . . . .	1
1.2 Atomic scale computer simulation . . . . .	5
1.3 Motivation . . . . .	7
1.4 Thesis outline . . . . .	8
<b>2 Literature review</b>	<b>9</b>
2.1 Properties and deformation behavior of materials- from micro to nanoscale	10
2.1.1 Strengthening by grain size refinement . . . . .	10
2.1.2 Inverse Hall-Petch relation . . . . .	13
2.1.3 Ductility . . . . .	18
2.1.4 Effects of temperature . . . . .	18
2.1.5 Strain hardening . . . . .	19
2.2 Nanotwinned structures and changes in properties . . . . .	21
2.3 Deformation behavior of nanotwinned samples-experimental observations	26
2.4 Atomistic simulations . . . . .	29
2.4.1 Stacking fault and generalized stacking fault curve . . . . .	29
2.4.2 Deformation behavior . . . . .	33
2.4.3 Dislocation-twin boundary interaction . . . . .	35
2.5 Analytical models . . . . .	39
2.6 Summary and objectives of this work . . . . .	41
<b>3 Computational approach</b>	<b>43</b>
3.1 Modeling schemes across scales: continuum to atomistic . . . . .	43
3.2 Interatomic potentials . . . . .	45
3.2.1 Embedded atom method (EAM) . . . . .	47

---

3.3	Molecular dynamics (MD) method . . . . .	49
3.3.1	Energy minimization and velocity initialization . . . . .	51
3.3.2	Velocity-Verlet algorithm . . . . .	52
3.3.3	Periodic boundary condition . . . . .	53
3.3.4	Nosé-Hoover thermostat . . . . .	54
3.4	Visualization techniques . . . . .	57
3.4.1	Centrosymmetry parameter (CSP) . . . . .	57
3.4.2	Slip vector (SV) analysis . . . . .	58
3.4.3	Understanding CSP and SV plots . . . . .	58
<b>4</b>	<b>Deformation Behavior and Stress-Strain Response</b>	<b>64</b>
4.1	Model description . . . . .	64
4.2	Grain and twin boundary structure . . . . .	66
4.3	Grain and twin boundary energy calculation . . . . .	68
4.4	Generalized stacking fault energy curve calculation . . . . .	71
4.5	Deformation procedure . . . . .	74
4.6	Deformation behavior of the crystal . . . . .	75
4.6.1	Dislocation nucleation along and across the TBs . . . . .	76
4.6.2	Twinning fault deformation . . . . .	77
4.6.3	Twin boundary migration and change in twin width . . . . .	79
4.6.4	Pile-up and transmission of dislocations across the TBs . . . . .	81
4.6.5	Dislocation nucleation from steps . . . . .	83
4.6.6	Grain boundary sliding and grain rotation . . . . .	84
4.7	Stress calculation . . . . .	85
4.7.1	Stress vs. strain response . . . . .	87
4.7.2	Maximum stress variation with twin width . . . . .	88
4.8	Resolved Shear Stress (RSS) Calculation . . . . .	92
4.8.1	Resolved shear stress (RSS) variations in various grains. . . . .	94
<b>5</b>	<b>Effects of twin width, grain size, and temperature on toughness</b>	<b>98</b>
5.1	Toughness measurement . . . . .	99
5.2	Effects of Twin Width . . . . .	100
5.3	Grain size and twin width refinement . . . . .	103
5.4	Effects of Temperature . . . . .	108
<b>6</b>	<b>Conclusions and Future Recommendations</b>	<b>111</b>
6.1	Summary of conclusions . . . . .	111
6.2	Future work . . . . .	114
<b>A</b>	<b>Conjugate gradient (CG) energy minimization</b>	<b>119</b>
<b>B</b>	<b>Velocity initialization algorithm</b>	<b>121</b>
<b>C</b>	<b>Coincident site lattice (CSL)</b>	<b>123</b>

---

**Bibliography**

**126**

# List of Figures

2.1	The Hall-Petch and inverse Hall-Petch plot for nc Copper samples . . .	12
2.2	Stages of polycrystalline deformation mechanism . . . . .	13
2.3	Inverse Hall-Petch plots for nc palladium and copper . . . . .	14
2.4	Dislocation pile-up inside micro- and nanocrystalline grains . . . . .	15
2.5	Tensile elongation to failure vs. yield strength of various nc metals . .	19
2.6	Temperature and strain rate effect on the strength and ductility . . .	20
2.7	Strain hardening of nc copper in compression and tension . . . . .	21
2.8	Strength and hardness variation with twin width and loading rate . .	24
2.9	TEM images of Cu samples of different twin densities . . . . .	25
2.10	Tensile stress-strain and elongation to failure vs. twin density of Cu .	26
2.11	Electrical resistivity as a function of temperature of various Cu samples	27
2.12	TEM images of nanotwinned Cu sample before and after deformation	28
2.13	Displacement of twin boundaries due to deformation . . . . .	29
2.14	Step, jog formation and dislocation emission from the coherent TBs .	30
2.15	Dislocation loop formation from the twin boundaries . . . . .	31
2.16	Stacking sequence of $\{111\}$ planes of FCC crystals . . . . .	32
2.17	Generalized planar fault curve . . . . .	33
2.18	Twin boundary migration energy density . . . . .	34
2.19	Dislocation nucleation from the TBs . . . . .	35
2.20	The Thompson tetrahedron . . . . .	37
2.21	Interaction of a screw dislocation with coherent TB . . . . .	38
2.22	Absorption, desorption and direction transmission of a screw dislocation	39
2.23	Schematic diagram of the twin boundary affected zone . . . . .	40
3.1	Schematic diagram of the periodic boundary condition . . . . .	54
3.2	Stacking sequence and visualization of a coherent TB . . . . .	60
3.3	Formation mechanism and visualization of an intrinsic stacking fault .	61
3.4	Formation mechanism and visualization of an extrinsic stacking fault	62
3.5	Visualization of a full dislocation . . . . .	63
4.1	Configuration of the Cu nanotwinned model . . . . .	67
4.2	Structure of grain and twin boundary . . . . .	69
4.3	Schematic diagram of a bi-crystal model to calculate TB energy . . .	70

---

4.4	Generalized energy density curves of various defects . . . . .	73
4.5	Dislocation nucleation and propagation along and across the TB . . .	78
4.6	Formation of intrinsic stacking fault and twinning fault . . . . .	80
4.7	Twin boundary migration process and change in twin width . . . . .	82
4.8	Dislocation pile-up and transmission across the TB . . . . .	83
4.9	Dislocation emissions from the steps . . . . .	84
4.10	Relative displacement of the center of mass (COM) over time . . . . .	86
4.11	Stress vs. strain response of various nanotwinned models . . . . .	89
4.12	Deformation mechanisms inside the grains at different strains . . . . .	89
4.13	Variation of maximum stress with twin width . . . . .	93
4.14	RSS variation with strain for different grains of the 5-twin model . . .	95
4.15	RSS variation and observed deformation inside grain 3 . . . . .	96
4.16	RSS variation and observed deformation inside grain 1 . . . . .	97
5.1	Toughness variation with inverse root of twin width . . . . .	100
5.2	Relative amount of dislocations inside grain 3 at 300K . . . . .	103
5.3	RSS variation with strain and CRSS variation with twin width . . . .	104
5.4	Schematic diagram showing three types of refinements . . . . .	105
5.5	Strength and toughness comparison . . . . .	106
5.6	Effect of temperature on the deformation process . . . . .	110
C.1	Coincident site lattice . . . . .	125

# List of Symbols

$d$	Grain size
$d_c$	Critical grain size
$t$ or $l$	Twin lamella spacing or twin width
$\epsilon$	Strain
$\sigma$	Stress
$\sigma_y$	Yield stress
$\sigma_0$ or $\tau_0$	Lattice friction stress
$\sigma_{am}$	Strength of an amorphous material
$\sigma_{gb}$	Strength of the GB
$T$	Toughness
$k$	Material dependent constant/ Hall-Petch coefficient
$w$	Grain boundary width
$g$	Geometric factor
$P_{dis}$	Probability of a dislocation being absorbed by the GB
$\Delta$	Effective grain boundary thickness
$K$	Material parameter
$S_{TB}$	Total area of the TBs in a unit volume
$m$	Strain rate sensitivity index
$f$	Frequency of the TB
$\gamma_{USF}$	Unstable stacking fault energy density

$\gamma_{SF}$	Stacking fault energy density
$\gamma_{UTF}$	Unstable twin fault energy density
$\gamma_{UTM}$	Unstable twin boundary migration energy density
$\gamma_{TB}$	Twin boundary energy
$\gamma_{GB}$	Average grain boundary energy
$A_{TB}$	Twin boundary area
$A_{GB}$	Grain boundary area
$b$	Burgers vector
$N$	Total number of atoms
$i$	Atom number
$j$	All neighboring atoms of $i$
$I, J$	Cartesian coordinate
$V$	Potential energy
$E_{tot}$	Total energy of the system
$E_{coh}$	Cohesive energy
$E_{kin}$	Kinetic energy
$E_i$	Energy of an individual atom $i$
$E_0$	Constant
$r_{ij}$	Interatomic distance between atoms $i$ and $j$
$r_{cut}$	Cut off radius
$\phi_{ij}$	Pair potential due to the interaction between atom $i$ and $j$
$\rho_j$	Uniform electron density field that each atom experiences

$\bar{\rho}_i$	Host electron density at atomic position $i$ due to neighboring atoms
$F_i$	Embedding energy of atom $i$
$E_{embd}$	Total embedding energy
$\mathbf{x}_i$	Position vector of atom $i$
$m$ or $m_i$	Mass of atom $i$
$\mathbf{v}_i$	Velocity of atom $i$
$\mathbf{a}_i$	Acceleration of atom $i$
$\mathbf{p}_i$	Momentum of atom $i$
$\mathbf{f}_i$ or $\mathbf{F}_i$	Force on atom $i$
$H$	Hamiltonian
$s$	Coordinate variable associated with the heat bath
$p_s$	Conjugate momenta of $s$
$M_s$	Thermal mass parameter
$\xi$	Friction coefficient
$k_B$	Boltzmann's constant
$T$	Temperature
$T_{inst}$	Instantaneous temperature
$\mathbf{s}^i$	Slip vector of atom $i$
$n_s$	Number of slipped neighbors
$\sigma_i^{IJ}$	Stress tensor of atom $i$
$\sigma^{IJ}$	Global stress tensor
$\sigma_G^{IJ}$	Grain stress tensor

$\Omega_i$	Atomic volume at site $i$
$\Omega$	Volume of the system
$\Omega_G$	Volume of the grain
$N_G$	Total number of atoms in a particular grain
$\alpha$	Slip system
$\mathbf{s}_\alpha$	Slip direction
$\mathbf{n}_\alpha$	Slip plane normal
$\tau_{RSS}^\alpha$	Resolved shear stress on $\alpha$
$\rho_{dis}$	Dislocation density
$\rho_t$	Twin density
$\rho_{int}$	Interfacial/TB dislocation density
$\mathbf{h}$	Search direction
$\mathbf{g}$	Residual
$\mathbf{A}$	Hessian matrix
$Z_v$	Partition function

## List of Abbreviations

TB	Twin boundary
CTB	Coherent twin boundary
GB	Grain boundary
MD	Molecular dynamics
RSS	Resolved shear stress
CRSS	Critical resolved shear stress
TBAZ	Twin boundary affected zone
CSL	Coincident site lattice
CG	Conjugate gradient
LAMMPS	Large-scale atomic/molecular massively parallel simulator
H-P	Hall-Petch
DFT	Density functional theory
EAM	Embedded atom method
CSP	Centrosymmetry parameter
SV	Slip vector
COM	Center of mass
nc	Nanocrystalline
nt	Nanotwin
UFC	Ultra fine crystalline

RT	Room temperature
ECAP	Equal channel angular pressing
TEM	Transmission electron microscopy
GSF	Generalized stacking fault
GTF	Generalized twin fault
TBM	Twin boundary migration
CN	Coordination number

# Chapter 1

## Introduction

### 1.1 Materials at the nanoscale

Nanostructured materials can be metals, ceramics, polymers, or composites composed of very small crystalline grains or particles in the range of 1-100 nanometers (nm). The study of nanomaterials is the fastest growing area in materials science and engineering. Much of the fascination with nanomaterials stems from the unique mechanical, electrical, chemical, optical, and magnetic properties that matter exhibits at the nanoscale. For instance, opaque, inert, stable, and insulator materials become transparent, catalytic, combustible, and conductor, respectively, at the nanoscale. These properties or effects can not be attained by reducing the grain size from macro to micro dimensions, however, it becomes pronounced when the nanometer size range is reached, enabling wide-ranging industrial, biomedical, and electronic applications. For instance, nanomaterials are being used in nanocomposites, magnetic materials, drug delivery, nanocoating, tribological application, tissue engineering, and biological MEMS. An important aspect of nanoscale materials is the 'size effect'. The vastly increased ratio of surface area to volume profoundly affects the evolution of struc-

tural, thermodynamic, electronic, spectroscopic, and chemical features of these finite systems. It is believed that the theoretical strength of materials can be reached or quantum effects may appear with enough reductions in particle size [1]. From a mechanical engineering point of view, nanomaterials exhibit superior tensile strength, hardness, wear resistance, and corrosion resistance compared to those of the coarse-grained materials [2]. These measured mechanical responses depend upon microstructural features such as the grain size, point defects, dislocations, grain boundaries etc., as well as the underlying deformation mechanisms occurring inside the grains.

Experimental investigations [2–5] and atomistic simulations [6–10] carried by the researchers suggest that the mechanisms of plastic deformation in nanocrystalline materials are fundamentally different from those observed in the coarse grained materials, and may lead to novel and unique mechanical properties. According to their prediction such deformation mechanisms include partial dislocation emission from the grain boundaries, nucleation of twins either inside the grain interiors or from the grain boundaries, and twin lamellae formation via splitting and migration of the grain boundaries of nanocrystalline face-centered cubic metals [2]. Moreover, the structure of grain boundaries in nanocrystalline materials is still shrouded in mystery. Based on experimental evidence and computer simulations, two contradictory pictures have been proposed by different workers: the earliest works suggest a highly disordered “frozen-gas-like” grain boundary structure, which is substantially different from the structures found in coarse-grained polycrystalline materials [10], whereas more recent experiments suggest that grain boundary structures in nanocrystalline materials are not different but similar to those found in polycrystalline materials [10].

In coarse-grained metals, the plastic deformation is mainly carried by the nucleation and motion of lattice dislocations [3]. Although dislocations are simple line defects of the materials, the ways those defects nucleate and interact with each other

and with grain boundaries, are very complex in nature [11]. Moreover, this microstructural feature is the key element in determining the macroscopic properties of a material, such as the yield strength, ductility, fracture toughness etc. In coarse-grained materials the motion of dislocations within individual grains is hindered by the grain boundaries, which results in dislocation pile-ups against them. Further reduction in grain-size introduces more obstacles to the dislocation motion, thereby making the metal harder to deform. Thus, the more difficult it is for dislocations to nucleate and to move, the stronger and harder but less ductile is any crystalline material [12]. This strengthening mechanism by reducing the grain size is known as the Hall-Petch effect [13, 14]. The existence of the Hall-Petch effect at the nanoscale has been the subject of intensive research in recent years due to the complex behavior observed in nanostructured materials. Most of the results confirm the validity of the classical Hall-Petch relation down to a critical grain size, ( $d_c$  approximately 20 ~ 30 nm), above which the dislocations nucleate from the grain boundaries and triple points, and grain boundaries represent fewer obstacles for the unimpeded glide of dislocations across the grains [8]. However, below this critical grain size the results are still controversial. It is more or less accepted that below  $d_c$  the conventional dislocation-slip mechanisms ceases to be operational in favor of a grain-boundary based deformation mechanism, and the yield and flow stresses decrease with decreasing grain size, a phenomenon known as the “inverse Hall-Petch” effect.

Strength and ductility are the central mechanical properties of any material but are usually opposing characteristics due to the physical nature of plastic deformation. Although very high hardness or strength has already been observed in many nanomaterials, in most of the cases they are very brittle. But several investigations have shown that some nanomaterials can have both of these two opposing characteristics. An unusual nanocrystalline structure has been developed by Wang *et al.* [15]

that combines these two useful properties that are often mutually exclusive. Such a “bimodal” structure consists of micrometer-sized grains embedded in a matrix of nanocrystalline grains, and shows extraordinarily high ductility, but also retains its high strength. In such structures, the nanocrystalline grains provide strength and the embedded larger grains stabilize the tensile deformation of the material [12, 15]. A few authors have proposed a so-called rotational plasticity [12, 16] that has also led to high strength and ductility in nanostructured materials. Such occurrence becomes possible through the formation of a nanometer sized grain structure with predominantly high angle grain boundaries, where the tiny equiaxed grains enhance strength by impeding dislocation motion, and improve ductility through other deformation mechanisms such as grain boundary sliding and enhanced grain rotation.

Another nanocrystalline structure that is drawing much attention to the researchers in recent years is the “nanotwinned” structure, containing a high density of nano-scale twins within the grains. This nanostructure is unique in a sense that it exhibits an unexpected improvement in both strength and ductility with decreasing twin spacing [17–19]. The strength enhancement with twin refinement is comparable to that observed in nanocrystalline Cu samples due to grain refinement. However, the simultaneous enhancement in ductility has been reported to be caused by dislocation interactions with the twin boundaries (TBs). According to the authors the embedded TBs, which are known to be a special kind of coherent boundary, act as dislocation barrier to strengthen the samples, but also accommodate plastic strains due to the interaction with the dislocations [19, 20].

In many other applications, high electrical conductivity and high mechanical strength are often required simultaneously. However, all of the strengthening mechanisms (i.e., grain boundary refinement, cold working or solid solution alloying) lead to a pronounced decrease in conductivity due to the higher scattering of electrons at

the defects of the metals. Lu *et al.* [21] has shown experimentally that both conductivity and strength can be achieved simultaneously by introducing a high density of nanotwins in metals. It has been reported that the TBs are able to block dislocation motion, like conventional grain boundaries, but possess extremely low electrical resistivity compared to that of the conventional grain boundary. Therefore, a metal containing a high density of twin boundaries exhibits ultrahigh strength without losing its high electrical conductivity.

It is apparent that certain properties of materials are not intrinsic. Rather, microstructural features and underlying deformation mechanisms can alter the measured macroscopic properties of a material. Our primary concern of this research is to understand the emergence of material properties on the basis of the features that populate the microstructure. Investigating the underlying mechanisms that contribute to the enhanced mechanical behavior of nanostructured materials is of fundamental as well as practical importance that can be exploited to make the “next-generation” of superstrong metals, ductile ceramics, and wear-free materials.

## 1.2 Atomic scale computer simulation

Atoms and molecules, or extended atomic or molecular structures, are considered to be the basic units, or building blocks, of designing and creating future generation materials. Moreover, advanced materials science is confronted with the need for an increasingly precise control of final product properties to meet specific demands [22, 23]. Since experimental measurements and theoretical modeling based on a continuum approach are not capable of capturing a microscopic view of the physics at such small length scales, atomistic simulations are gaining increasing popularity in materials science to elucidate the effects of defects, surfaces and other microstructural features.

Moreover, predictions and understanding resulting from the atomic-level simulations are proving increasingly accurate and useful. As a consequence, the field of atomistic simulation is becoming an established tool and indispensable partner in materials research and design [23,24].

In recent years, the advent of new computer technologies has led to tremendous improvement of computing speed and data storage capacity. High speed processors and massively parallel computers have enabled the development of new concepts and algorithms for the computational modeling and simulation of materials [25]. The motivations for computer simulations of physical systems are many fold. One of the main motivations is the capability of computer simulations to apply theory to study complex systems and gain insight into their behavior, which are far beyond the reach of present analytical methods and experimental resources. Moreover, computer simulations can bridge the gap between theory and experiment. Some quantities or behaviors are impossible or difficult to measure by experiment. Computer simulations can quantify those quantities quite easily. The laboratory experiment tells us what happens, whereas, theory combined with computation allows us to find out the reason behind it, and to predict the results under similar circumstances. Moreover, computer simulations allow one to validate the analytical models by comparing the results with experiment [26]. Other important features of computer simulation include the stability, accuracy, and efficiency of the solution, which are the most important aspects of solving numerical algorithms. The explanatory, reliable, and predictive capability of computer simulations explain the ever-increasing demand of computation on modern materials science [23].

## 1.3 Motivation

A variety of engineering metals and alloys exhibit twinning as their mode of deformation, and in some cases twinning is purposely introduced into metals and alloys. As stated earlier in this chapter, nanocrystalline grains with embedded nano-scale twins or the nanotwinned structures are observed to enhance both strength and hardness of materials compared to those of the nanocrystalline samples without any twin. Moreover, experimental investigations report two unique characteristics of these nanostructures, exhibiting enhanced ductility with twin refinement and elevated electrical conductivity, both of which are not attainable in twin-free nanocrystalline samples. The primary objective of this research is to explore the underlying atomistic deformation mechanisms governing the observed behaviors of this nanostructured material using the “molecular dynamics (MD)” simulation technique. A state-of-the-art MD simulation package has been used to simulate the behavior of copper (Cu) nanotwinned structure under the application of external loads. Dislocation characterization techniques have been used to thoroughly investigate the underlying deformation mechanisms, and elucidate the relationship between these mechanisms with the observed properties (e.g., the von Mises stress, resolved shear stress, and toughness) of these structures. The deformation characteristics, and hence the mechanical properties are observed to be affected by various parameters, including the twin width, grain size, grain orientation, temperature, and stacking fault energy. Therefore, our goals also include exploring the effects of these parameters on both the deformation behavior and the properties of nanotwinned Cu.

## 1.4 Thesis outline

This thesis consists of six chapters and is organized as follows. Chapter 2 is the literature review part of this thesis and devoted to the properties (such as strength, ductility, strain hardening etc.), and the deformation behavior of materials at the nanoscale. We then focus our attention to the nanotwinned materials, and changes in mechanical properties. Both experimental and atomistic simulation observations of deformation behavior and observed properties have been presented. In Chapter 3 we discuss the basics of the atomistic simulation technique, and various dislocation characterization techniques used in our simulations. Chapter 4 and 5 present the results obtained from the simulations. Chapter 4 discusses the observed deformation behaviors, and the stress-strain response of various nanotwinned Cu. An analysis of resolved shear stress and corresponding changes in the deformation pattern in each grain have also been presented in this Chapter. In Chapter 5 we discuss the toughness of our simulated material. The effects of twin width, grain size, and temperature on deformation behavior, and a technique of grain size/twin width refinement to optimize materials properties have been presented in this Chapter. These two chapters (4 and 5) also appear in modified form as published journal papers [27, 28]. Lastly, Chapter 6 presents concluding remarks based on the results obtained from the simulations, and also gives recommendations for future work.

# Chapter 2

## Literature review

Material behavior is size-scale dependent. The observed behavior of materials at the larger scales can not be directly extrapolated to predict their response at the smaller scales. This chapter presents a thorough review of the research works that have been conducted over last several years focusing on the changes in materials deformation behavior and properties due to grain size refinement from the microscale to the nanoscale, and the unique behaviors exhibited by nanostructured materials. Further enhancement of properties by introducing nanotwins inside the grains is one of the major topics of this review. It will also include a presentation of the deformation behavior of various FCC nanotwinned structures from both the experimental and atomistic simulation perspectives, as well as the analytical models developed so far to explain the observed behavior.

## **2.1 Properties and deformation behavior of materials- from micro to nanoscale**

### **2.1.1 Strengthening by grain size refinement**

Strengthening of materials can be achieved in several ways including work hardening, solid solution hardening, precipitation hardening, and grain boundary strengthening [29]. Among these, the grain boundary strengthening mechanism involves strengthening of materials by changing their average grain size. Plastic deformation mechanisms in coarse-grained metals involve continuous nucleation of dislocations from Frank-Read sources and their glide on various slip systems. Once the grain size becomes smaller than the spacing of the sources (less than  $1\mu\text{m}$ ), this deformation mechanism ceases to operate. Instead, for nanocrystalline (nc) material, mobile dislocations start to nucleate from other sources, such as the grain boundaries (GBs) or triple junctions [30]. In either case, under an applied external stress existing dislocations move through the grain until they encounter a GB. GBs are much more disordered structures than the crystal interior. Hence, GBs impede free dislocation movement and restrict the propagation of dislocations into the neighboring grain. Moreover, the crystal structure in the neighboring grain typically differs in orientation, which requires the dislocation to change direction and move into an appropriate slip plane. This restriction of dislocation movement delays the onset of full-scale plasticity and hence increases the yield strength of the material.

As deformation progresses, more dislocations arrive to the boundary, and create a dislocation ‘pile up’ or a cluster of dislocations unable to move past the boundary. Each dislocation has its own stress field that repels the stress field created by other dislocations in a pile up. This repulsive stress field is the driving force for the dislo-

cations to cross the boundary. Hence, the more dislocations present in a pileup, the greater the stress felt by a dislocation closer to the GB. This increases the possibility of a dislocation passing across the GB into the neighboring grain. Therefore, the yielding of a material is determined by two competing factors- i) the number of the GBs and ii) the number of dislocations in a pile-up. The former restricts the yielding, whereas, the latter facilitates the yielding.

As the grain size decreases, the number of dislocations in the pile up also decreases, however, the number of GBs increases. This results in an increased amount of applied stress necessary to move a dislocation across the GBs. The higher the applied stress to move the dislocation, the higher the yield strength. Thus, there exists an inverse relationship between grain size and yield strength, which is known as the Hall-Petch behavior [13, 14] of materials and expressed as follows in Equation 2.1

$$\sigma_y = \sigma_0 + kd^{-1/2}, \quad (2.1)$$

where  $\sigma_y$  is the yield stress,  $\sigma_0$  is a materials constant for the starting stress for dislocation movement (or the resistance of the lattice to dislocation motion),  $d$  is the grain diameter, and  $k$  is a material-dependent constant. This equation signifies that the smaller the grain size, the higher the number of grain boundaries that oppose dislocation movement and in turn strengthen the material. Figure 2.1(a) shows the Hall-Petch plot of Cu taken from different sources. In this figure, the yield stress is plotted against the inverse root of grain size. Therefore, the grain size becomes smaller as we move to the right along the axis. The positive Hall-Petch trend or strengthening is visible down to the grain size of 25nm ( $0.2\text{nm}^{-1/2}$ ) where a peak in the curve is attained. As the grain size is reduced further, the slope of the curve either levels off or becomes negative, which indicates a break-down of the Hall-Petch behavior at a much smaller grain sizes. A discussion focusing on a material's behavior in that size

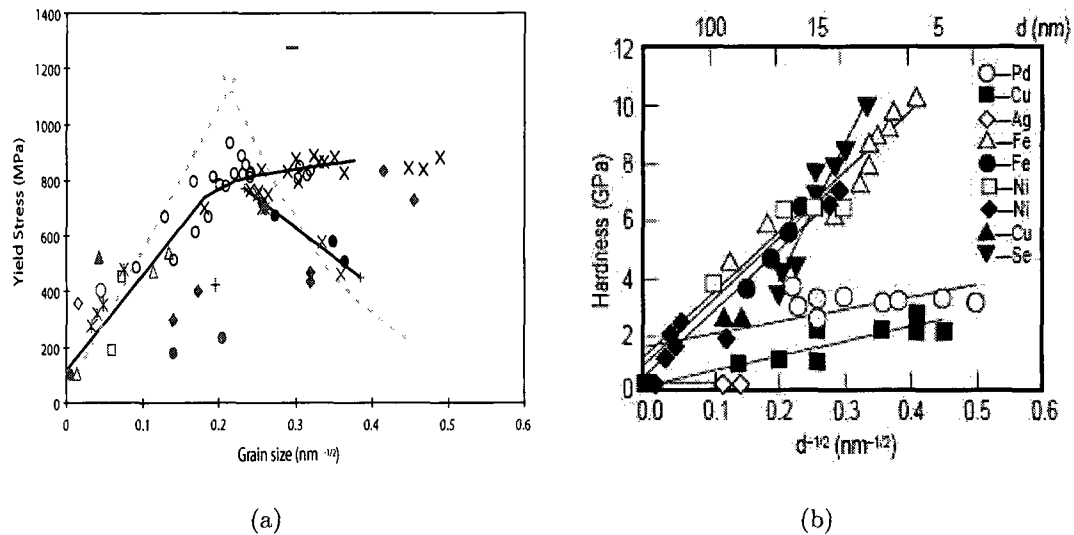


**Figure 2.1** (a) Variation of yield strength with inverse root of grain diameter showing both the Hall-Petch and inverse Hall-Petch relationship for Copper samples [32]. Different symbols denote data taken from various sources for Cu samples ranging from coarse to nano size grains. (b) The Hall-Petch plots for different nc materials showing increase in hardness with decreasing grain size [31].

range (below 25nm) will be presented in the next section. Hardness measurement of various materials also shows an increase in hardness with decreasing grain size, as shown in Figure 2.1(b). In most cases, pure nc metals (10nm grain size) can be 2 – 7 times harder than their coarse-grained ( $> 1\mu\text{m}$ ) counterparts [31], and exhibit the Hall-Petch trend.

Besides the dislocation pile-up model, Meyers and Ashworth [33] propose a three stage deformation mechanism of yielding of polycrystalline metal to describe the Hall-Petch behavior. Their model assumes that the grain-size dependence of yield stress is associated with the generation of dislocations from the GBs. In the first stage, the difference in elastic response between adjacent grains establishes localized stress concentrations at the grain boundaries. These stress concentrations at the GBs result in localized plastic flow at the GBs prior to grain interiors (or micro-yielding),

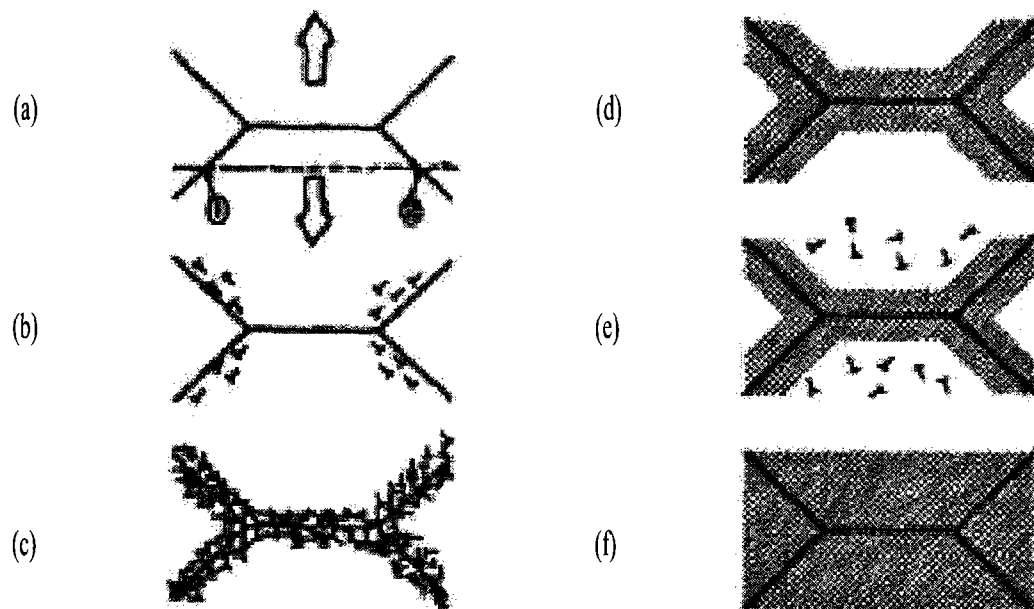


**Figure 2.2** Stages of polycrystalline deformation mechanism: (a,b) localized plastic flow in the GB region, (c,d) formation of a work-hardened GB area with defect free softer interior, and (e,f) plastic deformation of the grain-interior or macro-yielding [1].

as shown in Figure 2.2(a,b). In the second stage, the localized deformation results in a work-hardened GB layer, which prevents plastic flow into the softer core, as shown in Figure 2.2(c,d). In the third stage, as the applied stress rises, the grain interiors undergo plastic deformation and macro-yielding occurs, as shown in Figure 2.2(e,f). Therefore, a polycrystal with smaller grain size has a greater proportion of the work-hardened GB network that consequently increases the macro-yield stress [1, 33].

### 2.1.2 Inverse Hall-Petch relation

Theoretically, it seems possible to create an infinitely strong material by continuing to reduce the grain size. However, in reality, there must, at least, be a limit once grain sizes are lowered down to the size of a single unit cell; at that size materials be-

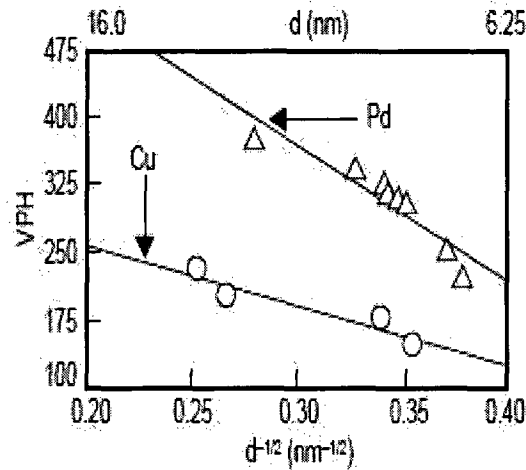


**Figure 2.3** Inverse Hall-Petch plots for nc palladium and copper [31].

come amorphous, not crystalline. In fact, there is a limiting effect which comes into play before this limit called the inverse Hall-Petch effect. The Hall-Petch relation (strengthening by grain size refinement) is widely observed for grain sizes down to the nanometer regime (100nm) when the yield strength reaches to a maximum point. However, experimental research and atomistic simulations on many nanocrystalline materials demonstrate that for grain sizes below 10~20nm, the yield strength either remains constant or decreases with decreasing grain size. This phenomena has been termed the reverse or inverse Hall-Petch relation. It is evident from Figure 2.1(a) that the Hall-Petch relation exists down to the grain size of  $\sim 25\text{nm}$  ( $d^{-1/2} = 0.2\text{nm}^{-1/2}$ ), below which the trend of the line becomes inverse. Some results predict a plateau while the others show a decrease in strength by reducing the grain diameter [32]. Hardness measurement also shows an inverse Hall-Petch relationship for nanocrystalline Cu and Pd, as shown in Figure 2.3. The mechanisms that explain this unique behavior of materials at very small length scale are still controversial, however, several have been proposed to explain it. We review some of these here.

Departure from the Hall-Petch relationship at the smaller length scale can be ex-

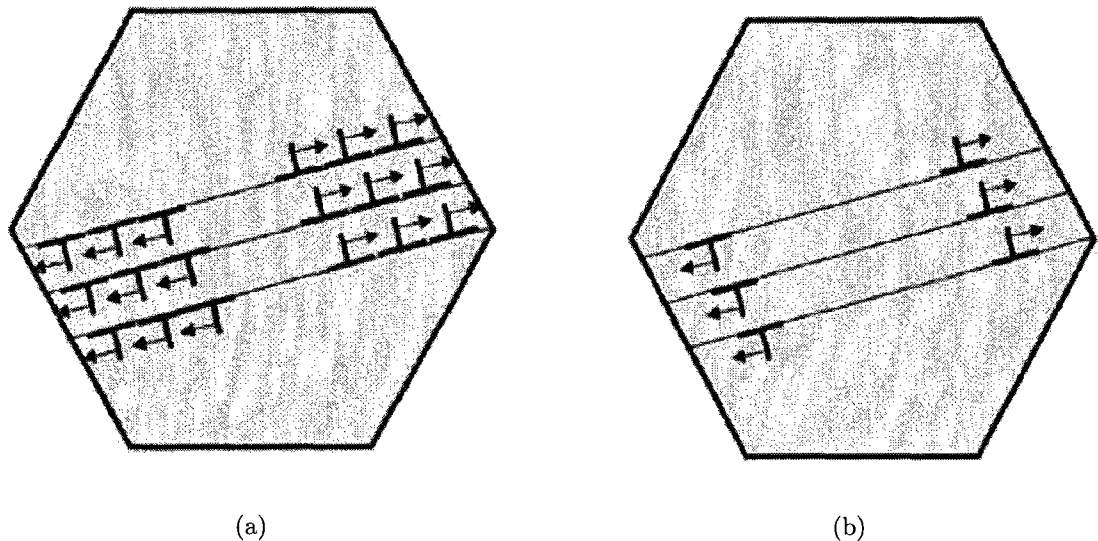


**Figure 2.4** (a) Multiple dislocation pile-up in a microcrystalline grain, and (b) single dislocation pile-up in a nanometer grain [32].

plained by dislocation theory: the pile-up of dislocations at the grain boundaries is the underlying mechanism of the Hall-Petch relationship, as shown in Figure 2.4(a). Once grain sizes drop below the equilibrium distance between dislocations, only one or two dislocations may accumulate against the GB, and the pile-up of many dislocations can not be supported, as shown in Figure 2.4(b). Thus, the Hall-Petch relationship should no longer be valid below a critical grain size, and the conventional dislocation-slip mechanisms ceases to be operational. Moreover, at very small grain sizes the fraction of atoms in the GBs becomes significant (16 percent at 12 nm, 50 percent at 3.5 nm, as estimated in computer simulations [10]), and grain boundary based deformation mechanisms become dominant. Molecular dynamics computer simulations of nanocrystalline Ni and Cu by Van Swygenhoven *et al.* [10] show that at the smallest grain sizes all deformation is accommodated in the grain boundaries, and the material resolves the applied stress by grain boundary sliding, resulting in a decrease in yield strength. Wolf *et al.* [8] suggest that, in the absence of both grain growth and any

dislocations, nanocrystalline FCC metals deform via a mechanism involving an intricate interplay between grain-boundary sliding and grain-boundary diffusion creep [8]. According to them, sliding-accommodated grain boundary diffusion creep may be the dominant deformation mechanism resulting in the inverse Hall-Petch behavior in nanocrystalline materials, even at room temperature [8]. Other deformation mechanisms contributing to the plasticity at nanoscale include partial dislocation emission from GBs, and deformation twinning at relatively higher strain rates and stresses, reported by Yamakov *et al.* for 2-D columnar Al [1,30]. Schiotz *et al.* [7] have also reported the emission of partial dislocations from GBs, transmission across the nc grain, and absorption into the opposing GBs. The time of travel across the grain is so short that the probability of dislocation-dislocation interaction within the grain is exceedingly low. Van Swygenhoven *et al.* [34,35] in their work show that the formation of both unit and partial dislocations is possible within an nc grain, and the ratio of the stacking fault and unstable stacking energies of material determines the possibility of one over the other. Detail discussion will be presented later in Section 2.4.1 .

To describe the inverse Hall-Petch behavior, researchers have proposed various models. Fan *et al.* [36] propose a composite model in which the authors assume a nanocrystalline material consisting of a grain interior and an amorphous grain-boundary layer. The grain interior deforms elastically under external stress, while the grain boundary deforms viscoelastically during the plastic deformation. This model shows that, when the grain size  $d$  is below a certain threshold, the strength of a nanocrystalline material decreases linearly with decreasing grain size, as

$$\sigma = \sigma_{am} \left[ 1 + g \left( \frac{d}{w} - 1 \right) \right],$$

where  $\sigma_{am}$  is the strength of an amorphous material,  $w$  is the grain boundary width,

and  $g$  is a geometric factor [36]. The authors assume no dislocation activity inside the grain interior below the critical grain size, however, computer simulations confirm dislocation activities even at that length scale.

Carlton *et al.* [37] suggest a model for the inverse Hall-Petch effect in nanocrystalline materials based on the probability of dislocation absorption by the GBs or probability of an individual atom on the dislocation core making a jump to the GB. They show that below a critical grain size, typically at the nanoscale, dislocations are more easily absorbed by GBs, and the yield stress of a material becomes a function of grain size,  $d$ , as

$$\sigma_y = \sigma_0 + k \left[ \frac{1 - P_{dis}}{d} \right]^{\frac{1}{2}},$$

where  $\sigma_0$  is the lattice friction stress,  $P_{dis}$  is the probability of a dislocation being absorbed by the GB, and  $k$  is the Hall-Petch coefficient [37]. Finally, another set of models explain the inverse Hall-Petch behavior by considering a nanocrystalline material as a coherent-precipitate strengthened two-phase alloy in which all the grain boundaries merge into a whole continuous matrix and each of the grains embeds in the matrix as a precipitate. This leads to a stress dependence on size as

$$\sigma = \sigma_{gb} + K \left( \frac{d - \Delta}{d} \right)^3,$$

where  $\sigma_{gb}$  is the strength of the GB,  $d$  and  $\Delta$  are the average grain diameter and the effective grain boundary thickness, respectively, and  $K$  is a material parameter [38]. Other explanations that have been proposed to rationalize the apparent softening of metals with nanosized grains include poor sample quality, the presence of voids, and unrecognized pores in samples.

### 2.1.3 Ductility

At room temperature, nc materials exhibit poor ductility compared to coarse-grained materials [19]. A literature survey indicates that a vast majority of nanocrystalline metals exhibit low tensile elongation to failure (percent elongation below  $\sim 10\%$ ) [1]. Figure 2.5 illustrates the elongation to failure data measured for various nc metals ( $d < 100\text{nm}$ ). It is evident from this figure that the elongation to failure of various nc metals is usually much lower than their conventional coarse-grained counterparts. Some nc metals even exhibit “brittle” behavior and fail with little or no visible plastic strains. Some even fail at low stresses. Experimentally, such an early and premature fracture is attributed to processing flaws, especially when the bulk sample is consolidated from loose nanoparticles [1]. This leaves pores inside the samples that trigger failure sometimes before the yielding has a chance to start. Most nc grains also experience plastic instability or a concentration of large deformation in one region that results in a crack formation and an early failure or necking in tension [39, 40]. Moreover, due to their size, nc grains fail to efficiently store the dislocations, leading to the low ductility of nc materials [39–41].

### 2.1.4 Effects of temperature

The effects of temperature on the properties of nanocrystalline (nc) materials have been actively investigated to explore their potential use in cryogenic applications [39–41]. As discussed in Section 2.1.1, at room temperature, nc materials are known to exhibit elevated strength, much higher than their coarse-grained counterparts [13, 19, 31, 32]. With lowering temperature, both strength and elongation to failure of nc materials can be enhanced, making them suitable for cryogenic applications, as shown in Figure 2.6 (curves A and B). Wang *et al.* have reported in several articles that at

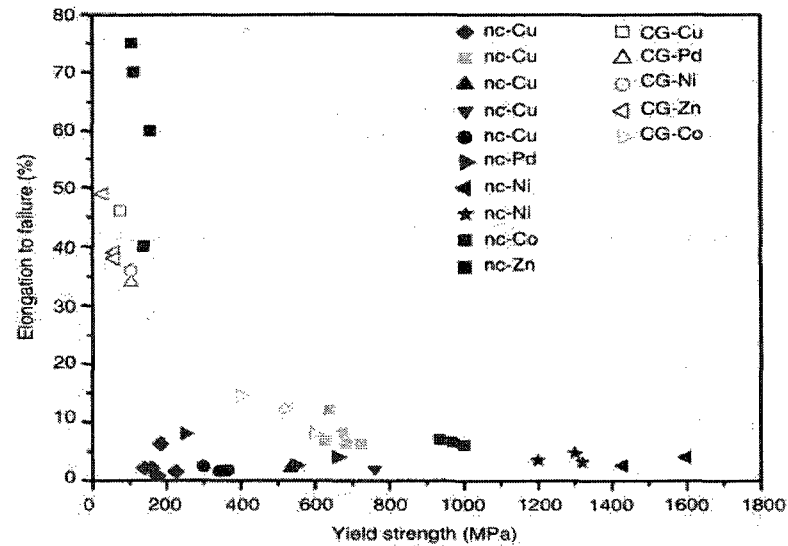


**Figure 2.5** Tensile elongation to failure of various nc metals with grain size  $<100\text{nm}$  in the literature, plotted against their yield strength [1]. Note that almost all the nc metals show a rather low tensile ductility compared with their coarse grained counterparts.

low temperature (e.g., 77K), the dislocation storage capacity of nc grains increases due to reduced dislocation annihilation through thermally activated cross slip or climb, and therefore, enhances the ductility of nc materials [39,40,42]. Moreover, since GBs constitute a large portion of the total volume of nc grains, GB-based deformation mechanisms (e.g., GB sliding, rotation, migration [35,43]) may contribute to the elevated materials properties at low temperature.

### 2.1.5 Strain hardening

Nanocrystalline materials generally show very little or no strain hardening during plastic deformation which is different from the response of coarse grained polycrystalline metals [32]. The lack of effective strain hardening in nc metals upon plastic deformation is due to the low dislocation storage capacity of extremely small grains that fail to increase defect density as coarse-grained metals. Experimentally, the

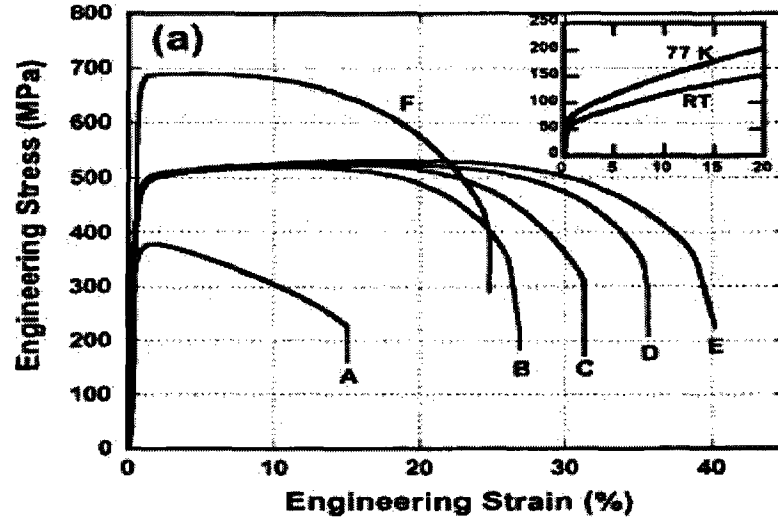


**Figure 2.6** Temperature and strain rate effect on the strength and ductility of nc copper of grain size 300nm. Curve A: RT test at a strain rate of  $1 \times 10^{-4} s^{-1}$ , curves B to E: the same Cu at 77 K and strain rates ranging from  $1 \times 10^{-4} s^{-1}$  to  $1 \times 10^{-1} s^{-1}$ . Both strength and ductility increase with lowering the temperature. The inset shows the yield strength of coarse-grained Cu. Curve F is for the Cu sample with grain size 190nm tested at 77K and strain rate  $1 \times 10^{-1} s^{-1}$  [39].

conventional mechanisms for high strain-hardening, including the formation of dislocation locks such as the Lomer-Cottrell locks, formation of dipoles, and significant pinning due to dislocation-dislocation intersections, have not been observed for nc metals [1]. The low density of dislocations may also arise due to the annihilation of dislocations into the GBs. The large volume fraction of GBs in nc metals act as the sources of dislocations. However, after traversing the grain they get absorbed into the GBs into the opposite side easily. Therefore, GBs also acts as the sinks of dislocations in nc grains. In the absence of effective work-hardening mechanisms, local thermal or geometrical fluctuations trigger the localization of plastic deformation or concentration of large deformation in one region of most nc metals [1, 39, 40]. Figure 2.7 depicts the true stress-strain response of nc copper under tension and compression. The true stress-strain curve under compression reveals strain hardening only at the

first few percent (1 – 2%) of plastic strain, beyond which the curve becomes flat over a large strain range. On the other hand, the response in tension shows a rapid peak and subsequent softening as the localization of plastic deformation leads to necking at the yield stress.

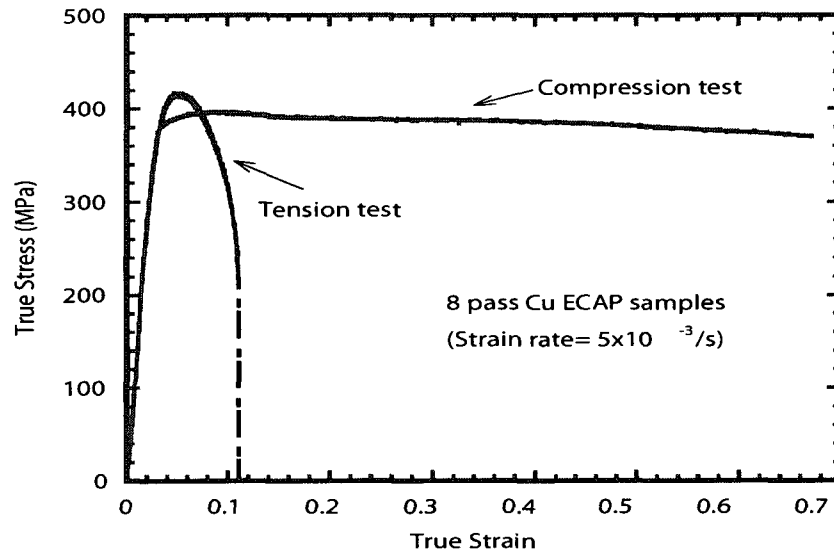


**Figure 2.7** True stress-strain curve of nc copper showing a wide flat plastic region with no strain hardening under compression, except an initial strain hardening over a small plastic strain regime. The response under tension shows a rapid peak and subsequent drop, as the plastic instability sets in early and leads to necking at the yield stress [32].

## 2.2 Nanotwinned structures and changes in properties

Twin boundaries (TBs) are highly symmetrical low energy interfaces across which crystal structures are mirror images to each other. These boundaries are believed to contribute in the same way as GBs to the plastic deformation and strengthening of nanocrystalline materials. Recent experimental observations show that the nano-scale

twins within ultrafine crystalline metals lead to a significant increase in flow stress and hardness [17, 21, 44]. Figure 2.8(a) shows a plot of yield stress as a function of inverse root of the grain size ( $d$ ), where various symbols (other than the star symbols) represent experimental data obtained from different sources for nano-, ultrafine-, and micro-crystalline pure Cu. The figure shows a linear enhancement of yield stress with grain size refinement, over the nm to the  $\mu\text{m}$  range, for polycrystalline Cu. The star symbols in this figure represent the yield stress of ultrafine grained Cu with growth twins, where twin width ( $l$ ) is plotted in place of grain size. It is also evident from this figure that the twin width exhibits the same relation to the yield stress as the grain size in nanotwinned Cu [44]. Moreover, the star symbols generally have higher yield stress values that make the grains with nanotwins more effective than the ordinary grains. Figure 2.8(b) shows that both tensile yield strength and ultimate tensile strength of as-deposited Cu samples with different twin densities increase with total area of TBs in a unit of volume ( $S_{TB}$ ) [21]. Figure 2.8(c) shows the variation of hardness as a function of loading rate in which the average hardness of the sample with a higher twin density is found to be noticeably higher than the sample with a lower twin density [17].

Strengthening metals by means of adding twins has been attributed to the glide dislocation interaction with the TBs. Experimental investigations [17–19, 21] reveal that the presence of twins hinders free dislocation movement and causes dislocation pile-ups at the TBs. When the twin lamellae are thick, a large number of dislocations assemble together in the pile-up and produce a stress concentration at the TBs. Thus, less applied stress is required for slip transmission across the TBs. However, for thin lamellae, only one or two dislocations may gather at the pile-up and hence, extremely high external stress is needed for dislocation transmission across the TBs. In this sense, the TBs behave more like the GBs in strengthening of materials at

the nanoscale. Researchers have also investigated the tensile stress-strain behavior of polycrystalline Cu containing different volume fraction of nano-sized twins and compared the response with twin-free samples at various strain rates [17–19]. Figures 2.9(i-iii) show TEM images of as-deposited Cu samples containing different twin densities (between 15~96nm): (i) the lower twin density, (ii) the medium twin density, and (iii) the higher twin density, respectively. These Cu samples consist of roughly equiaxed grains (about 400~450 nm). The tensile stress-strain curves for these samples, as shown in Figure 2.10(a), tested at different strain rates indicate that for a fixed twin width, the yield strength and tensile strength increase with increasing loading rate. Furthermore, the yield strength, tensile strength are found to increase with decreasing twin spacing. These trends, caused by the introduction of nanotwins, are comparable to those observed in nanocrystalline Cu samples due to the grain refinement. However, the reduction in grain size to the nanometer regime leads to significant reduction in ductility (strain to failure value). However the authors report significant increase in ductility with decreasing twin spacing. Shen *et al.* [19] also report a similar observation that the elongation-to-failure increases considerably with increasing twin lamellae density, as shown in Figure 2.10(b). This enhanced ductility has also been reported to be caused by dislocation interactions with the TBs. It is known that when a dislocation crosses a TB, a dislocation dissociation reaction takes place and a Shockley partial dislocation is left behind at the TB, which may accommodate plastic straining. Therefore, the higher the TB density, the larger the density of accumulated dislocations at the TB, which results in enhanced ductility due to plastic deformation [19].

Moreover, nanocrystalline samples with enhanced strength usually exhibit inferior electrical conductivity. However, an interesting observation has been revealed by Lu *et al.* [21], which shows that the electrical resistivity of nanotwinned Cu sample is

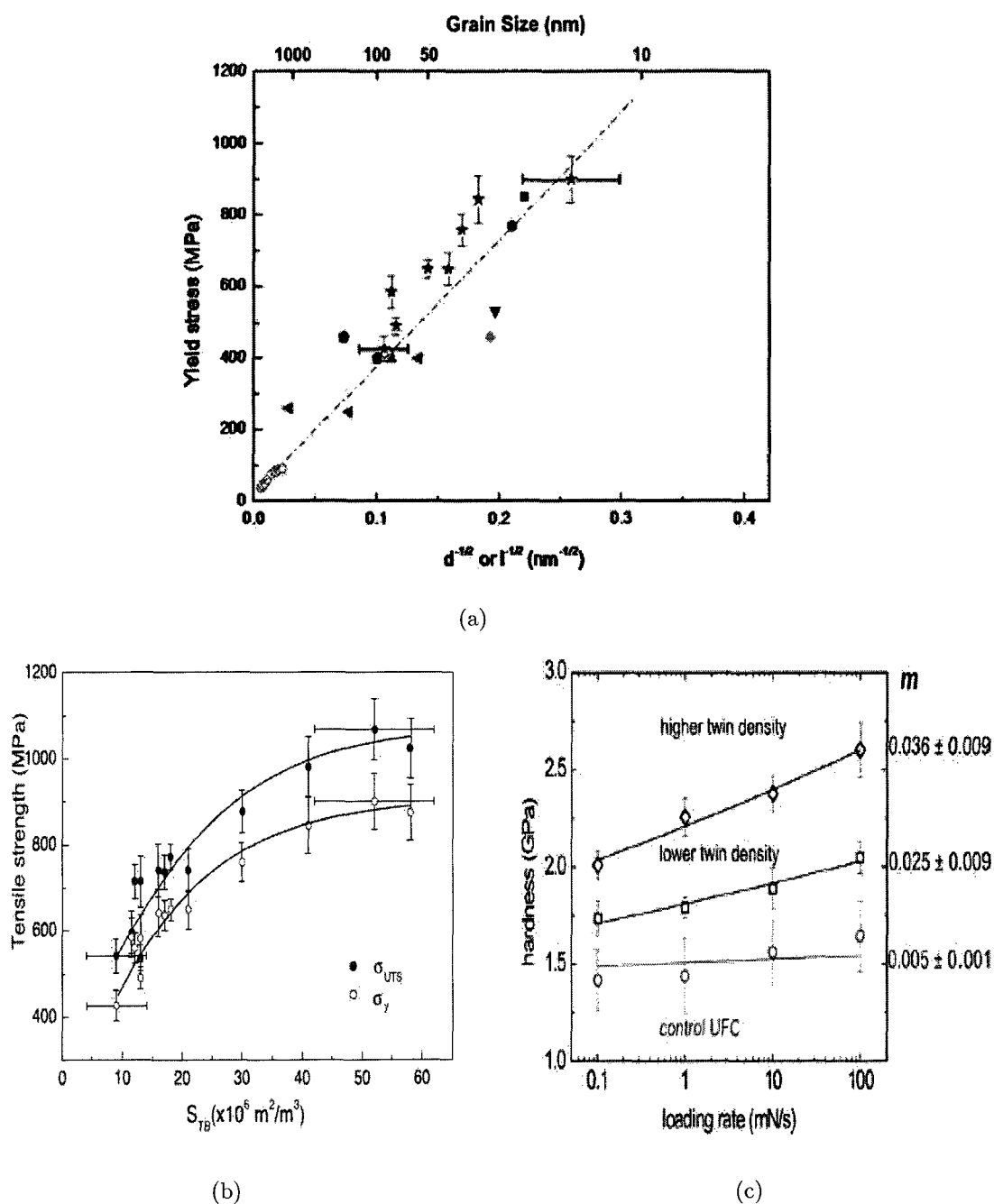


**Figure 2.8** (a) A plot of the yield stress as a function of inverse square root of the grain size  $d$ , where various symbols (other than the stars) denote experimental data obtained from various sources on nano-, ultrafine- and micro-crystalline pure Cu. The star symbols with scatter range denote data for Cu samples with controlled growth twins for which the twin width  $l$  is plotted in place of the grain size  $d$  [44]. (b) Ultimate tensile strength and tensile yield strength variation with the total area of TBs in a unit of volume [21], and (c) variation of hardness as a function of loading rate for samples with different volume fraction of twins [17].

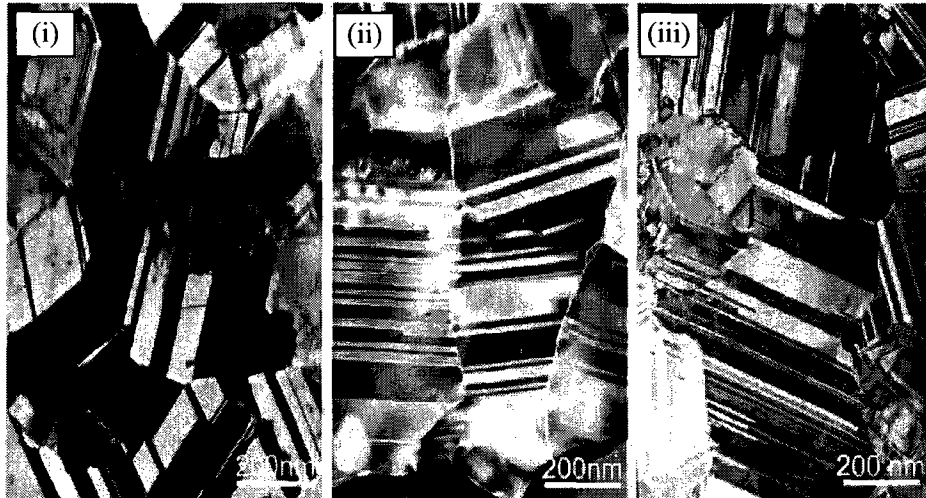


**Figure 2.9** TEM images of as-processed microstructure of Cu with (i) lower twin density, (ii) medium twin density, and (iii) higher twin density [19].

much less than that of the nanocrystalline Cu without twins, and very close to that of the coarse-grained Cu specimen over a wide temperature range, as shown in Figure 2.11. The authors argue that conventional strengthening approaches based on adding various kinds of defects (e.g., grain boundary refining, solid solution alloying, plastic straining etc.) increase the scattering of conducting electrons at the defects, thereby making high electrical conductivity and high mechanical strength two contradictory properties of metals. However, the TBs not only act in the same way as the GBs to strengthen the metals (by hindering dislocation movement) but also to minimize the scattering of conducting electrons. Therefore, metals containing high density of TBs exhibit higher strength without significant loss of electrical conductivity [21].

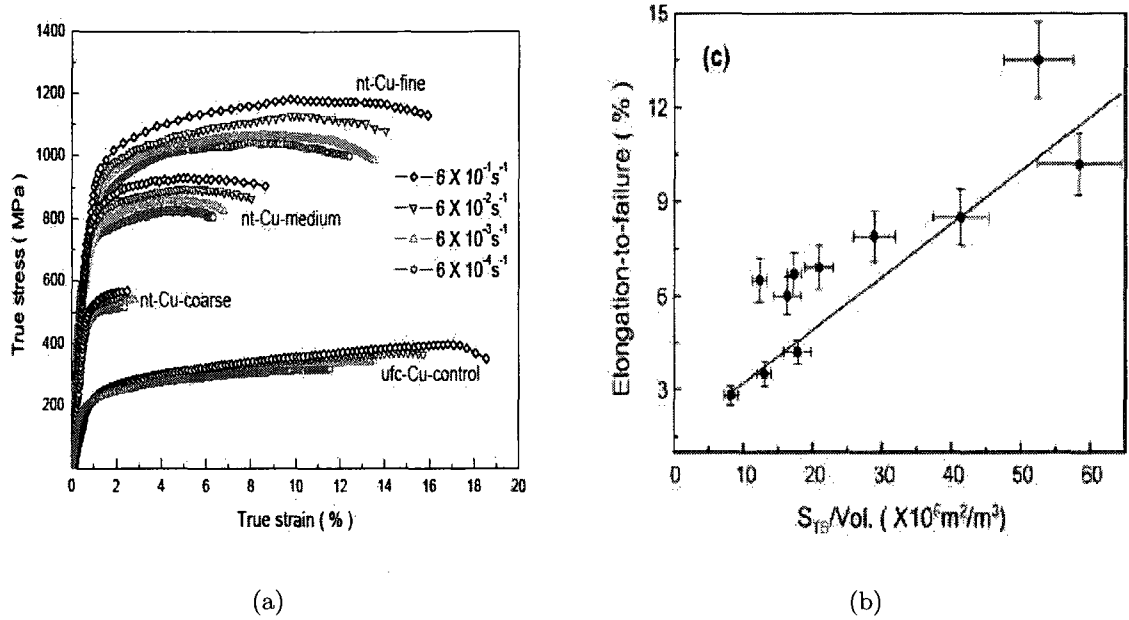
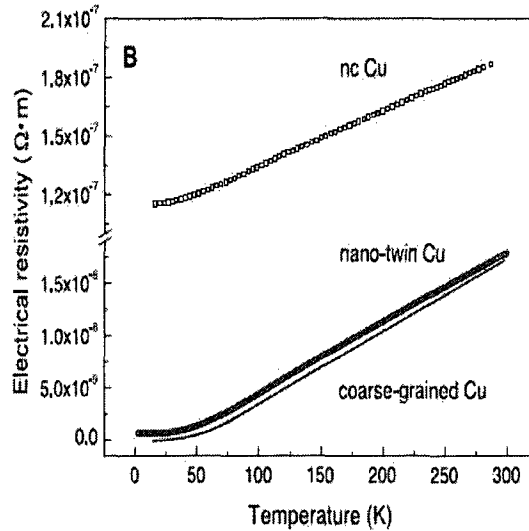


Figure 2.10 (a) Tensile stress-strain curves for Cu samples with various twin densities tested at different strain rates [18], and (b) elongation-to-failure as a function of twin density [19].

## 2.3 Deformation behavior of nanotwinned samples-experimental observations

As mentioned earlier, the post tensile and indentation TEM images suggest that the interaction of dislocations with the TBs plays a crucial role in plastic deformation of nanotwinned metals, and the strengthening of these samples is attributed to dislocation blocking at the TBs, similar to what is observed in conventional GBs. Figure 2.12 shows a high dislocation density in the vicinity of the TBs compared to a relatively defect-free microstructure of an as-deposited sample. These dislocations are identified as Shockley partial dislocations, and most of the plastic strain is carried by the dislocations piling up along the TBs [18]. Abundant dislocation accumulation causes displacement of twin boundaries and alteration of twin width, as shown



**Figure 2.11** Electrical resistivity of various Cu samples as a function of temperature [21]. Nanotwinned Cu exhibit electrical resistivity much less than nc Cu without twins, but very close to the coarse-grained Cu.

in Figure 2.13. It is observed that the crystal lattice within a few nm of the TBs is deformed heavily due to the high density of dislocation along the TBs compared to the internal volume a few nm away from the TBs [18]. Formation of steps, jogs, and possible dislocation emission from the displaced TBs are also evident in Figure 2.14. Lu *et al.* [21] suggest that in addition to the dislocation accumulation along the TBs, dislocations may also propagate across the coherent TBs by cross slip onto an equivalent plane of a twin. The blocked dislocations propagate across the TBs if a dislocation dissociation reaction takes place, leaving behind a non-glissile Frank dislocation at the TBs.

However, Konopka *et al.* in their work show that twin boundaries can act as both strong and weak barriers to the dislocation movement depending upon the frequency of the TBs ( $f$ ) and temperature.  $f$  can be expressed as the ratio of the number of the TBs to the total number of all of the GBs [45]. In their experiment, with Cu samples of the same grain size but different frequency of the TBs, they reveal an

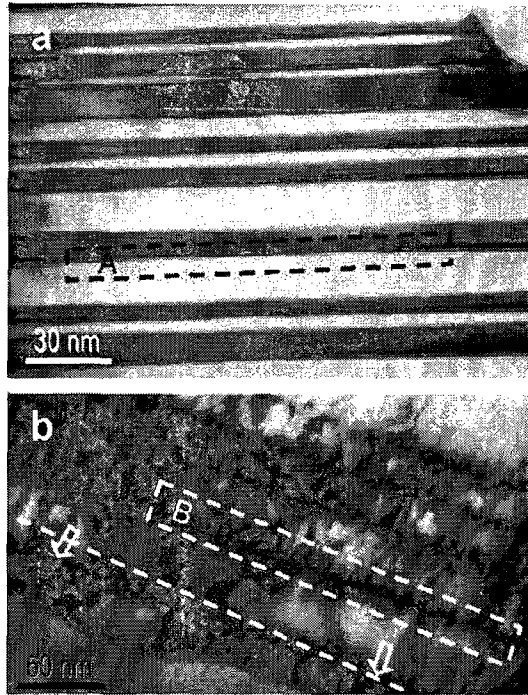


**Figure 2.12** (a) TEM image of an as-deposited Cu sample with straight twin boundaries with no dislocation, and (b) high dislocation accumulation along the TBs after deformation [18].

inverse relationship between the flow stress and the twin frequency as [45]

$$f_{A1} > f_{A2} \quad \sigma_{0.2(A1)} < \sigma_{0.2(A2)}.$$

This reduced flow stress is especially pronounced at temperatures between 200 and 500°C. The authors explain this observed softening by considering the TBs as dislocation sources. An increased frequency of TBs results in a reduction of the flow stresses as the number of dislocations generated by these boundaries is proportional to the TB surface. TEM images, shown in Figure 2.15, also reveal dislocation loop formation from a TB. However, above this temperature range and at a higher deformation such differences in the stress values are not observed, which can be attributed to the recovery process that proceeds under these conditions [45].

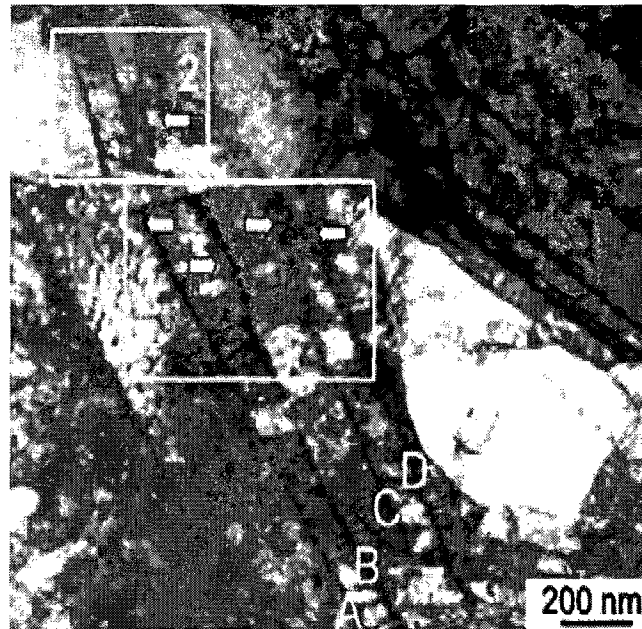


**Figure 2.13** Displaced twin boundaries due to deformation. At position A, B, C, and D the TBs are almost parallel to each other. However, the same TBs appear to be displaced inside the white squares, marked by the arrows [17].

## 2.4 Atomistic simulations

### 2.4.1 Stacking fault and generalized stacking fault curve

In a perfect lattice atoms are stacked into layers in a regular sequence. A stacking fault is a planar defect that is formed when the regular sequence has been interrupted locally [13]. This planar fault is generally observed in the closed packed planes of closed packed structures. Figure 2.16(a) shows the atomic arrangement of  $\{111\}$  planes of FCC crystal. According to this figure the atomic planes are stacked into an  $ABCABCABC\dots$  sequence. The effect of a stacking fault is created either by removing or introducing an extra plane. For example, if an  $A$  layer slides into the  $B$  position and all the layers above it move accordingly, i.e,  $B$  to  $C$ ,  $C$  to  $A$ ,  $A$  to  $B$  etc., then a new sequence will be formed ( $ABCBCABCA\dots$ ), as if an  $A$  plane had

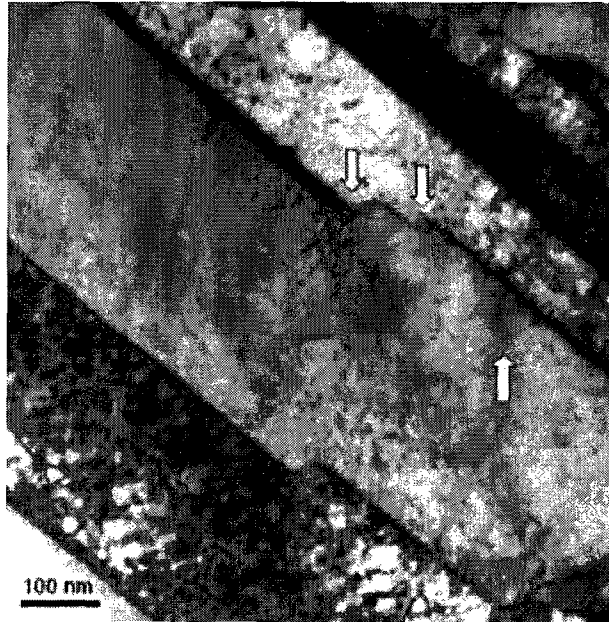


**Figure 2.14** Displacement of TBs resulting in steps and jogs in the boundary (as shown by downward pointing arrows), and emission of dislocation loop from the twin boundary (as shown by upward pointing arrow) [17].

been removed. The sliding of one layer over the other happens due to the emission of partial dislocations, as shown in Figure 2.16(b). This figure demonstrates how an atom at position  $B$  moves to the next  $B$  site via position  $C$ . It is energetically more favorable if one  $B$  atom moves to position  $C$  first, then move to the next  $B$  site, instead of moving to the next  $B$  site directly over  $A$  atom. Moving of an atom from  $B$  site to  $C$  site implies the formation of a leading partial dislocation (Burgers vector  $b_2$ ) which leaves a stacking fault behind its path. This stacking fault sequence will be erased by the formation of a trailing partial dislocation (Burgers vector  $b_3$ ) when the previous  $B$  atom moves from the  $C$  site to the next  $B$  site. These two partial dislocations simultaneously repel and attract each other and establish an equilibrium separation distance with an stacking fault ribbon between them.

The generalized stacking fault (GSF) curve (or the energy-displacement curve)

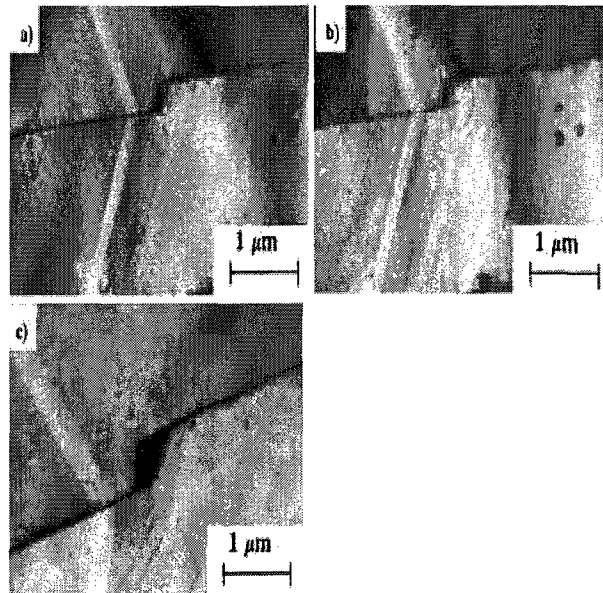


**Figure 2.15** (a) A dislocation loop joined with a part of the twin boundary at the state of initial tension, (b) the dislocation loop shown in (a) has been multiplied due to continued tension, and (c) other dislocation loops joined with the TB generate new dislocations [45].

shows the amount of energy required to displace adjacent atomic planes past one another. As an atomic plane moves past the adjacent plane, the energy per unit area of the slip plane increases to a maximum  $\gamma_{USF}$ , and decreases to some stable value  $\gamma_{SF}$ , as shown in Figure 2.17.  $\gamma_{USF}$  and  $\gamma_{SF}$  are termed the unstable fault energy and stacking fault energy, respectively. The  $\gamma_{USF}$  represent the amount of energy that is required in order to nucleate a partial dislocation, whereas, the  $\gamma_{SF}$  is the energy associated with the stacking fault left behind by the partial dislocation. At this point two possible scenario can occur, either a trailing partial dislocation can emit at the same plane overcoming the energy difference ( $\gamma_{USF} - \gamma_{SF}$ ) or a partial dislocation can emit at the adjacent slip plane forming a deformation twin [34]. Van Swygenhoven *et al.* [34] propose that the absolute value of  $\gamma_{SF}$  is not a sufficient condition to predict the tendency of emitting trailing partial dislocation, rather a

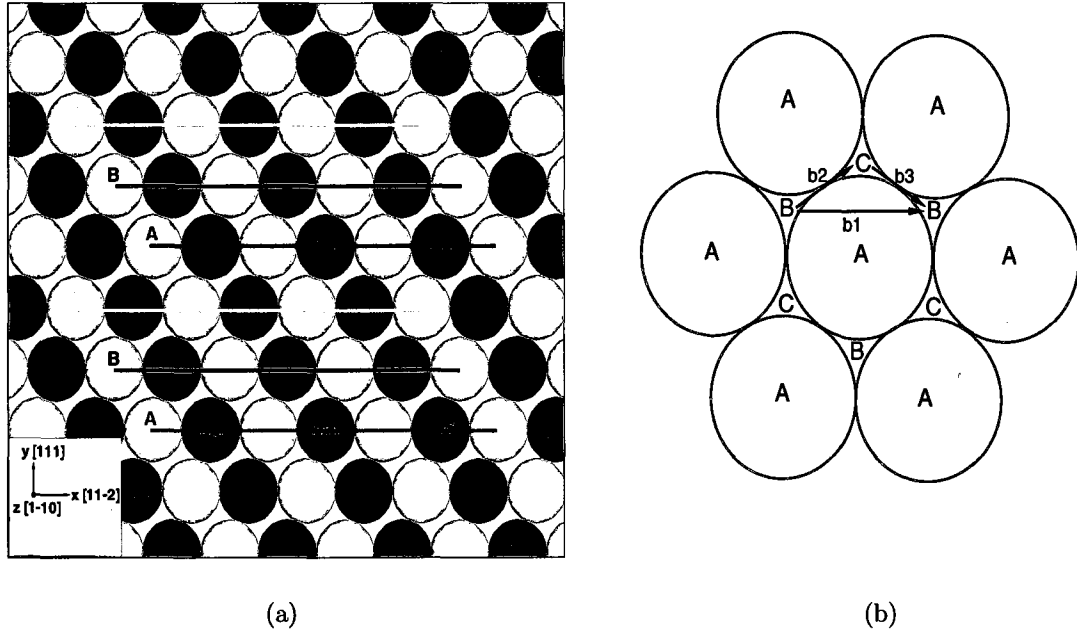


**Figure 2.16** (a) Stacking sequence of  $\{111\}$  planes of FCC crystals, viewing the  $\{111\}$  planes edge-on ( $ABCABC\dots$ ). The color of the balls (blue or green) signifies their position on a different x-y plane along the z-direction, and the same colored balls are located on the same (110) plane along the z-direction. (b) Slip of  $\{111\}$  planes in FCC crystals viewing the  $\{111\}$  planes from the top; reproduced from [13]. It shows a more energetically favored path followed by a B atom to move to the next B cite via position C, instead of moving directly over A.

ratio of  $(\gamma_{SF}/\gamma_{USF})$  gives a better estimation for various FCC metals. As the value of the ratio approaches unity, the energy barrier that has to be overcome to create a trailing partial becomes less, and full dislocation activities become more evident. Otherwise, only the leading partial propagates through the grain forming an extended partial dislocation. Similarly, for the second alternative path, the emission of a partial dislocation in the neighboring plane forming a deformation twin depends upon the ratio of  $\gamma_{UTF}/\gamma_{USF}$  [34], where  $\gamma_{UTF}$  is the unstable twinning fault.

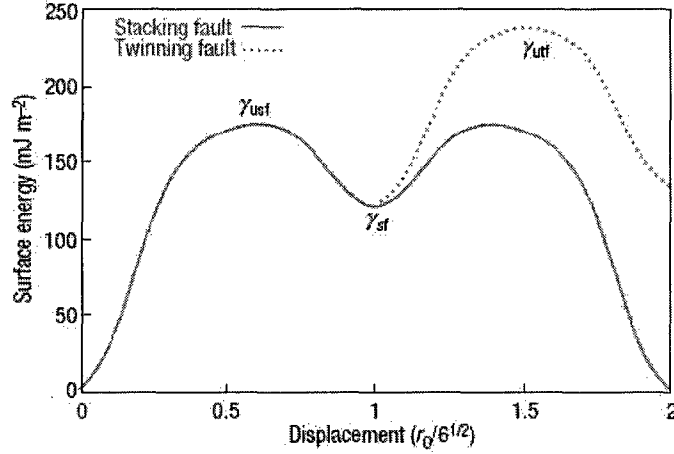


**Figure 2.17** Generalized planar fault curve showing unstable stacking fault  $\gamma_{USF}$ , stacking fault  $\gamma_{SF}$ , and unstable twinning fault  $\gamma_{UTF}$  [34].

## 2.4.2 Deformation behavior

The deformation behavior of various nanotwinned structures has also been investigated by researchers using atomistic simulations [46–49]. Froseth *et al.* [46] report that for nc-Al with pre-existing TBs, twin boundary migration is a predominant deformation mode. The migration process starts at the intersection of a TB with the GB by the emission of partial dislocation at the plane adjacent to the TB. As the partial dislocation propagates through the grain the existing TB migrates to the neighboring (111) plane [46]. The authors explain the TB migration event in terms of another similar generalized planar defect energy curve, known as generalized twin boundary migration (TBM) energy curve (as shown in Figure 2.18(a)). The maximum of this curve represents the unstable TBM energy density,  $\gamma_{UTM}$ . A low value of  $\gamma_{UTM}$  compared to  $\gamma_{UTF}$  and  $\gamma_{USF}$  signifies dominant deformation activities via TBM compared to partial, full, or deformation twinning [46]. This is not usually the case for other FCC metals, e.g., Cu and Ni. For Al, the ratio of  $\gamma_{USF}/\gamma_{UTM}$  is  $\sim 3$ , which leads to dominant deformation of nanotwinned Al via TBM. However, for Cu and

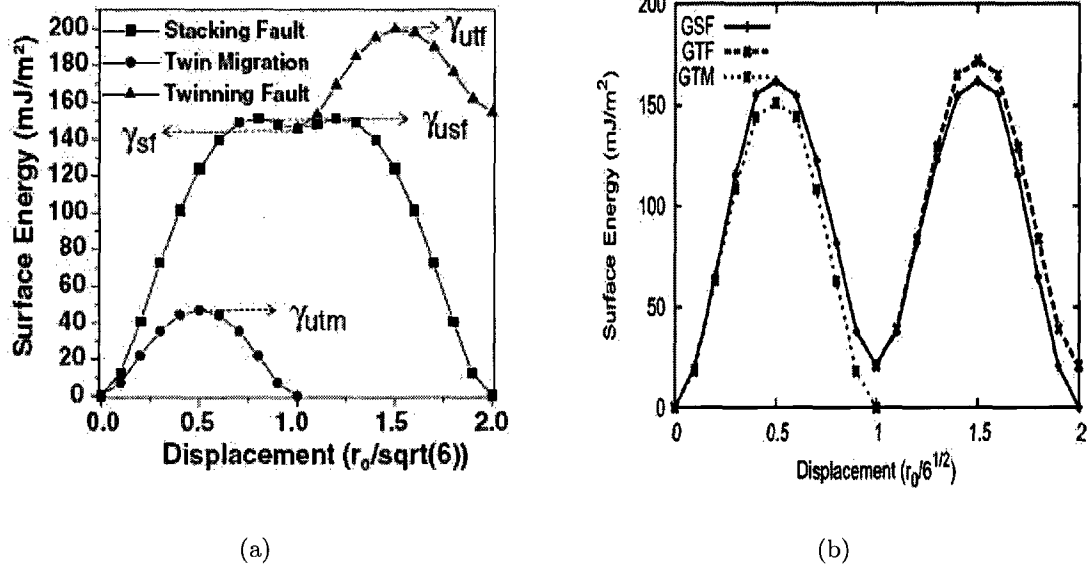


**Figure 2.18** (a) Twin boundary migration energy density  $\gamma_{UTM}$  in comparison with  $\gamma_{USF}$ ,  $\gamma_{SF}$ , and  $\gamma_{UTF}$  [46], and (b) various generalized planar fault energy curves for Cu [47].

Ni the value of this ratio is 1 and 1.3, respectively [47]. Therefore, for both Cu and Ni TBM is about as probable as the formation of extended partial dislocations. It is extremely important to properly understand the shape of GSF curves, as they explain and predict the various deformation mechanisms (e.g., emission of extended partial dislocation, full dislocation activities, formation of deformation twins, or TBM). More precisely, key features of the GSF curves are the ratios of  $\gamma_{SF}/\gamma_{USF}$ ,  $\gamma_{UTF}/\gamma_{USF}$ , and  $\gamma_{UTM}/\gamma_{USF}$ . The energy density curves of the formation of various defects have been generated using the Cu potential used in this work [50], and will be used in Chapter 4 to explain our results.

As a final note, Cao and Wei [48] recently published their investigation on plastic deformation behavior of nanotwinned copper samples under uniaxial tensile load by MD simulation. They also report strengthening by adding twin boundaries within 2D columnar grains and thinner twins exhibit higher strength at different strain rates.

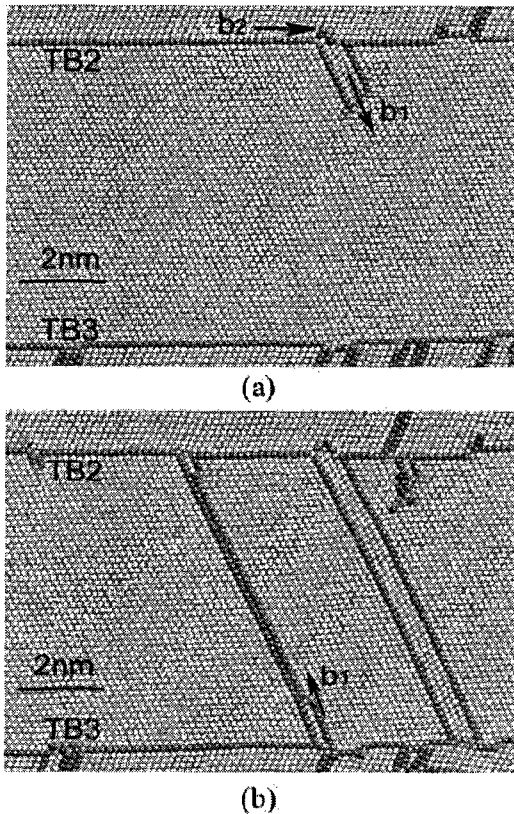


**Figure 2.19** (a) A dislocation nucleated at TB2 dissociate into a Frank partial  $b_2$  and a Shockley partial dislocation  $b_1$ , and (b) the movement of  $b_1$  is blocked at TB3 and at the same time another partial dislocation nucleates from TB3 [48].

They also report dislocation nucleation from the TBs, as shown in Figure 2.19, which is analogous to the experimental observations made by Lu *et al.* [17] and Konopka *et al.* [45].

### 2.4.3 Dislocation-twin boundary interaction

Atomistic simulations have also been conducted by several researchers to properly understand the dislocation-twin boundary interaction mechanisms of various nanotwinned FCC samples. MD simulations by Yamakov *et al.* [49] reveal detailed mechanisms of dislocation-dislocation and dislocation-twin boundary interactions in

nanocrystalline 2D columnar Al crystal. In their study they report deformation twinning as a prominent mode of deformation at an early stage that originates by the emission of partial dislocations from the GBs. They also present two interesting modes of interaction between a glide dislocation and an existing twin boundary. In the first mode, upon encountering the TB the dissociated dislocation undergoes either a twinning (adding a twin plane) or untwining (removing a twin plane) reaction that leaves behind a stair-rod dislocation at the TB, and can be expressed as follows [49]

$$AC \rightarrow A\delta + \delta C \rightarrow A\gamma + \gamma\delta + \delta C$$

$$AC \rightarrow A\delta + \delta C \rightarrow A\gamma + \delta D/C\gamma + \gamma D.$$

The equations are written in usual Thompson notation, as shown in Figure 2.20<sup>1</sup>. In the first equation, the leading dislocation,  $A\delta$ , reacts with the TB and forms a twinning dislocation,  $A\gamma$ , and a stair-rod dislocation,  $\gamma\delta$ . The second reaction happens when  $\delta C$  is the leading dislocation, instead of  $A\delta$ , and the stair-rod dislocation becomes  $\delta D/C\gamma$  [49]. In the second mode, the incident dissociated dislocation may cross-slip in the twin plane without leaving a stair-rod dislocation at the TB, however, the twinning or untwining reaction still takes place [49]. Jin *et al.* show two different ways a screw dislocation may interact with coherent twin boundaries for various FCC metals [52]. Depending upon the energy barrier for the nucleation of a Shockley partial dislocation, a screw dislocation may either propagate into the adjacent twin

---

<sup>1</sup>The faces of Thompson tetrahedron correspond to  $\{111\}$  type slip planes of FCC lattice. Figure 2.20 illustrates a two dimensional representation of the Thompson tetrahedron, obtained by unfolding it at one end. The edges of the tetrahedron (or the lines joining two Roman letters,  $AB, BC, CD$ ) represent full dislocations of  $\langle 110 \rangle$  type, while the lines joining each vertex and the centroid of the same slip plane ( $A\gamma, B\alpha, C\beta$ ) represent Shockley partials of  $\langle 112 \rangle$  type. The lines joining each vertex and the centroid of the opposite slip plane represent Frank partials ( $A\alpha, B\beta, C\gamma$ ), whereas, the lines joining two centroids represent stair-rod dislocations ( $\gamma\delta, \alpha\delta$ ).

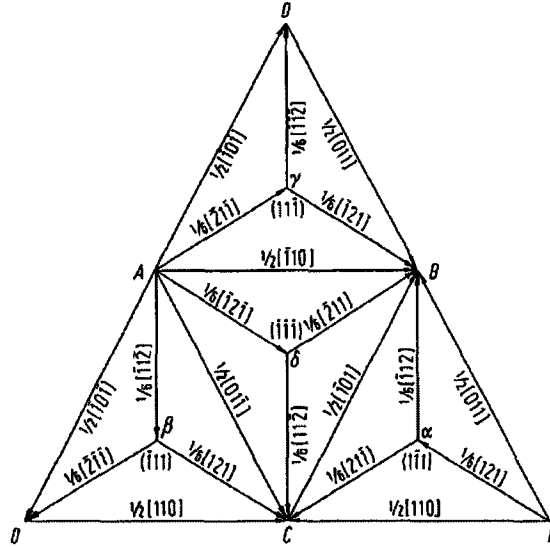


**Figure 2.20** Planar view of the Thompson tetrahedron. Source [51].

grain through the boundary or it may dissociate within the twin boundary plane. For materials with higher stacking fault energy ( $\gamma_{SF}$ ) than the twin fault energy ( $\gamma_{UTF}$ ) (e.g., Al), cross-slip into the twin plane occurs spontaneously, and is determined by the fault energy difference  $\gamma_{UTF} - \gamma_{SF}$ . As shown in the top row of Figure 2.21, a screw dislocation constricts first at the TB and then re-dissociates into two Shockley partials separated by a newly formed twin fault on the twin plane. On the other hand, materials with stacking fault energy ( $\gamma_{SF}$ ) lower than both the unstable stacking fault energy ( $\gamma_{USF}$ ) and unstable twin fault energy ( $\gamma_{UTF}$ ) (e.g., Cu and Ni), the screw dislocation passes through the twin plane from the parent grain into the twin grain, and this event is dictated by the fault energy difference  $\gamma_{USF} - \gamma_{SF}$ . A screw dislocation in this case, as shown in the bottom row of Figure 2.21, re-dissociates into two Shockley partials along the same glide plane in the twin grain separated by an intrinsic stacking fault [52]. The middle row of Figure 2.21 is the schematic of these two possible mechanisms. A recent paper by Zhu *et al.* [20] also demonstrates two similar interaction mechanisms of a screw dislocation with the twin boundary.

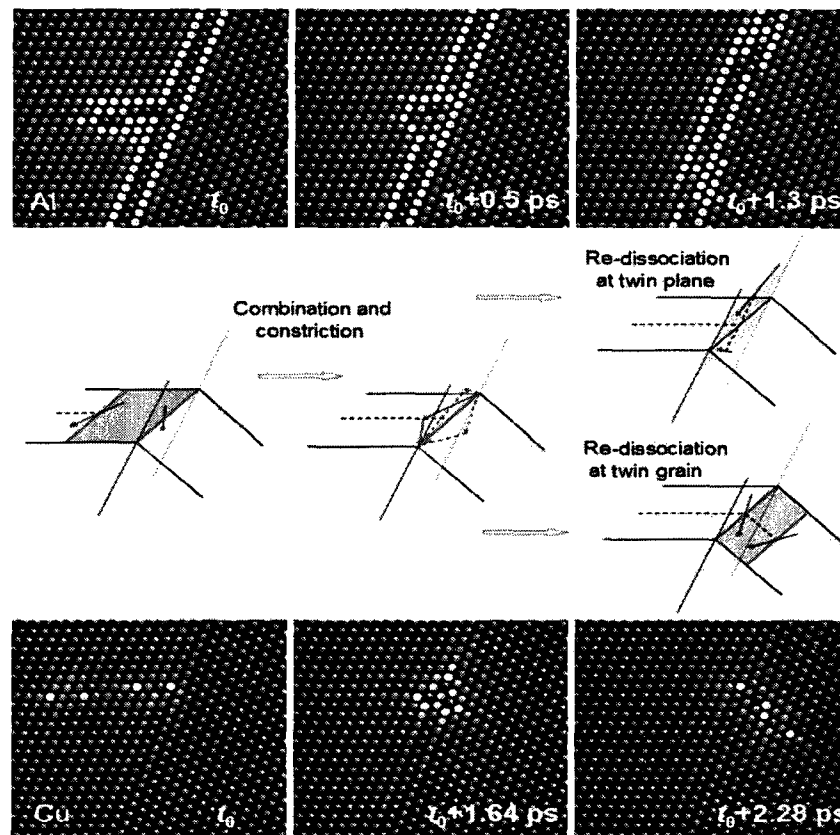


**Figure 2.21** Interaction of a screw dislocation with coherent TB. The top row shows dissociation of a screw dislocation into the twin plane, whereas the bottom row shows the direct transmission through the twin plane from the parent grain into the twin grain. The middle row is the schematic of these two possible mechanisms [52].

As shown in Figure 2.22, two incoming partials either constrict first to a full screw dislocation, followed by absorption into the TB and desorption into the twin grain or the leading partial penetrates into the twin grain without waiting for the trailing partial to arrive. In the latter case, a stair-rod dislocation is temporarily deposited on the TB and is freed when the trailing partial arrives [20].

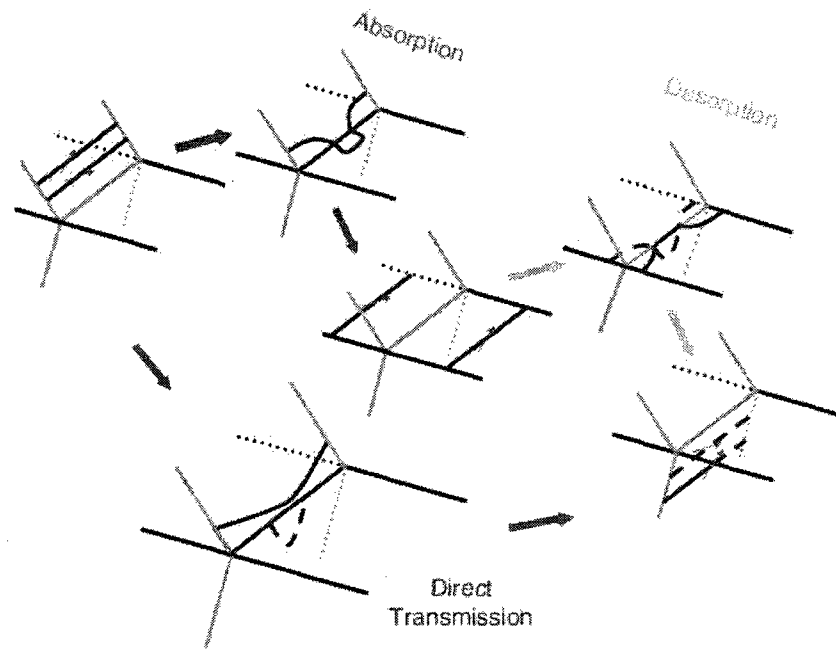


**Figure 2.22** Absorption, desorption and direction transmission of a screw dislocation at TB [20].

## 2.5 Analytical models

Various analytical models have been postulated by several researchers to describe the deformation behaviors of nanotwinned materials. Based on the experimental observations, Dao *et al.* [18] propose an analytical model that assumes the atoms at and adjoining the twin boundaries are more heavily involved in plastic deformation than the crystal interior, and named the region as the ‘twin boundary affected zone (TBAZ)’, shown in Figure 2.23. A TBAZ involves the atoms up to about 7-10 lattice parameters away from the twin boundaries, and is plastically softer (and more strain rate sensitive) than the crystal interior region between the TBAZs [18]. The authors also assume a significant shear deformation anisotropy parallel to and across the TBs. Since there exist no obstacles along the TBs, plastic deformation is expected to be easier and the critical resolved shear stress along this direction is considered to be the

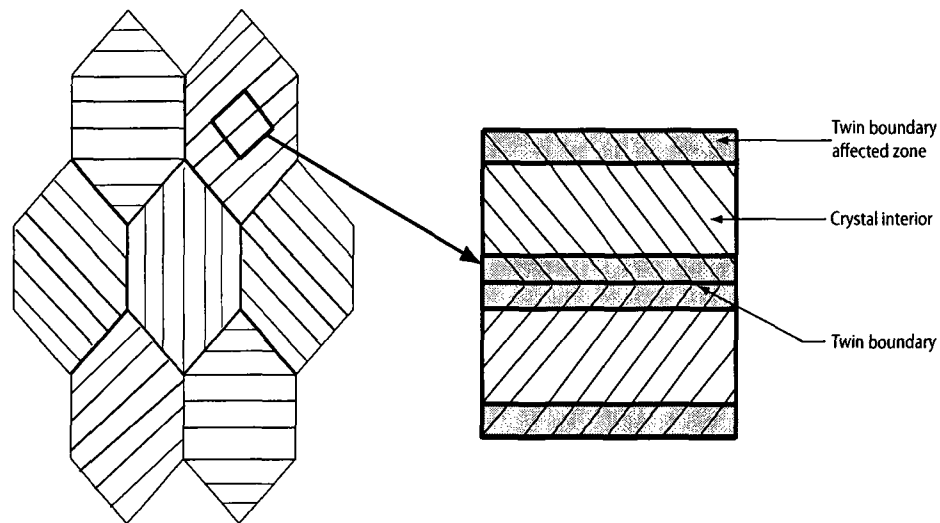


**Figure 2.23** Schematic diagram of the twin boundary affected zone (TBAZ) model, reproduced from [18].

same as that of the twin free grains. However, on the slip systems across the TBs, the shear deformation is considerably harder due to the presence of TBs and the critical resolved shear stress is assumed to be governed by the twin lamellae thickness [18]. Based on these assumptions, their model predicts the experimentally observed trends of the effects of twin density on flow strength, rate sensitivity, and ductility reasonably well beyond a certain critical twin lamellae spacing (13nm). Asaro and Suresh [44] develop a mechanistic model for the low activation volume and high rate sensitivity of metals with nanocrystalline grains and nanotwins. Their analysis correlates some key deformation behaviors such as: partial and full dislocation emissions from the GBs or the TBs, and the formation of deformation twins, in terms of intrinsic stacking fault energy, unstable stacking energy, and unstable twinning energy. This model assumes that the sliding of a grain boundary facet acts like a small crack, and becomes a source of stress concentration on the GBs [44]. Zhu *et al.* [20] propose a model that describes the origin of ductility in the nanotwinned samples in terms of the interaction of dislocations with the interfaces. In this model, the ductility of the nanotwinned

structures has been attributed to the hardening of twin boundaries as they gradually lose coherency during plastic deformation [20].

## 2.6 Summary and objectives of this work

Experimental investigations undertaken so far [17–19, 21, 41] have been carried out at comparatively larger scales (few hundreds of nanometers grain diameter with twin spacings of a few nanometers), and at realistic strain rates. However, these are not capable of exploring the detailed atomistic deformation mechanisms occurring at much smaller length scales that control the properties of these materials. On the other hand, atomistic simulation makes it possible to investigate materials deformation behavior at length scales where experimental investigations are not feasible. Computer simulations (such as molecular dynamics, MD) conducted by Yamakov *et al.* [30, 49], Froseth *et al.* [46, 47, 53], and Cao *et al.* [48] have been carried out efficiently at much smaller scales giving detailed insights of various atomistic deformation mechanisms, and the influence of stacking fault energy of various FCC nanotwinned structures, but are limited to extremely high strain rates. Moreover, the influence of underlying deformation mechanisms on the observed properties of nanotwinned structures has yet to be revealed. The aim of this present work is to address these important questions to help develop a complete understanding of this field of research.

Based on the above review of the literature the following goals have been set to be addressed in this present research work:

1. to understand the deformation behavior and overall stress-strain response of various Cu nanotwinned structures,
2. to relate resolved shear stress variation in various grains and along various slip planes to the deformation mechanisms,

3. to understand the dominant deformation pattern in each grain and the participation of various grains in the overall deformation process depending on their orientation with respect to the loading direction,
4. to systematically study the effects of twin width, grain size, grain orientation, and temperature on the atomistic deformation processes and the corresponding changes in the observed properties, e.g., strength and toughness, of nanotwinned copper,
5. lastly, to investigate an efficient way to refine the twin width and grain size that will help optimize the properties of these materials.

This present study will therefore be helpful to obtain valuable insights of various deformation characteristics, and subsequent changes in the macroscopic mechanical properties of nanotwinned structures. Moreover, this research will also contribute in developing the theory to describe nanotwinned materials' behavior.

# Chapter 3

## Computational approach

One of the primary motivations of computer simulation is the ability of this approach to deal with complex physical systems that are inaccessible through experiments. Experimental investigation of nanoscale materials not only requires strong expertise but also involves sophisticated equipments in every stage of sample preparation, deformation characterization, and property analyses. Whereas the fine microstructure of these materials enables scientists to apply various computational techniques to gain insight into the materials' behavior at the nanoscale and to predict their behavior under different circumstances quite precisely and efficiently.

### **3.1 Modeling schemes across scales: continuum to atomistic**

Among several computational modeling schemes, the appropriate choice depends on the type of the problem and scale of the physical phenomena under consideration. It is well understood that material properties are strongly affected by various phenomena occurring at different length scales. At the atomic scale, understanding of

atomic interactions and quantum mechanical descriptions are necessary to characterize materials behavior. At the nanometer scale, defects such as dislocations, their core structure, and the mechanisms of their nucleation and movement control mechanical behavior. At the larger scales, for example from tens to hundreds of micrometers, the effects of large collections of defects including GBs, dislocation pile-ups at the GBs, and other microstructural elements become significant, while at an engineering scale, contributions arising from macroscopic stresses and/or temperature gradients become profound and govern macroscopic material properties [25].

Continuum mechanics is the most effective route to determine the macroscopic response of materials under external stimuli such as mechanical loads or the application of electromagnetic fields. The concept of continuum mechanics ignores the features at ‘small’ scales such as the interaction between the atoms, and assumes the materials to be continuous, which means the matter in the body is continuously distributed and fills the entire region of space it occupies. A material may be assumed to be a continuum when the distance between the particles is very small compared to the physical dimension of the problem. The whole body is continually sub-divided into infinitesimal elements with properties being those of the bulk material. Continuum theories replace the kinematic description of materials in terms of atomic positions with field variables [54]. Therefore, the number of degrees of freedom is reduced to manageable proportions and can be applied to real size physical problems.

On the other hand, fully atomistic simulation schemes are essential to elucidate the atomic scale phenomena occurring at the nanometer scale. Defects such as dislocations, their core structure, and mechanisms of their nucleation and interaction with other defects have direct and strong influence on the macroscopic material behavior. The effect of these defects can not be captured completely through conventional theoretical modeling and computer simulations based on continuum approaches. There-

fore, those models must be used in conjunction with atomistic models to characterize materials behavior [55]. Atomistic modeling, however, cannot be used to simulate entire systems on the micrometer scale, because of the limitations of both data processing speed, and data storage capacity of the computers. The present state-of-the-art atomistic modelling schemes can work efficiently only at length scales well below the typical grain size [56]. To overcome this limitation, the field of multi-scale materials modeling has emerged, whereby atomistic modeling is coupled with larger scale continuum models to quantify the performance and behavior of materials across all relevant length and time scales [25]. The focus of this thesis, however, is to gain an understanding of the atomic scale behavior of nanocrystalline materials. Due to the fine microstructure of these materials, a fully atomistic treatment is considered to be both realistic and feasible.

## 3.2 Interatomic potentials

The mechanical behavior of materials is governed by the interactions between the constituent atoms. These atomic interactions not only define the atomic arrangement in a crystalline structure but also their arrangement in the dislocation core [57]. Therefore, accurate theoretical descriptions of interatomic potential functions are necessary in every atomistic simulation to study the collective behavior of atoms in a crystal. The accuracy and complexity of the potential determine the quality of the simulation results and the amount of computer time required [24]. The most obvious physical feature of interatomic interaction is that atoms repel when they are brought too close to each other. However, atoms attract each other at longer distance. Depending upon the atomic species some interatomic interactions are easy to describe and some other can be very complex, but the functional forms are based on the forces

exerted between the protons and electrons. Therefore, the most accurate interatomic interaction should be based on the solution of Schrödinger's equation for interacting electron clouds around each atom [57].

Density functional theory (DFT) is one of the earliest methods wherein simulations are aimed towards obtaining numerical solution of the complex quantum many-body Schrödinger equation of the atomic system [58]. The DFT calculation, therefore, provides a highly accurate description of the quantum mechanical behavior of the materials, and can obtain the ground-state energy of an atomic configuration. However, the applicability of this method is limited due to extremely high computational requirement. Current state-of-the-art DFT calculations are limited to system sizes of about a few thousand atoms, and modeling their behavior for about ten picoseconds. However, even with the use of massively parallel super computers, the computation time exceeds many days of CPU time [59]. Thus, it is essentially impossible to compute the mechanical response of a system of realistic dimension with this approach [22]. Despite this limitation, DFT calculations are used to calculate the energy or structure of critical atomic configuration, such as various metastable configurations, and generalized stacking fault configuration [59].

To overcome the limitation of system size associated with the DFT technique, scientist have developed simpler semi-empirical models for approximate descriptions of the interaction between particles. These semi-empirical models assume simplified form for the atomic interactions, and are often expressed as the potential energy functional of a collection of atoms,

$$V(\mathbf{x}_i) \equiv V(\mathbf{x}_1, \mathbf{x}_2, \dots, \mathbf{x}_N), \quad (3.1)$$

where  $\mathbf{x}_i$  is the position vector of atom  $i$  and  $N$  is the total number of atoms. This functional form is then fitted against experimentally measured quantities in such a

way that the parameters of the energy functional, which determine its numerical values, exactly reproduce those known experimental quantities [59]. Substitution of a simpler model allows one “to obtain quick qualitative results; to scan many cases to obtain trends; to investigate longer time scales; or to model a larger system”- as described by Voter [24]. The major problem of this approach is that while the functional form may reproduce some experimentally measured quantities reasonably well, there is a possibility that it may get other quantities completely wrong. Therefore, one functional form is only valid under certain conditions to reproduce certain experimentally measured quantities for the material of interest.

The simplest of such semi-empirical models is the *pair potential*, where the energy,  $E_{tot}$  of an arbitrary arrangement of  $N$  atoms is written as

$$E_{tot} = E_0 + \frac{1}{2} \sum_{i=1}^N \sum_{j \neq i}^N \Phi_{ij}(r_{ij}). \quad (3.2)$$

Here  $E_0$  is a constant,  $\Phi_{ij}$  is an energy potential that depends on the atomic species of both atoms  $i$  and  $j$ , and the distance between the  $i$ th and  $j$ th atoms,  $r_{ij}$ . The pair potential is limited in its applicability, because of the initial assumption that describes the potential energy as a sum of interactions between a pair of atoms. In reality very few materials can be described by pair potential with reasonable accuracy [57, 59].

### 3.2.1 Embedded atom method (EAM)

One way to overcome the limitations of pair potential is to construct a many-body potential energy. Daw and Baskes derived a method, the Embedded-Atom Method (EAM), based on density functional theory to calculate ground-state properties of realistic metal systems [60, 61]. The EAM theory views each atom as an impurity which is embedded in the host consisting of all other atoms. It is assumed that the host atoms each contribute some electron density to a site where the impurity will

be inserted. The energy associated with this insertion or the embedding energy of an atom  $i$  depends on the resulting host electron density at atomic position  $i$  and the species of the impurity. The total embedding energy of a system of  $N$  atoms is obtained by adding the individual atom energy contributions as

$$E_{\text{embed}} = \sum_{i=1}^N F_i(\bar{\rho}_i), \quad (3.3)$$

where  $\bar{\rho}_i$  is the host electron density at atomic position  $i$  due to neighboring atoms. The embedding energy  $F_i$  of an atom  $i$  is defined as the energy of that atom in a uniform electron gas of density  $\bar{\rho}_i$  relative to the atom separated from the electron gas. The function  $\bar{\rho}_i$  is found by linearly adding the electron densities of all neighboring atoms, and is expressed as

$$\bar{\rho}_i = \sum_{j \neq i}^N \rho_j(r_{ij}), \quad (3.4)$$

where  $\rho_j$  is the uniform electron density field that each atom experiences [57, 59, 60]. In addition to this, it is also necessary to consider the pair-wise interactions between two atoms to derive the exact form of the total energy. Therefore, in EAM, the total potential energy  $V$  of a configuration of  $N$  atoms is written as [60]

$$V = \frac{1}{2} \sum_{i=1}^N \sum_{j \neq i}^N \Phi_{ij}(r_{ij}) + \sum_{i=1}^N F_i(\bar{\rho}_i), \quad (3.5)$$

where  $\Phi_{ij}$  is a pair potential due to the interaction between two atoms,  $i$  and  $j$ , separated by an interatomic distance  $r_{ij}$ . In theory, the summations of  $i$  and  $j$  in equations 3.3–3.5 are over all the atoms,  $N$ . However in practice,  $j$  denotes only the neighboring atoms within some cutoff radius,  $r_{\text{cut}}$ , of atom  $i$ . This cutoff generally includes the first 2 or 3 neighbor distances in the crystal, beyond which atomic interaction is neglected [59]. Because of the non-linear embedding function, the EAM potential includes many-body effects that makes the EAM potential more realistic than a pair-wise potential [57]. The ground-state properties, i.e. lattice

constant, elastic constants, sublimation energy, and vacancy-formation energy of the solid can be calculated from Equation 3.5 [60]. The EAM is also capable of treating metallic system with cracks, surfaces, impurities and alloys. When treating impurities or alloys, it is necessary to know the embedding function for each element and pair potential for each pair of atomic species.

### 3.3 Molecular dynamics (MD) method

Among various methodologies of atomistic simulation, the Molecular Dynamics (MD) method is one of the most popular techniques to simulate the dynamics of a many-body particle system, and investigate the mechanical behavior of materials for which reliable interatomic potentials are available. In MD simulations, a physical system of  $N$  atoms, which are described as a number of interacting material points, is represented by a set of atomic coordinates,  $\{\mathbf{x}_i | i = 1, 2, \dots, N\}$ . The objective of the simulation is to compute the trajectories of the constituent particles following the laws of classical mechanics. The motion of a particle  $i$  is described through Newton's second law [62]

$$\mathbf{F}_i = m_i \frac{d^2 \mathbf{x}_i}{dt^2}, \quad (3.6)$$

where  $\mathbf{F}_i$  is the acting force on particle  $i$  of mass  $m_i$  and position vector  $\mathbf{x}_i$ , resulting in an acceleration  $\mathbf{a}_i = d^2 \mathbf{x}_i / dt^2$  of the particle. Therefore, in Newtonian dynamics, motion is a response to the applied force. If we consider an isolated system of  $N$  atoms moving in accordance with Newton's law, then the atomic trajectories are the time-dependent position vector  $\mathbf{x}_i(t)$ . However, as the atom position changes, its momentum also changes with time due to the interaction with other atoms, giving a time dependent momentum vector  $\mathbf{p}_i(t)$ . Therefore, at one instant, the state of the system can be fully specified by the positions and momenta of all atoms  $(\mathbf{x}_i, \mathbf{p}_i)$  [57].

Hamiltonian dynamics uses this concept and introduces a function of the positions and momentum of the particles, called the Hamiltonian  $H(\mathbf{x}_i, \mathbf{p}_i)$ , whose value is constant in time. The total energy of an isolated system, which is a conserved quantity, can also be identified as the Hamiltonian and can be expressed as [62]

$$H(\mathbf{x}_i, \mathbf{p}_i) = \sum_{i=1}^N \frac{|\mathbf{p}_i|^2}{2m_i} + V(\mathbf{x}_i), \quad (3.7)$$

where the first term on the right hand side is the sum of the kinetic energies of all atoms, and the second term denotes the total potential energy,  $V$ , of the system [57]. The momentum vector of atom  $i$  is expressed as  $\mathbf{p}_i = m_i \mathbf{v}_i$ , where  $\mathbf{v}_i = d\mathbf{x}_i/dt$  is its velocity. If we take the time derivative of Equation 3.7 we obtain

$$\begin{aligned} \frac{dH}{dt} &= \sum_i \frac{\partial H}{\partial \mathbf{p}_i} \cdot \frac{\partial \mathbf{p}_i}{\partial t} + \sum_i \frac{\partial H}{\partial \mathbf{x}_i} \cdot \frac{\partial \mathbf{x}_i}{\partial t} \\ &= \sum_i \frac{\mathbf{p}_i}{m_i} \cdot \frac{\partial \mathbf{p}_i}{\partial t} + \sum_i \frac{\partial V}{\partial \mathbf{x}_i} \cdot \frac{\partial \mathbf{x}_i}{\partial t} = 0 \end{aligned} \quad (3.8)$$

Equating the above two equations and making appropriate substitutions, we obtain the equations of motion in Hamiltonian dynamics [57, 62]

$$\frac{\partial H}{\partial \mathbf{p}_i} = \frac{\mathbf{p}_i}{m_i} = \frac{d\mathbf{x}_i}{dt} \quad (3.9)$$

$$\frac{\partial H}{\partial \mathbf{x}_i} = \frac{\partial V}{\partial \mathbf{x}_i} = -\frac{d\mathbf{p}_i}{dt} \quad (3.10)$$

These two first-order differential equations are equivalent to Newton's second-order equation shown in Equation 3.6. However, the only difference is that in Hamiltonian dynamics force does not appear explicitly, rather motion occurs in such a way to keep Hamiltonian function constant over time [62]. The connection between the Hamiltonian and Newtonian dynamics can be drawn by extending Equation 3.10, which leads to

$$\frac{d\mathbf{p}_i}{dt} = m_i \frac{d\mathbf{v}_i}{dt} = m_i \frac{d^2 \mathbf{x}_i}{dt^2} = -\frac{\partial V}{\partial \mathbf{x}_i}. \quad (3.11)$$

The above equation is nothing but another form of Newton's second law (as shown in Equation 3.6). Therefore, the force  $\mathbf{F}_i$  on atom  $i$  can be written as the negative derivative of interatomic potential function  $V(\mathbf{x}_i)$  with respect to the position of the atom  $\mathbf{x}_i$

$$\mathbf{F}_i = m_i \frac{d^2 \mathbf{x}_i}{dt^2} = \frac{-\partial V(\mathbf{x}_i)}{\partial \mathbf{x}_i}. \quad (3.12)$$

This is the fundamental equation of an MD simulation to compute the atomic movement explicitly at each time step. An MD algorithm, therefore, aims to find a solution of the above differential equation through numerical integration with a finite time step [22]. Integrating Equation 3.12 once yields the atomic momenta. A second time integration produces the atomic positions. Repeatedly integrating for several thousand times produces trajectories of individual atoms [62]. MD simulation permits atomistic simulation of complex problems involving billions of atoms and a simulation period on the order of nano-seconds [63].

### 3.3.1 Energy minimization and velocity initialization

Before starting the actual dynamics, it is important to minimize the potential energy of the initial atomic configuration. Among various energy minimization schemes the conjugate gradient and the steepest-descent methods are widely used. Depending on the initial atomic positions, both of these schemes converge iteratively to a local energy minima, which may not be the global minimum of the energy function. The relaxed configuration thus obtained corresponds to the state of zero temperature or zero atomic velocities.

To bring the relaxed configuration to a state of thermal equilibrium, initial atom velocities are then randomized at a finite temperature to satisfy the Maxwell-Boltzmann distribution. An iterative velocity rescaling algorithm is followed to minimize the temperature fluctuations and bring the system temperature close to the set temperature.

Interested readers are referred to Appendix A and Appendix B for the details of the conjugate gradient and velocity initialization algorithm, respectively. It is important to emphasize that, velocity initialization is done only at time  $t = 0$ ; before the actual dynamics begins. Finite temperature MD simulations using a temperature thermostat (e.g., Nosé-Hoover thermostat) apply a different technique to control the system temperature. Detailed discussion on this topic will be presented later in Section 3.3.4.

### 3.3.2 Velocity-Verlet algorithm

The Velocity-Verlet algorithm is a commonly used technique of finding atomic trajectories by numerically solving Newton's second law over time. The actual dynamics begins with a system at thermal equilibrium at a finite temperature. Thereafter an appropriate loading is applied by tiny increments at each time step. The choice of time step is very crucial in every MD simulation. An appropriate time step should be small enough to ensure the highest level of stability and accuracy, and should also be large enough to make the simulation efficient. To find atomic trajectories, the Velocity-Verlet algorithm calculates the new position of a particle at time  $t + \Delta t$  from its position, velocity, and acceleration at time  $t$ . Then velocities at the "half step"  $t + \Delta t/2$  are calculated as [57]

$$\mathbf{x}_i(t + \Delta t) = \mathbf{x}_i(t) + \mathbf{v}_i(t)\Delta t + \frac{1}{2}\mathbf{a}_i(t)(\Delta t)^2, \quad (3.13)$$

$$\mathbf{v}_i(t + \frac{\Delta t}{2}) = \mathbf{v}_i(t) + \frac{\mathbf{a}_i(t)(\Delta t)}{2}. \quad (3.14)$$

Accelerations at step  $t + \Delta t$ ,  $\mathbf{a}_i(t + \Delta t)$ , are obtained from the total force on each particle. Finally, velocities at step  $t + \Delta t$  are obtained from velocities at the half step

$t + \Delta t/2$  and accelerations at step  $t + \Delta t$  [57]

$$\mathbf{a}_i(t + \Delta t) = -\frac{1}{m_i} \frac{\partial V(\mathbf{x}_i(t + \Delta t))}{\partial \mathbf{x}_i(t + \Delta t)}, \quad (3.15)$$

$$\mathbf{v}_i(t + \Delta t) = \mathbf{v}_i(t + \frac{\Delta t}{2}) + \frac{\mathbf{a}_i(t + \Delta t)\Delta t}{2}. \quad (3.16)$$

This algorithm assumes that acceleration at time  $\mathbf{a}(t + \Delta t)$  only depends on position  $\mathbf{x}(t + \Delta t)$ , and does not depend on velocity  $\mathbf{v}(t + \Delta t)$ , which is the case for atomistic systems. However, the above algorithm needs to be updated for MD simulations using the Nosé-Hoover thermostat. The modified algorithm and solution procedure will be presented in Section 3.3.4.

### 3.3.3 Periodic boundary condition

In a small MD system, a large fraction of atoms are located on the surface of the domain and may not have proper atomic coordination for the interatomic interactions. This may induce spurious surface effects that dominate the properties of the small systems. Thus, MD simulation of a small system will provide information of the behavior of the material near the surface but not in the bulk [62]. This problem can be overcome by implementing the concept of the periodic boundary condition. To use the periodic boundary condition, a system of  $N$  atoms confined to a volume  $V$ , is imagined to be representative of the bulk material. The volume  $V$  is known as the primary cell and it is assumed that the bulk is composed of the primary cell that periodically replicates itself in all directions. These replicas are called image cells. Each image cell has the same shape, size and volume as the primary cell and contains the same number of atoms. Therefore, the atoms in each image cell are the images of the atoms in the primary cell and move exactly in the same way. During the simulation, as an atom leaves the primary cell, one of its images will enter through the opposite face. Moreover, the atoms near the boundaries interact with

the atoms residing within the cutoff radius across the boundaries. This interaction permits the atoms near the surfaces to see their full neighbors similar to the atoms inside the bulk and is required for accurate force and energy calculation. Hence, the physical behaviors and properties of the primary cell can represent the corresponding macroscopic sample of interest. Figure 3.1 shows the periodic boundary condition applied in two dimensions, where the shaded central box is the primary cell that has periodic copies all around it.

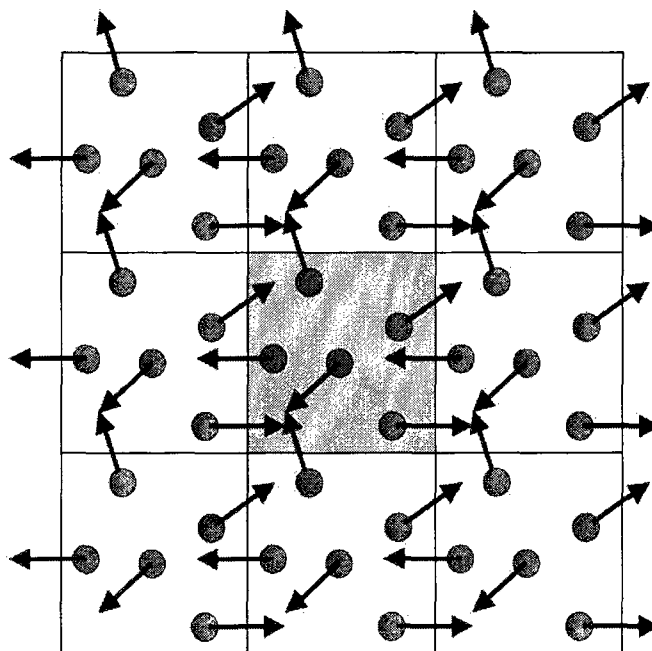


**Figure 3.1** Schematic diagram of the periodic boundary condition. The shaded box in the middle is the primary cell, and the boxes around it are the image cells. Reproduced from [64].

### 3.3.4 Nosé-Hoover thermostat

Use of a thermostat in MD simulation is essential to perform constant temperature simulation. The idea behind the Nosé-Hoover thermostat was originally developed by

Nosé [65] by introducing a new coordinate variable  $s$  and its conjugate momenta  $p_s$ , to mimic heat exchange between a large reservoir (or heat bath) with the atomistic sub-system.  $s$  serves as a scaling factor of time that distorts the atomic trajectories, but, helps maintain the prescribed temperature of the atomistic sub-system. The Hamiltonian of this system is postulated as [65]

$$H_{Nose} = \sum_i \mathbf{p}_i^2 / 2m_i s^2 + V(\mathbf{x}_i) + p_s^2 / 2M_s + 3Nk_B T \ln s, \quad (3.17)$$

where the first two terms on the right hand side represent the total energy of the atomistic sub-system, whereas, the last two terms represent the total energy of the reservoir. The equations of motion derived from the above Hamiltonian had been simplified by Hoover [66] by introducing the thermodynamic friction coefficient  $\xi$ . The equations of motion then become

$$\frac{d\mathbf{x}_i(t)}{dt} = \mathbf{v}_i(t), \quad (3.18)$$

$$\frac{d\mathbf{v}_i(t)}{dt} = \frac{\mathbf{f}_i(t)}{m_i} - \xi(t)\mathbf{v}_i(t), \quad (3.19)$$

$$\frac{d\xi(t)}{dt} = \frac{1}{M_s} \left[ \sum_{i=1}^N m_i |\mathbf{v}_i(t)|^2 - 3Nk_B T \right], \quad (3.20)$$

$$\frac{ds(t)}{dt} = s(t)\xi(t), \quad (3.21)$$

as suggested by Hoover [57, 66, 67]. Here,  $M_s$  is defined as a thermal “mass” parameter associated to  $s$ , which controls the rate of heat exchange between a large reservoir with the atomic sub-system. When the instantaneous temperature exceeds the desired target temperature  $T$ , the kinetic energy of the system increases, and  $\xi$  increases as well. Once  $\xi$  becomes positive, a viscous drag force is exerted on all atoms, resulting in a reduced atomic velocities and lower instantaneous temperature. This feedback system allows the instantaneous temperature to oscillate around the desired temperature  $T$  [57].

Therefore, the numerical implementation of Nosé-Hoover dynamics involves modification of the original Velocity-Verlet algorithm outlined in Section 3.3.2 to consider the effects of the thermostat. For the Nosé-Hoover equations of motion (Equation 3.18-3.21) the Velocity-Verlet algorithm becomes [67]

$$\mathbf{x}_i(t + \Delta t) = \mathbf{x}_i(t) + \mathbf{v}_i(t)\Delta t + [\mathbf{f}_i(t)/m_i - \xi(t)\mathbf{v}_i(t)] \frac{\Delta t^2}{2}, \quad (3.22)$$

$$\mathbf{v}_i(t + \Delta t/2) = \mathbf{v}_i(t) + [\mathbf{f}_i(t)/m_i - \xi(t)\mathbf{v}_i(t)] \frac{\Delta t}{2}, \quad (3.23)$$

$$\ln s(t + \Delta t) = \ln s(t) + \xi(t)\Delta t + \left( \sum_i m_i \mathbf{v}_i^2(t) - 3Nk_B T \right) \frac{\Delta t^2}{2M_s}, \quad (3.24)$$

$$\xi(t + \Delta t/2) = \xi(t) + \left( \sum_i m_i \mathbf{v}_i^2(t) - 3Nk_B T \right) \frac{\Delta t}{2M_s}, \quad (3.25)$$

$$\mathbf{v}_i(t + \Delta t) = \mathbf{v}_i(t + \Delta t/2) + [\mathbf{f}_i(t + \Delta t)/m_i - \xi(t + \Delta t)\mathbf{v}_i(t + \Delta t)] \frac{\Delta t}{2}, \quad (3.26)$$

$$\xi(t + \Delta t) = \xi(t + \Delta t/2) + \left( \sum_i m_i \mathbf{v}_i^2(t + \Delta t) - 3Nk_B T \right) \frac{\Delta t}{2M_s}. \quad (3.27)$$

These equations are solved in two steps. In the first step, Equations 3.22-3.25 are solved without any difficulty. It is important to note that velocity and friction coefficient values are updated to the intermediate values at time  $t = t + \Delta t/2$ , which is similar to the original Velocity-Verlet algorithm. However, the problem arises in the second step, which involves full update of  $\mathbf{v}_i$  and  $\xi$ . Unlike the actual Velocity-Verlet algorithm, in the Nosé-Hoover dynamics acceleration depends on velocity. Therefore, the updated velocity  $\mathbf{v}_i(t + \Delta t)$  appears on both sides of Equations 3.26 and 3.27. Some MD codes treat these equations as implicit equations, and solve them iteratively. However, the MD package that has been used in the research follows an “explicit reversible integrator” technique of Martyna *et al.* [68] to solve these equations explicitly. This new formulation is suitable for extended system dynamics (e.g., Nosé-Hoover dynamics), and more efficient than standard iterative schemes.

## 3.4 Visualization techniques

The outputs from MD simulations are simply the coordinates of all the atoms of the system. In order to investigate the underlying deformation mechanisms, it is necessary to filter out the uninteresting atoms that are not associated with the defects directly. To identify the location and character of the nucleated defects, and visualize the nucleation and evolution process of the defects, two visualization techniques, the centrosymmetry parameter [69] and the slip vector analysis [70], are used in this present work. A brief description of these two techniques are presented below.

### 3.4.1 Centrosymmetry parameter (CSP)

In most crystal structures, every atom holds a unique relation with its surrounding atoms, such that if a line is drawn through an atom, there exist two identical atoms at the same distance on the either side of the given atom along that line. This is known as the centrosymmetry of the crystal. The FCC crystal is also centrosymmetric, where every atom has twelve nearest-neighboring atoms, and each atom in the lattice has pairs of equal and opposite bonds to its nearest neighbors. Under homogeneous deformation, these equal and opposite bonds change direction and/or length, but hold the centrosymmetric relationship [69]. However, when a defect is nucleated or the material is deformed plastically, the equal and opposite relation no longer holds for all of the nearest-neighbors pairs and centrosymmetry breaks down. The centrosymmetry parameter, CSP, is used to quantify the departure from perfect centrosymmetry. It is defined as [69]

$$\text{CSP} = \sum_{i=1}^6 |\mathbf{R}_i + \mathbf{R}_{i+6}|^2,$$

where the  $\mathbf{R}_i$  and  $\mathbf{R}_{i+6}$  are the vectors corresponding to the six pairs of opposite nearest neighbors in the FCC lattice. The centrosymmetry parameter is zero for an

atom under any homogeneous elastic deformation and non-zero for an atom which is close to a defect or the free surface [69, 71].

### 3.4.2 Slip vector (SV) analysis

In order to monitor the evolution of nucleated dislocation, and to obtain quantitative information regarding the Burgers vector of the slip plane, a quantity, called the slip vector ( $\mathbf{s}^i$ ), can be defined for every atom  $i$  in the crystal. The slip vector was first introduced by Zimmerman *et al.* [70], and is defined by the following expression

$$\mathbf{s}^i = \frac{1}{n_s} \sum_{j \neq i}^{n_s} (\mathbf{r}_{ij} - \mathbf{r}_{ij}^0),$$

where  $j$  is a nearest neighbor of atom  $i$ ,  $n_s$  is the number of slipped neighbors, and  $\mathbf{r}_{ij}$  and  $\mathbf{r}_{ij}^0$  are the vector differences of atoms  $i$  and  $j$  in the current and reference positions, respectively. Slipped neighbors are those atoms for which the magnitude of displacement of atoms  $i$  and  $j$  ( $|\mathbf{r}_{ij} - \mathbf{r}_{ij}^0|$ ) exceeds one fifth of the Shockley partial dislocation. The reference configuration is the relaxed atomic configuration at zero mechanical stress. Any inhomogeneous deformation near an atom causes a large magnitude of the slip vector, which measures the Burger's vector for the slip of adjacent atomic planes. Moreover, the components of the slip vector help to identify the character of the dislocation [70].

### 3.4.3 Understanding CSP and SV plots

As discussed in the previous sections, CSP and SV parameters help detect the defects inside the crystal. However, it is important to interpret these results correctly, as various defects (partial/full dislocation, stacking fault, twinning fault, twin migration etc.) have their unique form in each plot of these two parameters. In the next chapter, the deformation behavior of nanotwinned samples will be analyzed based on

CSP and SV plots. Therefore, the following discussion will demonstrate the technique to interpret these plots correctly and determine the exact nature of the defects. For an atom at a perfect lattice site, both CSP and SV possess a zero value. Once a defect is present both of these two parameters obtain certain magnitude. Therefore, a minimum range is set to filter out those atoms located at the perfect lattice positions or below the minimum range, which makes visible those atoms associated with the defects.

In FCC crystals the closed-packed planes are  $\{111\}$  planes, which are also the glide planes and coherent twin planes. Since the twin orientation corresponds to a mirror reflection of the original crystal about the  $\{111\}$  plane, the stacking sequence will also be a mirror symmetry of the original sequence. Figure 3.2(a) [14] shows the stacking sequence of the coherent twin boundary, where the black vertical line denotes the position of the twin plane. A CSP plot makes most of the atoms invisible which are at the perfect FCC lattice sites (CSP=0), however, the twin boundary planes can be seen as a single plane of atoms in a HCP environment, as seen in Figure 3.2(b). In other words, in a CSP plot, atoms on the twin plane see ...BCB... sequence of atomic planes, and therefore obtain certain CSP values and become visible. However, atoms on the adjacent plane on either side of the twin boundary see ...ABC.... sequence (CSP=0), and hence become invisible. A slip vector plot, on the other hand, will not show a twin boundary unless the SV filter is removed to make all the atoms visible, and/or the twin boundary is displaced or migrated to a new position during the deformation process. Slip vector plots showing TBs at original and migrated positions will be presented later in Figure 4.7(d) of Section 4.6.3.

Now consider another type of fault. Suppose that all planes are in a perfect FCC sequence ABCABC.... If one of the planes and all planes above it are displaced by the vector  $1/6[\bar{2}11]$ , that results in an intrinsic stacking fault. This shear displacement

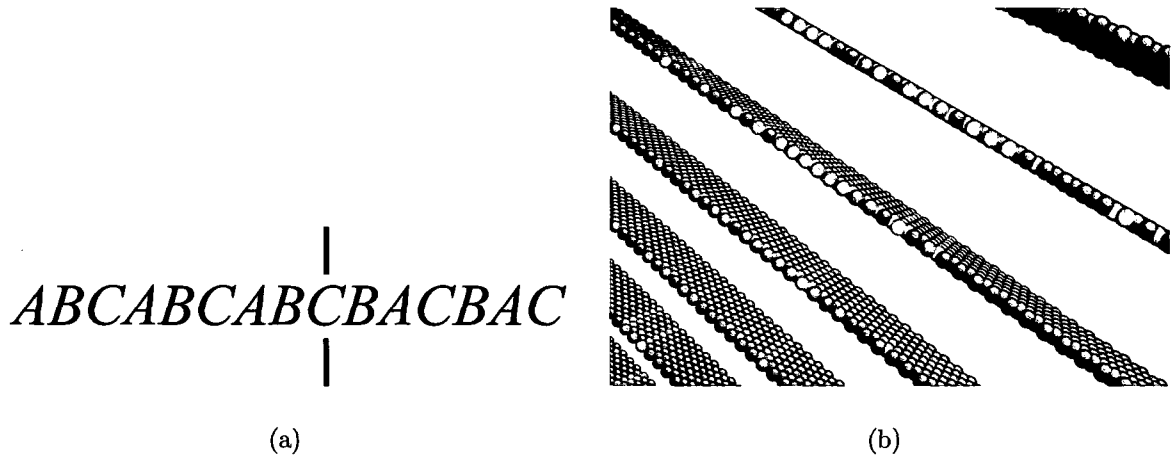


**Figure 3.2** (a) Stacking sequence of a coherent twin boundary (CTB). (b) CSP plot showing CTBs as a single plane of atoms in a HCP environment. Other atoms located in a FCC environment are invisible due to the CSP filter.

is represented by the arrows in Figure 3.3(a), and the resulting fault is shown in (b) with the black vertical lines [14]. Atoms located on both highlighted *A* and *C* planes see a HCP stacking sequence, ...*CAC*... and ...*ACA*..., respectively, whereas the rest of the atoms see a regular FCC sequence. Therefore, in a CSP plot, an intrinsic stacking fault is seen as two adjacent planes of atoms in a HCP sequence, as shown in Figure 3.3(c). A SV plot also shows two atomic planes, one on either side of the plane of slip, as shown in (d).

A third possible defect occurs if the planes below  $\bar{A}$  of an intrinsic stacking fault, as shown in Figure 3.4(a), are displaced by  $1/6[2\bar{1}1]$ , called an extrinsic stacking fault. The formation mechanism and the resulting fault are shown in Figure 3.4(a & b), respectively [14]. Atoms on both *B* and *C* plane see a HCP stacking sequence, however, atoms on the intervening *A* plane see a FCC sequence, ...*BAC*.... Therefore, in a CSP plot, an extrinsic stacking fault is seen as two neighboring HCP planes separated by an invisible FCC plane in between, as shown in Figure 3.4(c). However,



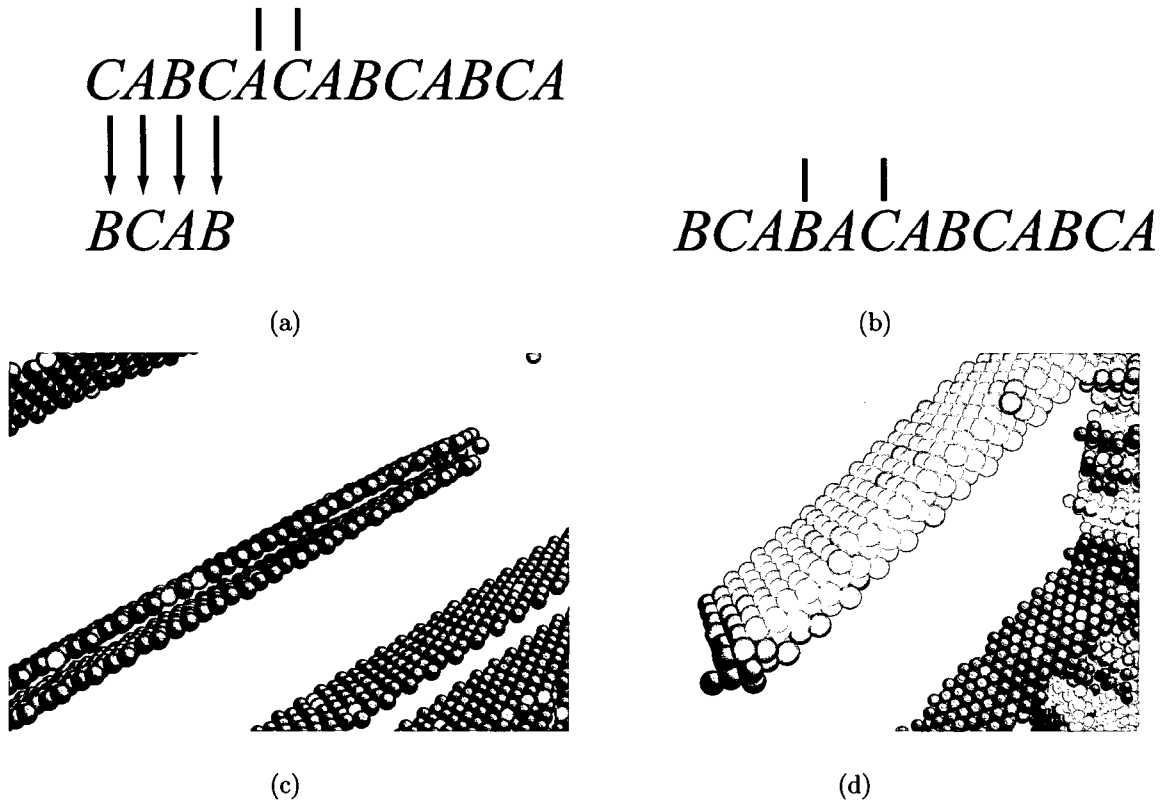


**Figure 3.4** (a) Formation of an extrinsic stacking fault, (b) stacking sequence of an extrinsic stacking fault, (c) CSP and (d) SV plots showing an extrinsic fault.

The trailing partial is therefore located in the middle of the two colored atoms. In contrast, a CSP plot (as shown in Figure 3.5(b)) will only show the atoms at the stacking fault, as they see a HCP environment. But the red atoms of Figure 3.5(a) will not be visible in this figure as they have gone through a full slip and returned back to the initial FCC stacking sequence.

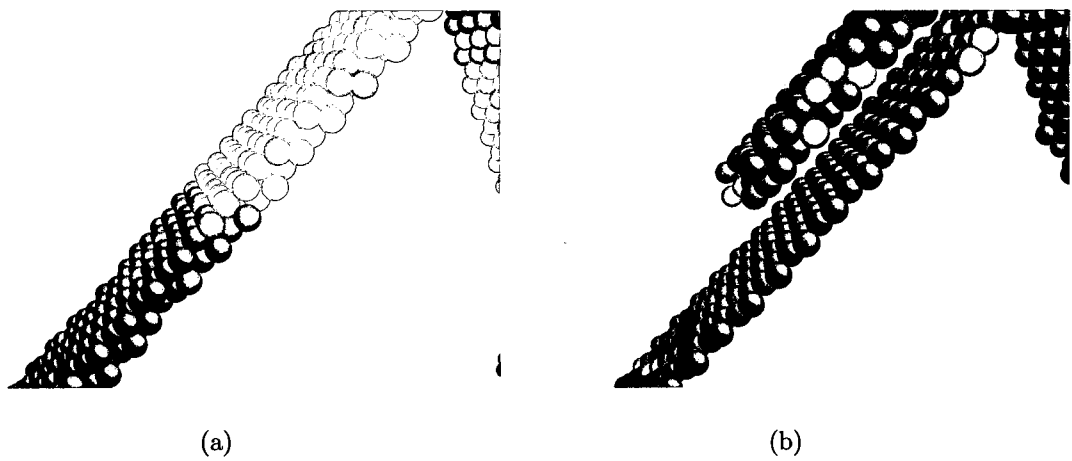


**Figure 3.5** (a) SV plot showing the slipped perfect crystal, trailing partial dislocation, and stacking fault between leading and trailing partials. (b) CSP plot showing the atoms at the stacking fault and a TB underneath. The atoms that have experienced full slip are not visible in this picture.

# Chapter 4

## Deformation Behavior and Stress-Strain Response

### 4.1 Model description

To analyze the deformation behavior and responses of the nanotwinned structure, a computation model (or cell) has been built using a series of computer programs written in FORTRAN. The computational cell contains four hexagonal grains of FCC copper with lattice constant  $3.615\text{\AA}$ . The copper is modelled using the EAM potential of Foiles *et al.* [50]. The grains are equiaxed (approximately 30nm in diameter) and separated by narrow grain boundaries. The cell dimensions along the x and y directions are approximately 50nm and 60nm, respectively. However, the thickness of the cell along the z direction is kept small at  $\sim 15\text{\AA}$ . As such, we model 2D columnar grains as a simplified surrogate for the full 3D grain structure. Figure 4.1(a) shows the x-y projection of the model at an unrelaxed state, where the black box denotes the approximate initial simulation cell size. The simulation is periodic in all three coordinate directions, creating an infinite array of columnar grains. This

initial unrelaxed configuration is then relaxed via conjugate gradient (CG) energy minimization. The details of the CG algorithm can be found in Appendix A. Figure 4.1(b) shows the relaxed configuration of the model, in which the atoms at the perfect FCC sites are shown in grey, and the grain boundary atoms are made visible by various other colored atoms, i.e., red, green, and blue. Visualization of the atoms is done using AtomEye- an atomistic configuration viewer [72]. This periodic simulation cell contains approximately 400,000 atoms, and the relaxed grains are completely dislocation free.

Figure 4.1(c) depicts the centrosymmetry parameter (CSP) plot of all the atoms at the relaxed state, which makes only the GB and TB atoms visible. Each grain is oriented with  $[1\bar{1}0]$  along z, but with various rotations in the x-y plane. Specifically, the  $[11\bar{2}]$  direction is oriented at  $0^\circ$ ,  $30^\circ$ ,  $60^\circ$ , and  $90^\circ$  from the x-axis in grains 1, 2, 3, and 4, respectively. Within each grain, the TBs represent the  $\{111\}$  crystallographic planes with a misorientation angle of  $70.53^\circ$  or  $[110]\Sigma 3(111)$  tilt boundaries. The rotational angle of each grain also signifies the orientation of the TB planes ( $\{111\}$  planes) within the respective grain from the x-direction ( $0^\circ$ ,  $30^\circ$ ,  $60^\circ$ , and  $90^\circ$  from the x-axis in grains 1, 2, 3, and 4, respectively). Due to the columnar structure of the model, all dislocation lines will be parallel to the  $\langle 110 \rangle$  columnar axis (z-direction), and following their nucleation dislocations can glide only on either of the two active  $\{111\}$  slip systems in each grain. In this present work six different nanotwinned models have been investigated by varying the twin spacings (between 3 – 15nm) to observe the effects of the twin widths on the deformation behavior. From now on, these models are referred to as: (i) 1-twin model (twin width  $\sim 15\text{nm}$ ), (ii) 3-twin model (twin width  $\sim 10\text{nm}$ ), (iii) 4-twin model (twin width  $\sim 7.5\text{nm}$ ), (iv) 5-twin model (twin width  $\sim 6\text{nm}$ ), (v) 7-twin model (twin width  $\sim 4.3\text{nm}$ ), and (vi) 10-twin model (twin width  $\sim 3\text{nm}$ ). Deformation behaviors and properties of these

nanotwinned structures have also been compared with a model of the same grain size but without any embedded TBs, and referred to as the no-twin model (twin-free sample).

## 4.2 Grain and twin boundary structure

A GB is an interface that is formed due to orientation mismatch between two adjacent grains in a polycrystalline metal. The structure and energy of the GB depend on the orientation of the two grains, as well as the orientation of the boundary plane itself. When two crystals preferentially align themselves with a common  $\{111\}$  plane a coherent twin boundary (CTB) is formed. Therefore, a CTB is nothing but a highly ordered and symmetrical GB. Figure 4.2(a) shows an example of a CTB, which is formed between two crystals (1 and 2), one with a crystal orientation  $[11\bar{2}]$ ,  $[111]$ , and  $[1\bar{1}0]$  along the x, y, and z direction, respectively, and the other a mirror symmetry of the former around the x-direction. A TB thus formed is designated as a  $[110]\Sigma 3(111)$  tilt boundary, where  $[110]$  denotes the rotational or tilt axis of the boundary plane, which is perpendicular to the plane of the paper (z-direction), and  $(111)$  is the boundary plane itself, which is the x-z plane with the y direction aligned to the boundary plane normal, as shown in Figure 4.2(a).  $\Sigma$  is a measure of symmetry of the boundary (those who are interested about the significance and measuring technique of  $\Sigma$  are referred to Appendix C for the details).

The angle of rotation of crystal 1 around the rotational axis is termed as the misorientation angle,  $\theta$ . In Figure 4.2(a),  $70.53^\circ$  between the two  $[001]$  directions of each of the bicrystals is the misorientation angle. The regular stacking sequence of closed packed  $\{111\}$  layers is inverted at the TB plane, and due to this highly symmetrical structure the energy of a CTB is very small compared to other GBs [73].

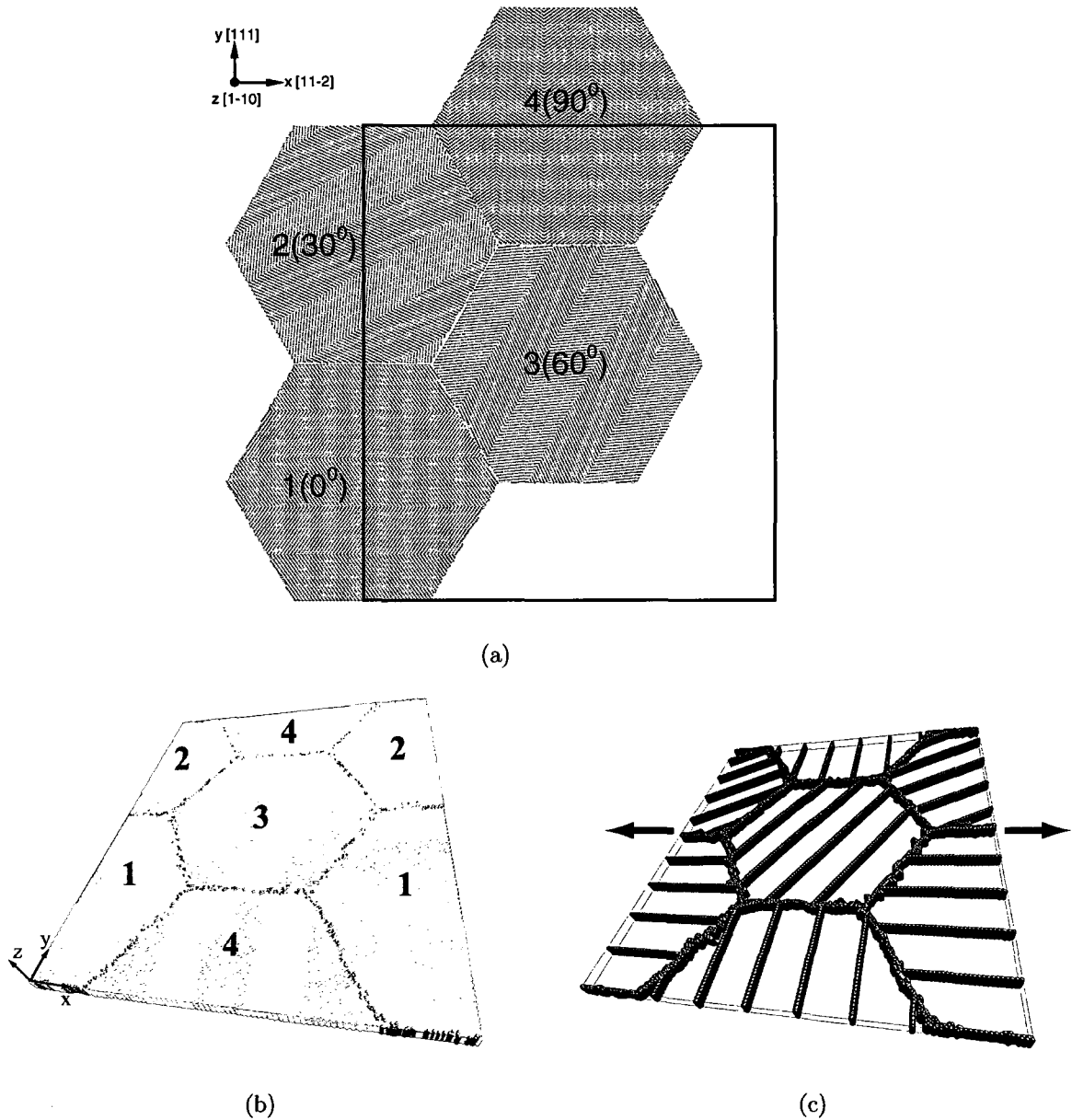


**Figure 4.1** (a) The x-y projection of the initial unrelaxed configuration of the nanotwinned structure. The grains are numbered from 1 to 4, and the rotational angle of each grain is shown in bracket. The black box denotes the approximate initial periodic cell size, (b) the relaxed configuration of the computational periodic cell showing four grains with embedded nanotwins. The portion of each grain which was outside the simulation cell (as shown in (a)) has been moved into the opposite side of the cell due to the periodicity. (c) shows the positions of the grain and twin boundaries using the CSP values as a filter. The arrows indicate the loading direction.

Figure 4.2(b) shows the GB energy variation with misorientation angle for different types of boundaries modelled using two different types of interatomic potentials. It is evident from this figure that the  $\Sigma 3(111)$  boundary (at  $\theta = 70.53^\circ$ ) possesses a very low energy for both of the potentials.

In general, the GBs are highly disordered structures. Due to the orientation mismatch between two neighboring grains, the atoms located closer to the edge of the grains do not have the same number of neighbors as those located inside the grains. Therefore, the GBs formed by these atoms possess much higher energy than the TBs. Figure 4.2(c) and (d) are two examples (the x-y projections of Figure 4.1(b)), illustrating atomic configuration inside and at the edge of different grains of our simulation model. The coloring of the atoms is based on the coordination number ( $CN$ ), where the atoms in grey (with  $CN=12$ ) form a crystalline structure, and are located well inside the grains. Whereas, the other colored atoms (with  $CN$  other than 12) are located at the edge of the grains forming a more disordered GB structure.

### 4.3 Grain and twin boundary energy calculation

Before performing the deformation simulations, it is necessary to ensure that both the GB and TB initial structures are reasonably representative of actual GB structures. To do so, the average TB energy ( $\gamma_{TB}$ ) is calculated initially in a separate bi-crystal model, as shown schematically in Figure 4.3. The model contains two FCC crystals separated by a common (111) TB plane, and is periodic in all three directions. The following expression is used to estimate the TB energy ( $\gamma_{TB}$ ),

$$\gamma_{TB} = (E_{tot} - N \times E_{coh}) / (A_{TB}), \quad (4.1)$$

where  $E_{tot}$  is the total energy of the system of  $N$  atoms containing TBs,  $E_{coh}$  is the cohesive energy, which is  $3.54 \text{ eV}/\text{\AA}^2$  for Cu modelled using one particular potential,

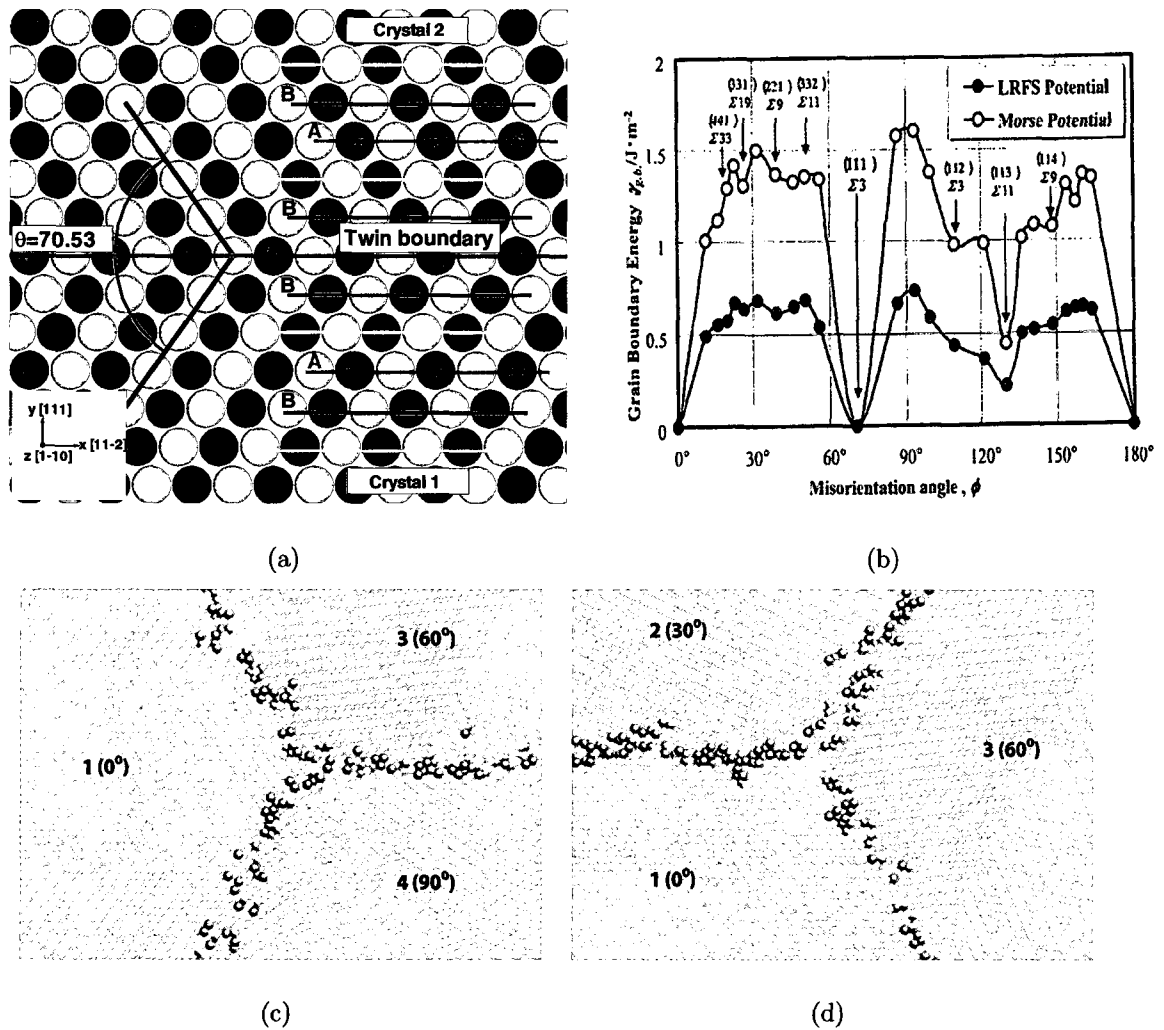


**Figure 4.2** (a) Structure of a  $[1\bar{1}0]\Sigma_3(111)$  twin boundary, viewing the  $\{111\}$  planes edge-on. The orientation of the bottom crystal is shown in the figure, whereas, the one on top possesses a mirror symmetry of the former around the  $x$ -axis. The color of the balls (blue or green) signifies their position on a different  $x$ - $y$  plane along the  $z$ -direction, and the same colored balls are located on the same  $(110)$  plane along the  $z$ -direction. (b) GB energy variation with misorientation angle for two different types of interatomic potentials [74]. (c and d) Atomic configuration inside and at the edge of different grains. The same grain number and rotational angle are maintained as Figure 4.1. The coloring is based on the coordination number of the atoms, where green=10, red=11, grey=12, and blue=13.

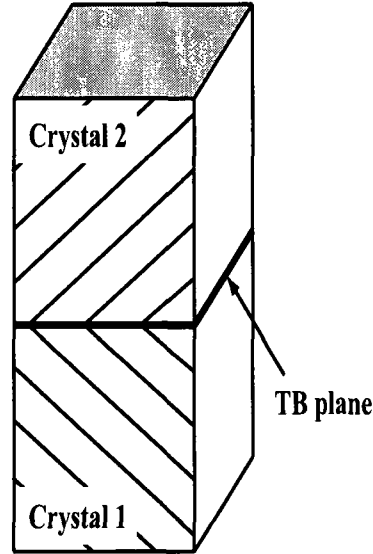


**Figure 4.3** Schematic diagram showing a bi-crystal model to measure the average TB energy. Crystal 1 and 2 share a common (111) TB plane. The shaded region is the TB area. The model is periodic in all three directions.

and  $A_{TB}$  is the total TB area. The above expression signifies the energy difference between two models, one with  $N$  atoms containing TBs (as shown in Figure 4.3), and the other with a perfect crystal of the same number of atoms, but without any TB. The energy difference is then divided by the total area of the TB planes to obtain a per unit area energy value. For the copper  $[110]\Sigma 3(111)$  TB, the energy is found to be  $5.5 \times 10^{-4} eV/\text{\AA}^2$ . This value allows us to estimate the average GB energy in our relaxed samples to be  $2.7 \times 10^{-2} eV/\text{\AA}^2$ , based on an accounting of all TB and GB area, and knowledge of the total energy as

$$\gamma_{GB} = (E_{tot} - N \times E_{coh} - \gamma_{TB} \times A_{TB}) / (A_{GB}), \quad (4.2)$$

where  $\gamma_{GB}$  is the average GB energy, and  $A_{GB}$  is the total GB area. These energy values are used as a check that the relaxed starting structures of our MD simulations are sensible, by ensuring the initial total potential energy is consistent with the total GB and TB areas contained in the periodic cell. Our GB energies and structures

compare favorably to detailed analyses on GB structure and energy of various tilt boundaries in Copper reported in [73–77].

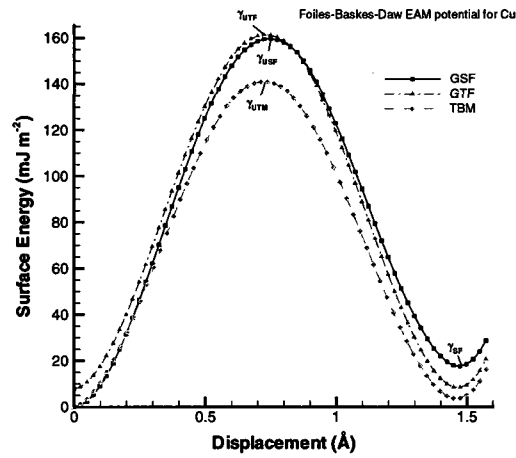
## 4.4 Generalized stacking fault energy curve calculation

As described earlier in Section 2.4.1, various generalized stacking fault (GSF) energy curves help gain an understanding of the origin of the observed deformation mechanisms among various other competing mechanisms within the microstructure. Therefore, we generate such GSF energy curves using the same Cu potential used in our simulations (the potential of Foiles *et al.* [50]), as plotted in Figure 4.4(a). These GSF curves are generated by molecular statics calculations following the same procedure mentioned in [34, 46, 52, 77, 78]; by rigidly displacing two blocks of perfect fcc crystal incrementally on a (111) plane along the  $[11\bar{2}]$  direction, as shown in Figure 4.4(b). For convenience, only the atoms near to the plane of displacement are shown. In order to ensure a stable configuration after the displacement, the maximum displacement of the top grain is chosen to exceed the Burgers vector of the partial dislocation of Cu ( $1.4758\text{\AA}$ ). The computational crystal is considered to be periodic along the x- and z-directions (the GB plane), however, a free boundary condition is imposed along the direction normal to the GB (y-direction). To eliminate the free-surface effects on the GB, the model is built large enough in the y-direction (40 {111} planes). During the simulation, the atoms located on the top grain (above the black line in Figure 4.4(b)) are displaced incrementally, while the atoms in the bottom grain remain fixed. As a (111) atomic plane glides past another, the energy per unit area of the slip plane increases to an unstable position,  $\gamma_{USF}$ , and then gradually decreases down to a stable position  $\gamma_{SF}$ , as shown by the GSF curve in Figure

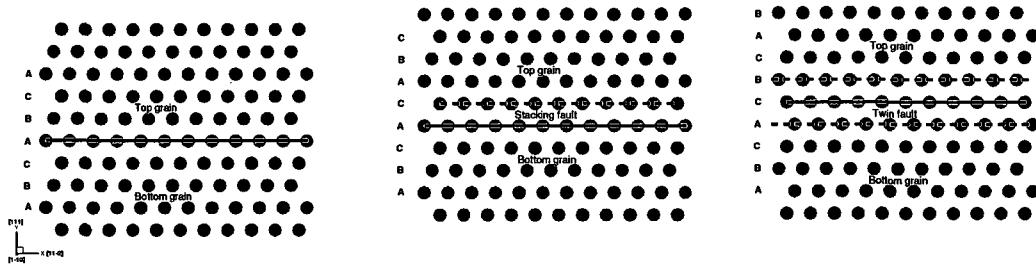
4.4(a). The unstable energy is related to the energy required in order to nucleate a partial dislocation, and once it propagates it leaves behind a stacking fault of energy,  $\gamma_{SF}$  [34]. The planar arrangement of the microstructure with intrinsic stacking fault is shown in Figure 4.4(c).

A twinning fault is then created using the bicrystal structure with an existing intrinsic stacking fault as an initial configuration, as shown in Figure 4.4(c), and displacing the atoms above the existing fault on the (111) plane and along the  $[11\bar{2}]$  direction. The generalized twin fault (GTF) energy curve and the microstructure thus obtained are shown in Figure 4.4(a) & (d), respectively. The GTF energy curve follows a similar trend as the GSF curve, reaches a slightly different maxima,  $\gamma_{UTF}$ , but ultimately comes back to the same initial stable energy level. The values obtained for  $\gamma_{USF}$ ,  $\gamma_{SF}$ ,  $\gamma_{UTF}$  agree reasonably well with other published results for various other potentials, as listed in Table 4.1.

To generate a twin boundary migration (TBM) energy curve, a separate bicrystal model is built, such that a  $\Sigma 3(111)$  twin boundary separates them at the interface, as shown in Figure 4.4(e). The crystal above the TB is displaced in the same manner, and the resultant energy curve is shown by the TBM curve in Figure 4.4(a). As the displacement of the top grain completes, the TB migrates into the neighboring (111) slip plane, as shown in Figure 4.4(f). The unstable energy for twin migration, ( $\gamma_{UTM}$ ), is found to be lower than the unstable stacking fault and twin fault energies obtained earlier. The ratio of various defect formation energies that determine the possibility of one deformation mechanism (either partial dislocation, full dislocation, twinning fault, or TB migration etc.) over the other competing mechanisms are listed on Table 4.1. A comprehensive discussion on this topic is presented in the next section.



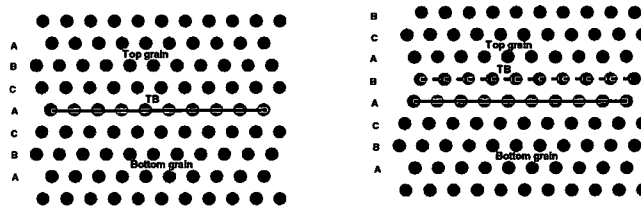
(a)



(b)

(c)

(d)



(e)

(f)

**Figure 4.4** (a) Generalized energy density curves of various defects obtained from EAM potential developed by Foiles *et al.* [50]. (b) The initial configuration of the bicrystal model to obtain the GSF curves. The atoms above the black line are displaced, whereas the atoms below the line remain free. The blue and green atoms are located in two adjacent (110) atomic planes. (c) Displaced configuration showing intrinsic stacking fault, (d) an atomic configuration showing twinning fault, (e) initial configuration used to generate TB migration energy curve, and (f) final configuration after TB migrates to the neighboring (111) plane.

Model [reported in]	$\gamma_{USF}$ ( $mJ.m^{-2}$ )	$\gamma_{SF}$ ( $mJ.m^{-2}$ )	$\gamma_{UTF}$ ( $mJ.m^{-2}$ )	$\gamma_{UTM}$ ( $mJ.m^{-2}$ )	$\frac{\gamma_{SF}}{\gamma_{USF}}$	$\frac{\gamma_{UTF}}{\gamma_{USF}}$	$\frac{\gamma_{UTM}}{\gamma_{USF}}$
Foiles <i>et al.</i> [present study]	<b>159.62</b>	<b>17.60</b>	<b>153.40</b>	<b>140.88</b>	<b>0.11</b>	<b>0.96</b>	<b>0.88</b>
Cleri-Rosato [34]	154.1	20.6	163.3	-	0.13	1.06	-
Schiotz-Jacobsen [34]	173.1	33.5	190	-	0.19	1.10	-
Mishin <i>et al.</i> [52]	185.17	29.49	168.67	-	0.16	0.91	-
Oh-Johnson [78]	158.0	27.0	-	-	0.17	-	-
Voter-Chen [78]	175.0	37.0	-	-	0.21	-	-

**Table 4.1** Planar fault energy densities ( $\gamma_{USF}$ ,  $\gamma_{SF}$ ,  $\gamma_{UTF}$ , and  $\gamma_{UTM}$ ) for various potentials. The values measured for the Cu EAM potential used in this present study are shown in bold. Also listed are the values for various other EAM and tight binding potentials reported in the literature enclosed in [ ].

## 4.5 Deformation procedure

A state-of-the-art parallel molecular dynamics simulation package, LAMMPS [79], is used to simulate the behavior of the copper nanotwinned structure under approximately uniaxial tensile deformation. At the beginning of each simulation and before applying the tensile deformation, a Gaussian distribution of the velocities of all the atoms is generated using a random number generator at a specific temperature. The structure is then deformed by applying a constant tensile engineering strain rate along the x-direction. The other two directions (y and z) are also strained by allowing those directions to shrink to keep their relative aspect ratio and the periodic cell volume constant. The simulations are performed in constant NVT ensemble (fixed number of atoms, volume and temperature). While it is true that the volume will not stay constant for a general loading (or uniaxial stress), we have chosen to control the strains in such a way that the volume is constant. This means that our stress state

is multiaxial, but still a valid way to load the crystal.

Atomic positions, velocities, and accelerations are updated at each time step using the Velocity-Verlet algorithm. The total simulation time is set at 300ps with a time step of 0.001ps. This short time period results in a very high strain rate, inherent to every MD simulation, but is necessary to obtain a significant amount of deformation within a reasonable simulation time. For our simulations, the applied strain rate is  $4.0 \times 10^8 s^{-1}$ , which allows the structure to deform  $\sim 65 \text{Å}$  in 300ps, or  $\sim 12\%$  of strain in the x-direction. In other words, the box length will increase 0.04% of its original length in every picosecond in this direction. The temperature of the simulations is controlled using a Nosé-Hoover temperature thermostat set to a constant temperature, either 0, 100 or 300K. Due to the large volume of data generated in each time step, only the atomic coordinates, periodic lengths, and atomic stresses are stored every 6ps for post-processing.

## 4.6 Deformation behavior of the crystal

The focus of the rest of this chapter is to present the observed deformation behavior and stress-strain response of various nanotwinned Cu examined in this research. First, in the following few subsections, several important deformation behaviors observed in our simulations are discussed. Afterwards, the stress vs. strain relationship of various nanotwinned models are examined, and the effects of twin width on the maximum stress values are compared at various temperatures. Later, the resolved shear stress (RSS) values of each grain are calculated by resolving the global stress tensors of each grain onto appropriate slip planes. The variations of the RSS and the corresponding changes in the deformation processes of different grains are also compared.

The key processes observed during the deformation of the nanotwinned models

include partial and full dislocation emission and propagation along and across the TBs, twin boundary migration and change in twin width, formation of deformation twins, dislocation pile-up and transmission across the TBs, formation of TB steps, dislocation emission from the steps, and grain boundary sliding. Yamakov *et al.* [49], Cao and Wei [48], and Froseth *et al.* [46] also investigated the deformation behaviors of TBs in nanocrystalline Al and Cu. The following few paragraphs describe some of our observations briefly.

### 4.6.1 Dislocation nucleation along and across the TBs

Within each grain of our model, there are generally two sets of slip planes, because the short periodicity along  $z$  prevents slip on the other two sets of planes. One of the active sets run parallel to the TBs, while the other intersects the TB at an angle of  $110^\circ$ . For brevity, we will refer to these slip planes as being “along” or “across” the TB, respectively. The GBs, triple junctions, and the intersection points of the TBs with the GBs are found to be the most probable sites for dislocation nucleation during the initial stages of deformation. Figure 4.5(a) illustrates the emission of partial dislocations along and across the TBs. Once nucleated, dislocations move through the grains gliding along two slip systems,  $\langle 11\bar{2} \rangle(111)$  and  $\langle 112 \rangle(11\bar{1})$ . Dislocations moving along the TBs experience no obstacles and glide through the entire grain, however, dislocations are blocked by the TBs in the other slip system, as shown in Figure 4.5(b). Figure 4.5(c) shows the corresponding slip vector plot of the atoms. The magnitude of the slip vector and the centrosymmetry parameter at the stacking fault are measured to be  $\sim 1.35\text{\AA}$  and  $\sim 0.042$  (after making the parameter dimensionless [72]), respectively, which confirms that these dislocations are the Shockley partial dislocations of Copper. The Burgers vector of all the partials along and across the TBs are found to be of the  $1/6\langle 112 \rangle\{111\}$  type. The observation of an extended

partial dislocation along the TB in Cu is in agreement with the work by Van Swygenhoven *et al.* [34], and Cao and Wei [48]. Van Swygenhoven *et al.* [34] have explained this mechanism in terms of the ratio of the intrinsic stacking fault energy to the unstable stacking fault energy of the materials,  $\gamma_{SF}/\gamma_{USF}$ , by arguing that much larger values of this ratio indicate a lower energy barrier that has to be overcome to create a trailing partial dislocation. For Cu, this ratio is quite small (0.11 as listed in Table 4.1) consistent with the higher number of extended partial dislocations observed in the samples along the TB. At later deformation stages, we also observe that the trailing Shockley partial dislocation nucleates and follows the leading partial dislocation; this makes full dislocations both along and across the TB plane (see for example Figure 4.5(d)). However, the emission of trailing partials is found to be a very rare occurrence, and is mostly observed along the TBs, and only across the TBs for the lower twin density models.

### 4.6.2 Twinning fault deformation

After a leading partial dislocation has been emitted, one of the two possible deformation alternatives is either the nucleation of a trailing partial on the same slip plane creating a full dislocation, or the nucleation of a new partial on the adjacent (111) plane resulting in an extrinsic stacking fault or a twinning fault. A slip vector plot in Figure 4.6(a) shows two intrinsic stacking faults formed by leading partial dislocations in two neighboring twin lamellae, and a slipped perfect crystal by emission of a trailing partial. In Figure 4.6(b), it is evident that the emission of a new partial dislocation on the neighboring slip plane of an existing intrinsic fault creates an extrinsic stacking fault or a twinning fault within the twin lamella. Successive emissions of partials on the adjacent slip planes widen the thickness of the twinning fault. The possibility of creating a trailing partial on the same slip plane or a new partial

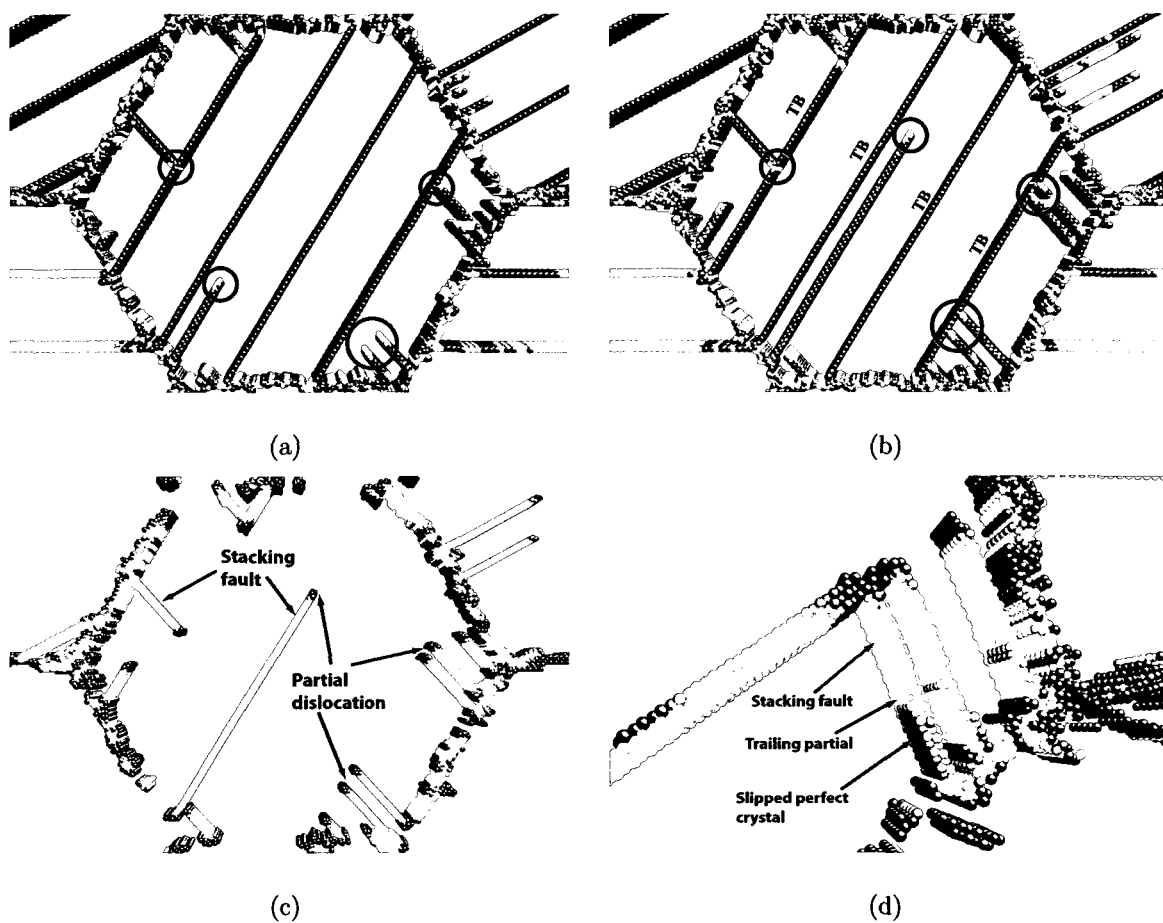
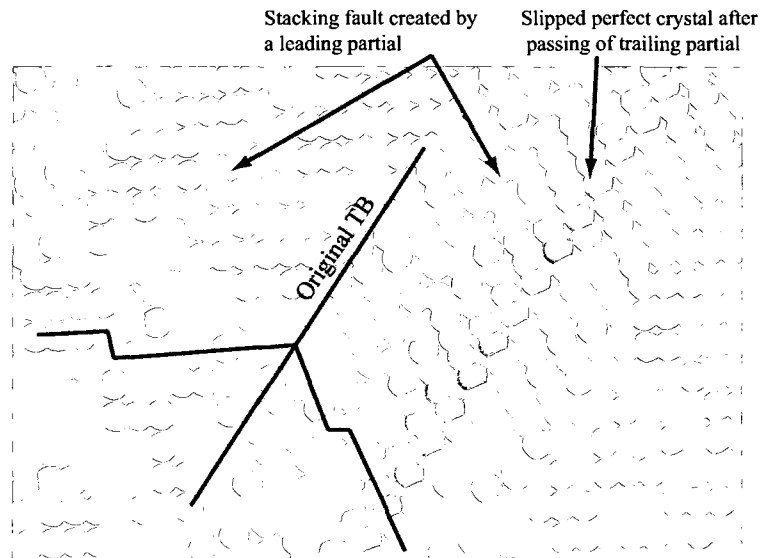


**Figure 4.5** (a, b) Centrosymmetry plots showing dislocation nucleation and propagation along and across the twin boundary, marked by the black circles, at (a) 36ps, and (b) 45ps. (c, d) Slip vector plots showing (c) the stacking fault at 45ps, and (d) emission of a trailing partial dislocation at 66ps.

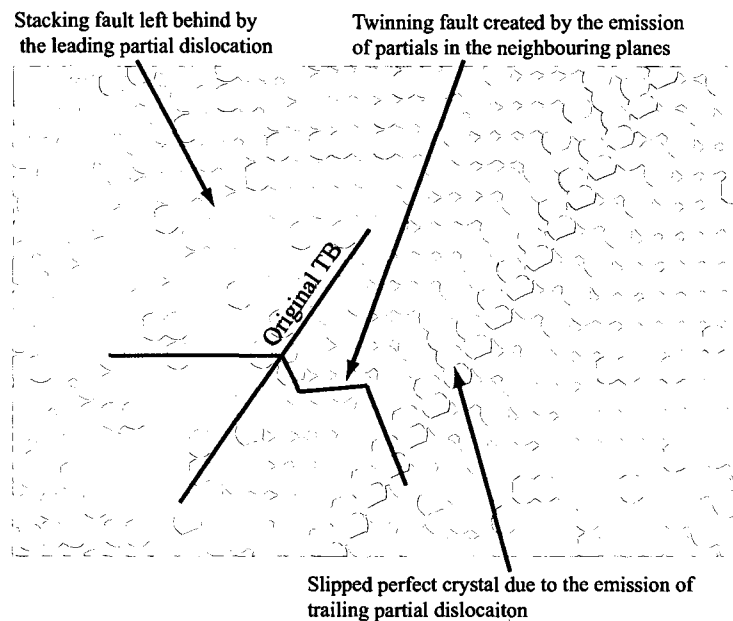
in the neighboring slip plane is controlled in part by the ratio  $\gamma_{UTF}/\gamma_{USF}$  [46]. For the Cu potential used in our simulation, these two energy densities are almost equal. Therefore, slip via the emission of a partial dislocation on the slip plane adjacent to the existing intrinsic stacking fault is equally possible as the slip via full dislocation on the same slip plane.

### 4.6.3 Twin boundary migration and change in twin width

Another important mechanism that has been observed in our simulations is twin boundary migration. During the deformation process, some of the TBs start to migrate to the neighboring (111) planes. This migration process is attributed to partial dislocations emitted from the GBs either on the adjacent (111) plane of the TB (as shown in Figure 4.7(a)), or at the same plane of the TB (as shown in Figure 4.7(b)). In every instance, the migration process starts from the GBs and ends on the other side of the grain, shifting the entire TB into the neighboring (111) plane, as shown in Figure 4.7(c). Such a deformation mechanism has also been observed by Froseth *et al.* [46] in nc-Al. Emission of several leading partials on the successive adjacent planes of a TB causes TB migration several atomic layers away from the original TB position, as shown in Figure 4.7(d). Also revealed in our work is that successive emissions of partial dislocations cause gradual reduction of the actual twin width inside the grain, as shown in Figure 4.7(e). The reduction of the twin width occurs for the same lamella where the emission of the partials actually takes place. Of course, on the other side of the TB, the neighboring lamella widens by one atomic plane for a single partial emission (as shown in (c)), and several atomic planes for successive emissions of partials on the neighboring planes (as shown in (d)). The possible deformation via twin boundary migration over other competing mechanisms (e.g., partial/full dislocation or twinning) is controlled by the magnitude



(a)



(b)

**Figure 4.6** (a) Intrinsic stacking fault created by the leading partials, and slipped perfect crystal formed by the trailing partial dislocation, and (b) formation of a twinning fault via emission of a partial dislocation on the neighboring slip plane of an existing intrinsic stacking fault.

of the unstable twin boundary migration energy density,  $\gamma_{UTM}$ . As listed in Table 4.1, the value of  $\gamma_{UTM}$  is less than both  $\gamma_{USF}$  and  $\gamma_{UTF}$ , and the ratio of  $\gamma_{UTM}/\gamma_{USF}$  is close to unity (0.88). Therefore, deformation via twin boundary migration is found to be a dominant deformation mechanism as the extended partial dislocations in nanotwinned Cu.

#### 4.6.4 Pile-up and transmission of dislocations across the TBs

As the deformation progresses, dislocations start to pile-up against the TBs. The density of accumulated dislocations against the TBs is higher in the higher twin density models compared to the lower twin density models, as in the latter case there is more evidence of dislocations moving across the TBs, leaving stacking faults that are subsequently intersected by the dislocations moving along the TBs. Moreover, as the twin density increases the intersection points between the TBs with the GBs also increases. Hence, the possibility of triggering new dislocations in the neighboring grains also increases. Thus, the total number of nucleated dislocations is also found to be higher in the higher twin density models.

The propagation of blocked dislocations across the TBs depends on the number of piled-up dislocations behind the leading dislocation, and also on the magnitude of the external stress [17]. For the most part, we observe the accumulation of only leading dislocations along the length of the TBs (i.e., there is a stacking fault running all the way back to the original nucleation site of each dislocation). In a very few cases we observe the nucleation of a trailing partial dislocation. Moreover, as the twin thickness reduces, dislocation pile-ups behind the leading partials become less evident. Only in the lower twin density models do we observe the emission of trailing partials across the TBs. In any case, dislocation passing across the TBs are observed only at very high stress levels. Figure 4.8(a) shows a few dislocations piled-up at the

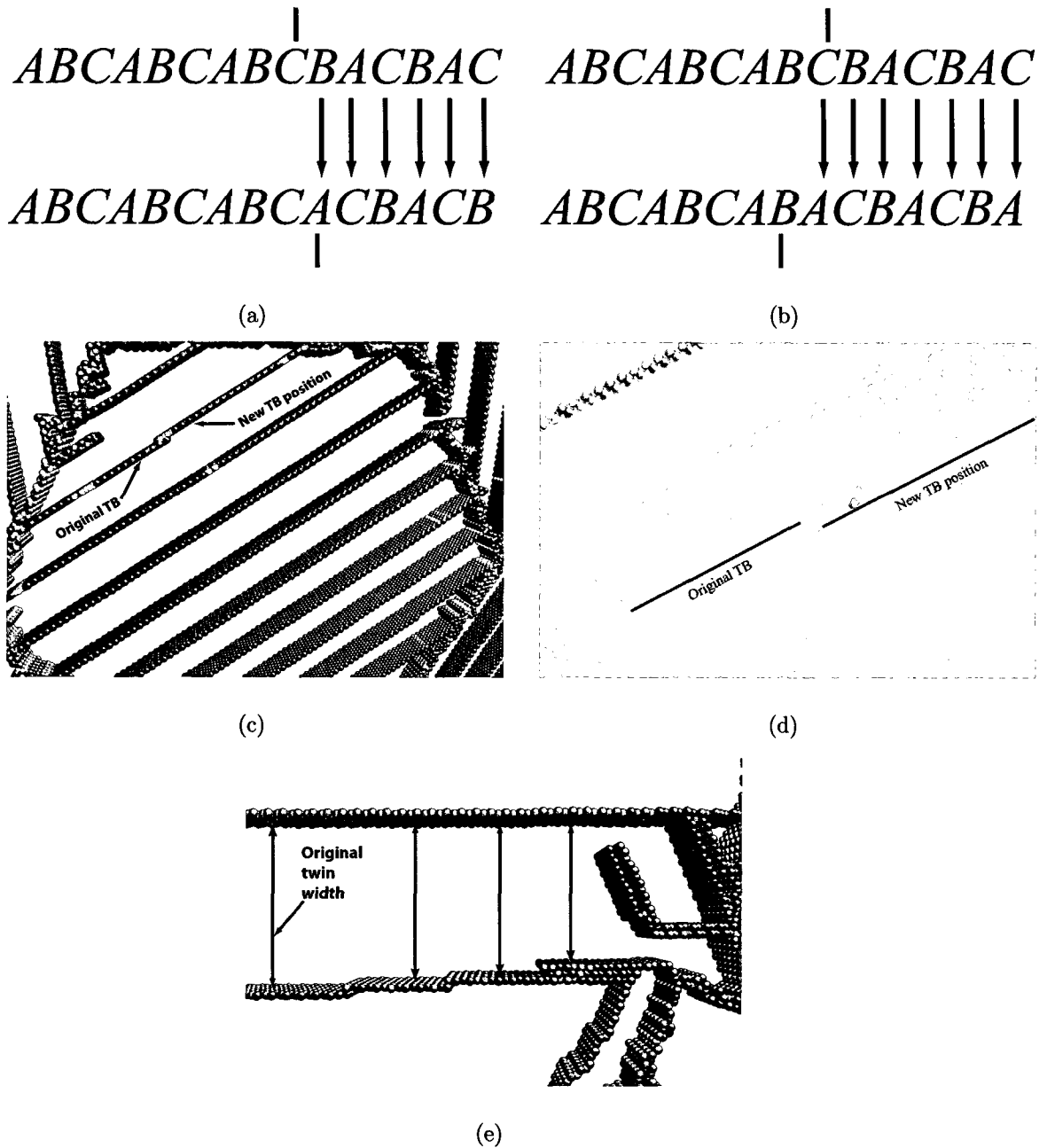


**Figure 4.7** (a, b) Twin boundary migration process by partial dislocation emission (a) on the adjacent (111) plane of the TB, and (b) at the same plane of the TB. (c, d) Twin boundary migration by (c) one atomic plane, and (d) several atomic planes. (e) Gradual reduction of the original width of the lamella where the nucleation of the partials occurs. It is also evident from both (c) and (d) that the reduction of the width is also accompanied by the widening of the lamella thickness on the other side of the twin boundary.

TBs, which later cross the boundary, as shown in Figure 4.8(b).

This passing mechanism can either be a single leading partial crossing the boundary, or a pile-up of many leading partials breaking the boundary together. For every twinned model, this mechanism is seen predominantly in grain 1 and 4 compared to the other two grains. It is also important to note that, in each grain, the partial dislocations start to cross the TBs at stress levels around the maximum RSS values of that grain, and vary between 1.1 – 1.4GPa in different grains of various models. Detailed discussion on the RSS values and the corresponding changes in the dominant deformation mode in each grain will be presented later in Section 4.8.

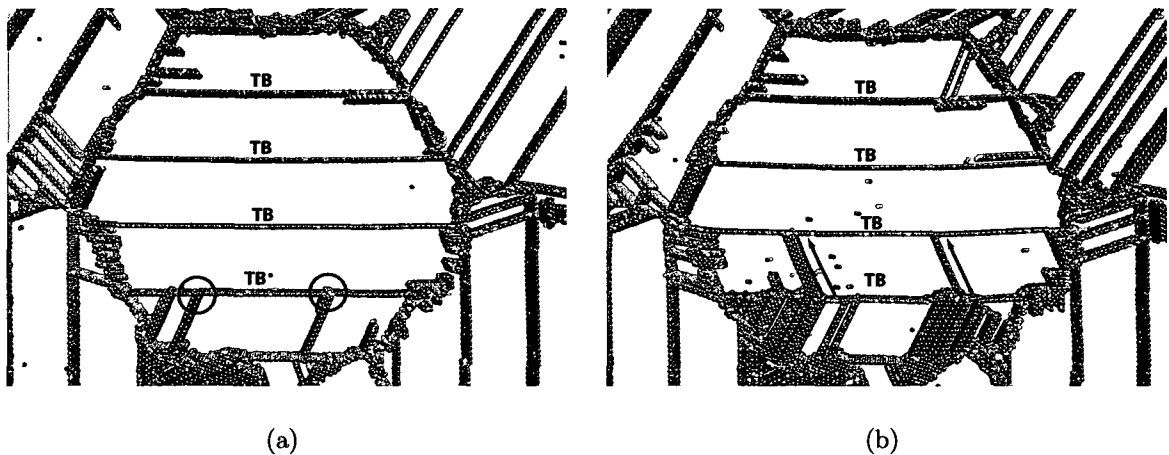


**Figure 4.8** (a) Accumulation of leading partial dislocations against the TB, (b) dislocation passing across the TB, either by a single leading partial dislocation or several dislocations together.

#### 4.6.5 Dislocation nucleation from steps

The partial dislocations leave behind a step on the TBs when crossing the boundaries. Figure 4.9(a) shows the formation of steps after three dislocations cross the TBs, marked by the black circles and arrows. Later, these steps become sources of

new dislocations, as shown in Figure 4.9(b). This observation agrees well with experimental observations by Konopka *et al.* [45] and Lu *et al.* [17]. However, we observed this mechanism only at 0K. It is possible that at elevated temperature, the thermal vibrations of the TB atoms are eliminating these steps at the TBs.

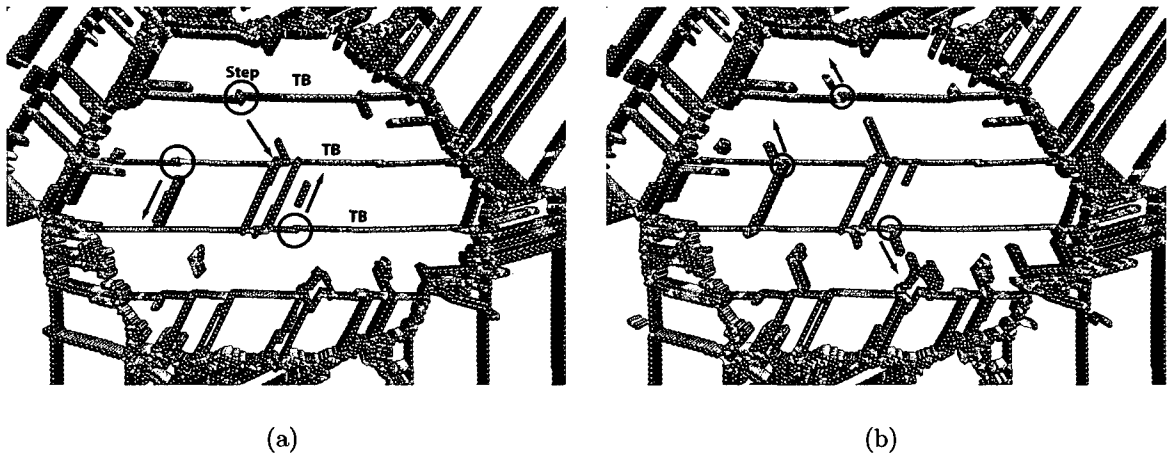


**Figure 4.9** (a) Step formation due to dislocation passing across the TBs, as shown by the black circles and arrows, and (b) new dislocation emission from these steps.

#### 4.6.6 Grain boundary sliding and grain rotation

Grain boundary sliding is quantified by computing the center of mass (COM) of each grain. The COM of a particular grain is easily computed as the average position of all atoms identified to be within that grain at the start of the simulation. The motion of the COM due to sliding (as opposed to the motion due to the applied strain) is found by subtracting the expected COM motion for purely uniform deformation of the sample. The relative displacement of the COM with respect to the reference position at each time step will help quantify the sliding of the GB between two neighboring grains. Figure 4.10 shows the time evolution of the COM of each grain, superimposed on the reference configuration of the grains for visualization. The grains

are not drawn in actual scale, but help to show their relative positions. It is evident from this figure that the displacements of the COMs of grains 1 and 2 are in opposite directions, which can be interpreted as GB sliding of about  $12\text{\AA}$  between grains 1-2 along the x-direction. Sliding also exists between grains 3-4, however, at a lower magnitude. Along the y-direction, the relative displacement of the COMs from the reference positions suggests considerable sliding at the GBs between grains 1-4, 2-3, and 2-4, but insignificant at the GB between grains 1-3.

Grain rotation is measured by monitoring the rotation of the TB planes inside the grains, and it appears to be insignificant for this model. After subtracting apparent rotation of the TB planes due to the stretching and compression of the sample, grains 2 and 3 exhibit small rotation over time ( $0.8 - 1.1^\circ$  in 120ps). However, the TBs inside the other two grains exhibit only slight bending, and no such rotation has been observed. It is possible that the periodic and highly symmetric nature of our simulation suppresses any significant grain rotations.

## 4.7 Stress calculation

LAMMPS simulations provide atomic stress tensors at the end of each time step. The commonly known Virial theorem is used to evaluate these stresses [59, 80–82]. For the EAM description of a material we write

$$\sigma_i^{IJ} = \frac{1}{\Omega_i} \left( \sum_{j \neq i}^N [\Phi'_{ij}(r_{ij}) + F'_i(\bar{\rho}_i)\rho'_j(r_{ij}) + F'_j(\bar{\rho}_j)\rho'_i(r_{ij})] \frac{r_{ij}^I r_{ij}^J}{r_{ij}} \right) - \frac{mv_i^I v_i^J}{\Omega_i}, \quad (4.3)$$

where the superscripts  $I$  and  $J$  refer to Cartesian components,  $\sigma_i^{IJ}$  refers to the stress tensor at atom  $i$ ,  $r_{ij}^I$  is the  $I^{\text{th}}$  component of the relative position vector between atoms  $i$  and  $j$ , and  $r_{ij}$  is its magnitude.  $m$  and  $v_i$  denote the atomic mass, and the velocity of atom  $i$ , respectively.  $\Omega_i$  is the atomic volume at site  $i$ .  $\Phi$ ,  $F$  and  $\rho$  are the

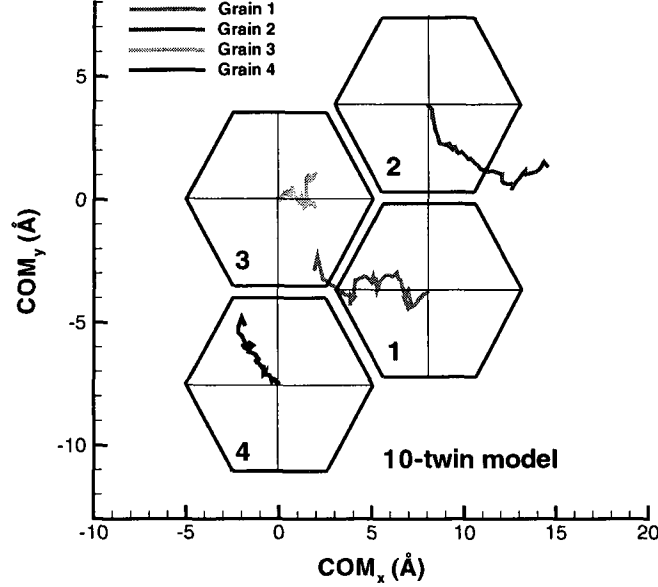


**Figure 4.10** Relative displacement of the center of mass (COM) with respect to the reference position over time. The intersection points of the horizontal and vertical lines represent the initial/reference COM positions. The grains are presented for visualization purpose only, and not drawn in appropriate scale.

pair potential, embedding energy, and electron density, respectively, while the prime components denote the differentiation of a function with respect to  $r_{ij}$ . The global stress tensor,  $\sigma^{IJ}$ , is obtained by summing up the atomic stress tensors of all the atoms at each time step and can be written as

$$\sigma^{IJ} = \frac{1}{\Omega} \sum_{i=1}^N \Omega_i \sigma_i^{IJ}, \quad (4.4)$$

where  $\Omega$  is the volume of the system and  $N$  is the total number of atoms. The stress tensor of each grain, which we call the “grain stress”, is evaluated by summing up the atomic stress tensors of the atoms in a particular grain as

$$\sigma_G^{IJ} = \frac{1}{\Omega_G} \sum_{i \in G} \Omega_i \sigma_i^{IJ}, \quad (4.5)$$

where  $G$  is the grain number,  $\Omega_G$  is the volume of the grain, and  $N_G$  is the number of atoms in that grain. These grain stress values are then resolved onto the two active slip planes in order to study how the RSS values are related to the deformation behaviors of the models. The following equation is used to resolve the grain stress tensor into various slip planes

$$\tau_{RSS}^{\alpha} = \sum_{I,J}^3 s_{\alpha}^I \sigma_G^{IJ} n_{\alpha}^I, \quad (4.6)$$

where  $\tau_{RSS}^{\alpha}$  is the resolved shear stress,  $\mathbf{s}_{\alpha}$  is the slip direction of slip system  $\alpha$ ,  $\sigma_G^{IJ}$  is the stress tensor of a particular grain, and  $\mathbf{n}_{\alpha}$  is the slip plane normal.

#### 4.7.1 Stress vs. strain response

The variations of the global von Mises stress with strain at a strain rate of  $4.0 \times 10^8 s^{-1}$  and temperature 300K are plotted in Figure 4.11(a). This figure illustrates that all of the models exhibit initial elastic behavior, reach a maximum stress, and then the stress values gradually decrease with increasing strain. The onset of plasticity is earlier in the nanotwinned models ( $\sim 0.02$  strain) compared to the twin-free model ( $\sim 0.033$  strain). In the early stages of plastic flow, the nanotwinned models exhibit higher stresses compared to the twin-free model. However, at later stages only the models with the highest twin densities (7- and 10-twin models) are significantly stronger than the twin-free model. The tensile stress-strain ( $\sigma_{xx}$  vs.  $\epsilon_{xx}$ ) behavior of the nanotwinned models has also been investigated, and the response of the models follows a similar trend (as shown in Figure 4.11(b)) as the von Mises stress-strain response shown in Figure 4.11(a).

The deformation behaviors of the nanotwinned models reveal that two of the four grains do not deform significantly due to the restriction imposed by the TBs on dislocation movement. As a result, dislocations start to accumulate against the

TBs, and the stress value gradually increases up to the maximum level. Due to the extremely thin lamellae width, the usual strengthening mechanism due to dislocation-dislocation interaction has not been observed at the lower strain stages. As the slip transfer becomes more evident across the TBs, the stress value begins to drop off with increasing strain. Figure 4.12(a) shows the deformation activities inside the grains of the 5-twin model before the stress value reaches the maximum point ( $\epsilon_{xx} = 0.065$ ). It is seen that some of the lamellae are populated with many dislocations, yet some remain dislocation-free. Dislocation accumulation and passing across the TB is only visible in the lower left corner grain where several dislocations have crossed the first TB, but are blocked at the second TB. The softening at the higher deformation stages is initiated from here, when a large number of dislocations begin to cross subsequent TBs, leading to a much faster decline of stress with strain. Figure 4.12(b) shows a large number of dislocation passing across the TBs in most of the grains at the larger strains,  $\epsilon_{xx} = 0.1$ . Ultimately, the dislocations break most of the TBs and the grains are completely deformed. Experimentally, nanocrystalline materials show softening due to plastic instability or concentration of large deformation in one region that results in a premature failure or necking in tension [39,40]. However, we found that rapid loss of strength of the nanotwinned samples is initiated as the TBs fail to resist deformation any further, and the slip transfer across the interface becomes much easier. This leads to complete failure of most of the TBs and the entire grain.

#### 4.7.2 Maximum stress variation with twin width

We take the maximum point of each curve of Figure 4.11(a), and plot those values against the inverse root of twin width ( $t$ ) for the different models, as shown in Figure 4.13(a). The Figure also shows the effect of temperature at a constant strain rate of  $4.0 \times 10^8 s^{-1}$ . At each temperature, the strength of the twin-free model is shown

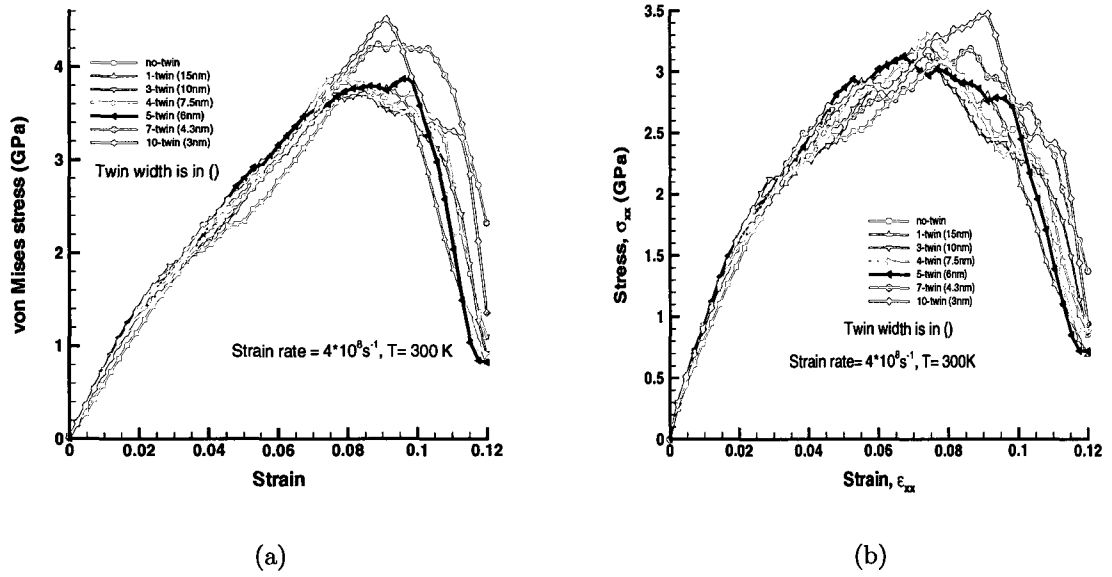


**Figure 4.11** Plots showing (a) von Mises stress vs. strain, and (b) tensile stress vs. strain response of various nanotwinned models at a strain rate of  $4.0 \times 10^8 \text{ s}^{-1}$ , and temperature 300K.

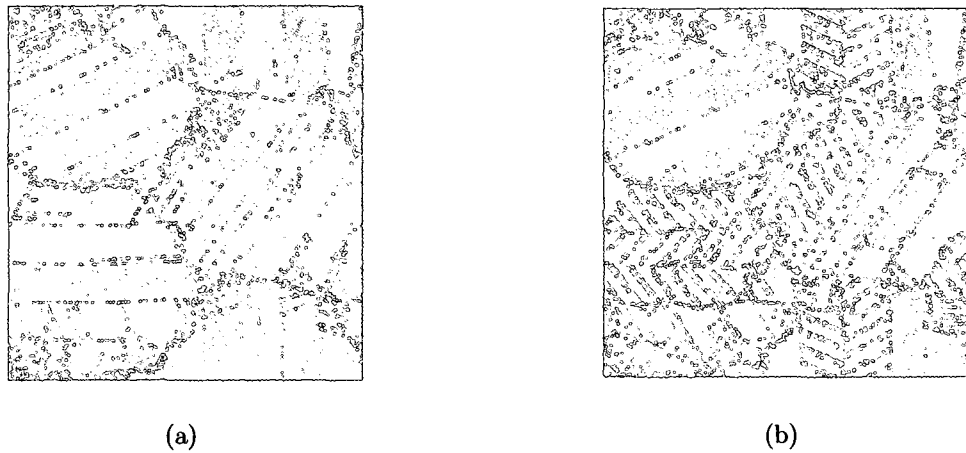


**Figure 4.12** Deformation mechanisms observed inside the grains at the (a) lower strains ( $\epsilon_{xx} = 0.065$ ), and (b) higher strains ( $\epsilon_{xx} = 0.1$ ) that leads to stress softening.

for reference (as shown by the circles in Figure 4.13(a)). At 0K, the trend shows that the twinned models have higher strengths compared to the twin-free model. The maximum stress values of these models vary between 5.5 – 6.3GPa, which yields an increase in strength of 4 – 18% by adding the nanotwins. It is important to note that although some strengthening has been achieved by adding the nanotwins inside the grains, increasing the twin density (or reducing the twin width) does not necessarily enhance the strength of the materials, as shown in Figure 4.13(a). Thus, there is virtually no effect of twin spacing at 0K. On the other hand, at a higher temperature (100K and 300K), the observation is quite different; a significant strengthening has been achieved by increasing the twin density. However, at a fixed twin width, the maximum von Mises stress value decreases with increasing temperature. Although some of the lower twin density models exhibit similar strength as the no-twin model, significant strengthening has been achieved for the higher twin density models (e.g., 7-twin and 10-twin models). The variation in strengths at 100K and 300K resemble the Hall-Petch behavior with the twin width ( $t^{-1/2}$ ), as shown in Figure 4.13(a). The maximum tensile strength of various models also exhibits a positive trend with twin width as shown in Figure 4.13(b), however, the main difference is that there is more scatter in the tensile stress result than in the von Mises result. We believe this is partly due to the fact that our loading is not purely uniaxial tension, but in fact a tensile strain along one direction combined with volume-conserving compressive strains in the other two directions. As such, we felt that the von Mises stress is a better scalar representation of the multi-axial stress state than the uniaxial stress.

This variation in strength of different models at a fixed temperature may be attributed to the uneven participation of various grains in the deformation processes; it depends upon grain orientation with respect to the loading direction, and also on the way the TBs and lamellae are participating in the deformation processes. It

is well established that the TBs, like the GBs, act as barriers to free dislocation movement, which leads to the strengthening of the materials [17–19, 41, 48]. Every model investigated in this research reveal that the movement of the dislocations that nucleate from the GBs and glide across the TBs are hindered by the TBs. Hence, the higher the number of the TBs (or the thinner the twin lamellae) the greater the resistance that the dislocations experience as they glide across the TBs. Moreover, the twin widths of most of the samples are so thin that only a single leading partial dislocation can be accommodated in the lamellae. In every instance, a number of leading partial dislocations have been found to gather along the length of the TBs (as shown in Figure 4.5(b)), rather than many dislocations piling up behind one another. With only a single dislocation in the pile-up, a higher external stress is required to break through the boundary compared to a pile-up of many dislocations [19]. On the other hand, glide dislocations moving along the TBs do not experience any obstacle until they reach the other side of the grain and are blocked by the GBs. This easy dislocation glide is mostly seen within the lamellae which are at the middle of the grains, and are considered to be the primary sources of plastic strain or ductility of the materials. One important point to mention here is that the usual strengthening mechanism by dislocation-dislocation interactions, observed in the coarse-grained materials, is not seen in our simulations, except for the thicker twin lamellae where a few dislocations moving in one slip plane have been found to intersect the stacking fault left behind by another dislocation. Therefore, the strengthening of the higher twin density models can be attributed solely to the dislocation-TB interactions.

As the dislocations gradually accumulate against the TBs, the stress level reaches a maximum point. At this stage the accumulated dislocations start to cross the TBs, and the curves gradually drop down. This event is more evident in the lower

twin density models (e.g., the 1-twin model). As mentioned before, the thickness of the twin lamellae of the higher twin density models is so small that only the leading partials are able to accumulate against the TBs along its length. Hence, no pile-up of dislocations behind the leading partials is observed. However, as the twin width increases, the formation of trailing partials becomes more evident. This increases the possibility of dislocation crossing across the TBs in the lower twin density models. After crossing the TBs the dislocations also experience fewer obstacles in their path, which makes deformation comparatively easier in these models. Therefore, the overall responses of the twinned models depend on how these TBs and lamellae are participating in the deformation processes. We conclude that there are several dominant factors contributing to the overall responses of these models: at the initial stages, strengthening is achieved as the TBs restrict dislocation movement, however, the easy glide of dislocations *along* the TBs contributes primarily to the material's ductility. At later stages, softening can also arise due to increased crossing of the TBs by dislocations.

## 4.8 Resolved Shear Stress (RSS) Calculation

As mentioned earlier in Section 4.7, due to the columnar structure of the grains there will be only two active slip systems in each grain that will be of our interest; one along the TBs and the other across the TBs. Therefore, we resolve the grain stresses,  $\sigma_G^{IJ}$ , onto these two slip planes according to Equation 4.6, and examine the variation of RSS with strain. These RSS vs. strain plots provide qualitative information of the dominant deformation mode in each grain.

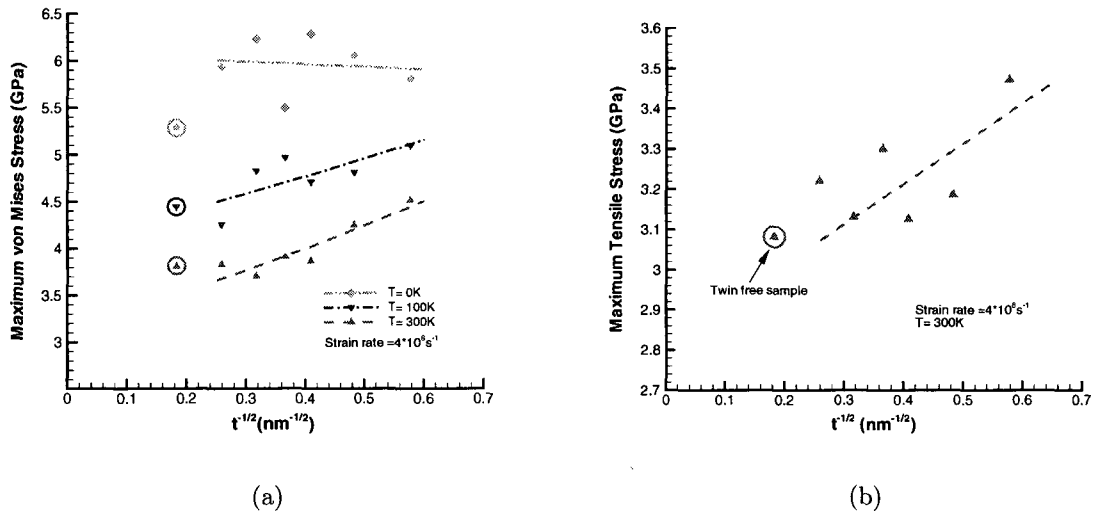


**Figure 4.13** (a) Variation of the maximum von Mises stress with inverse root of twin width ( $t$ ) at three different temperatures and a strain rate of  $4.0 \times 10^8 \text{ s}^{-1}$ . The maximum stress values for the twin-free models are marked by the circles, and plotted against the grain size  $d$  (30nm), instead of  $t$ . The rest of the data points are for various twinned models of grain size 30nm, and plotted against the twin width,  $t$ . (b) Variation of maximum tensile stress with inverse root of twin width ( $t$ ) at a strain rate of  $4.0 \times 10^8 \text{ s}^{-1}$  and 300K.

### 4.8.1 Resolved shear stress (RSS) variations in various grains.

Although there are only two active slip planes in each grain, there exist significant differences in the deformation behaviors of various grains due to their orientations with respect to the loading axis. Our goal here is to explore how the rotation of the grains affects the relative participation of each grain in the overall deformation processes of the model. Figures 4.14(a) and (b) present the variations of RSS of each grain of the 5-twin model along and across the TBs, respectively. Along the TBs, as shown in Figure 4.14(a), grains 2 and 3 are experiencing the maximum stress, while the stresses acting along the TBs of the other two grains are negligible. Across the TBs, as shown in Figure 4.14(b), grains 1, 2, and 4 are experiencing much higher resolved stresses than grain 3. This variations of the RSS values in different grains ultimately dictate the deformation behaviors in each grain. Hence, grains 1 and 4 exhibit dominant deformation across the TBs, while in grain 3 deformation is predominantly along the TBs. However, the deformation behavior of grain 2 is comparable in both of the active slip planes. Based on the above discussion, it can be said that the elevated *strength* of the nanotwinned models are attributed to the deformation behaviors in grains 1, 2, and 4, while grains 2 and 3 are contributing primarily to the *ductility* of the materials.

Any deviations or fluctuations in each RSS vs. strain graph are also indicative of some key deformation activities occurring inside that grain at those moments. We present two examples, as shown in Figure 4.15 and 4.16, in which the key points, marked as (i-v), correlate with the various deformation mechanisms occurring inside grains 3 and 1, respectively, of the 5-twin model. The same notation (i-v) is also used for the deformation snap shots (slip vector plots) presented below. In Figure 4.15, points ‘i’ and ‘ii’ depict the nucleation and glide of the leading partials along the TBs that left intrinsic stacking faults behind, point ‘iii’ shows the nucleation of a trailing

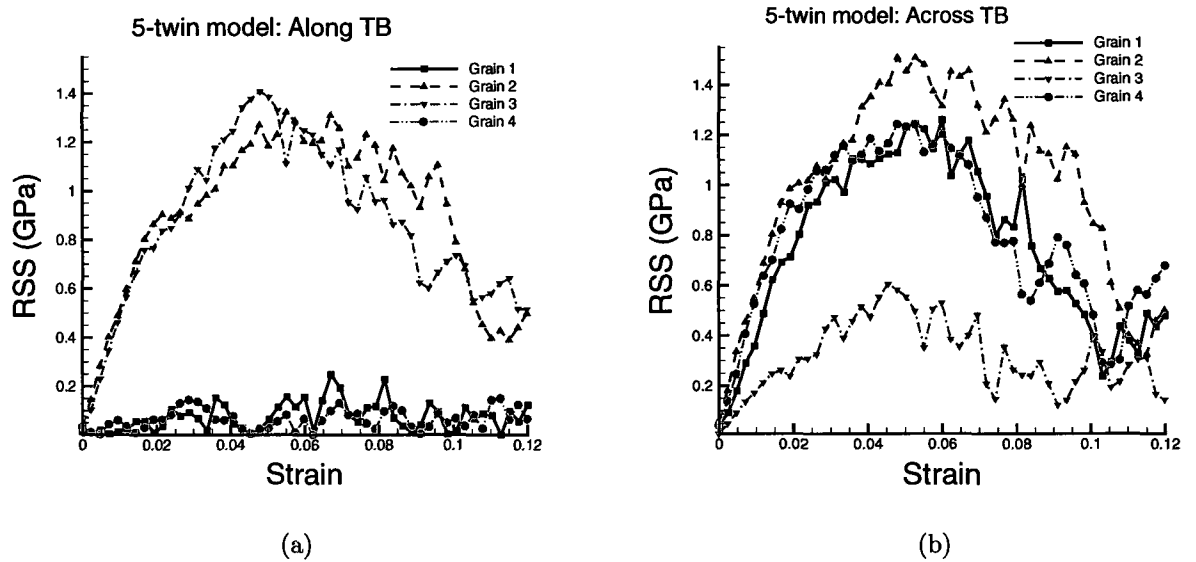


**Figure 4.14** Resolved shear stress variation with strain (a) along, and (b) across the TBs for different grains of the 5-twin model.

partial dislocation along the TB, and points 'iv' and 'v' display the glide of few more dislocations at later deformation stages, with extrinsic stacking faults behind. In Figure 4.16, points 'i' and 'ii' depict the nucleation and gradual accumulation of the leading partial dislocations against the TBs, point 'iii' and 'iv' show gradual passing of the dislocations across the first TB, and finally point 'v' shows the dislocations have started to cross the second TB. These points in the RSS vs. strain plots also provide quantitative information regarding the stress requirements for the occurrence of these deformation processes inside the Cu nanotwinned structures.

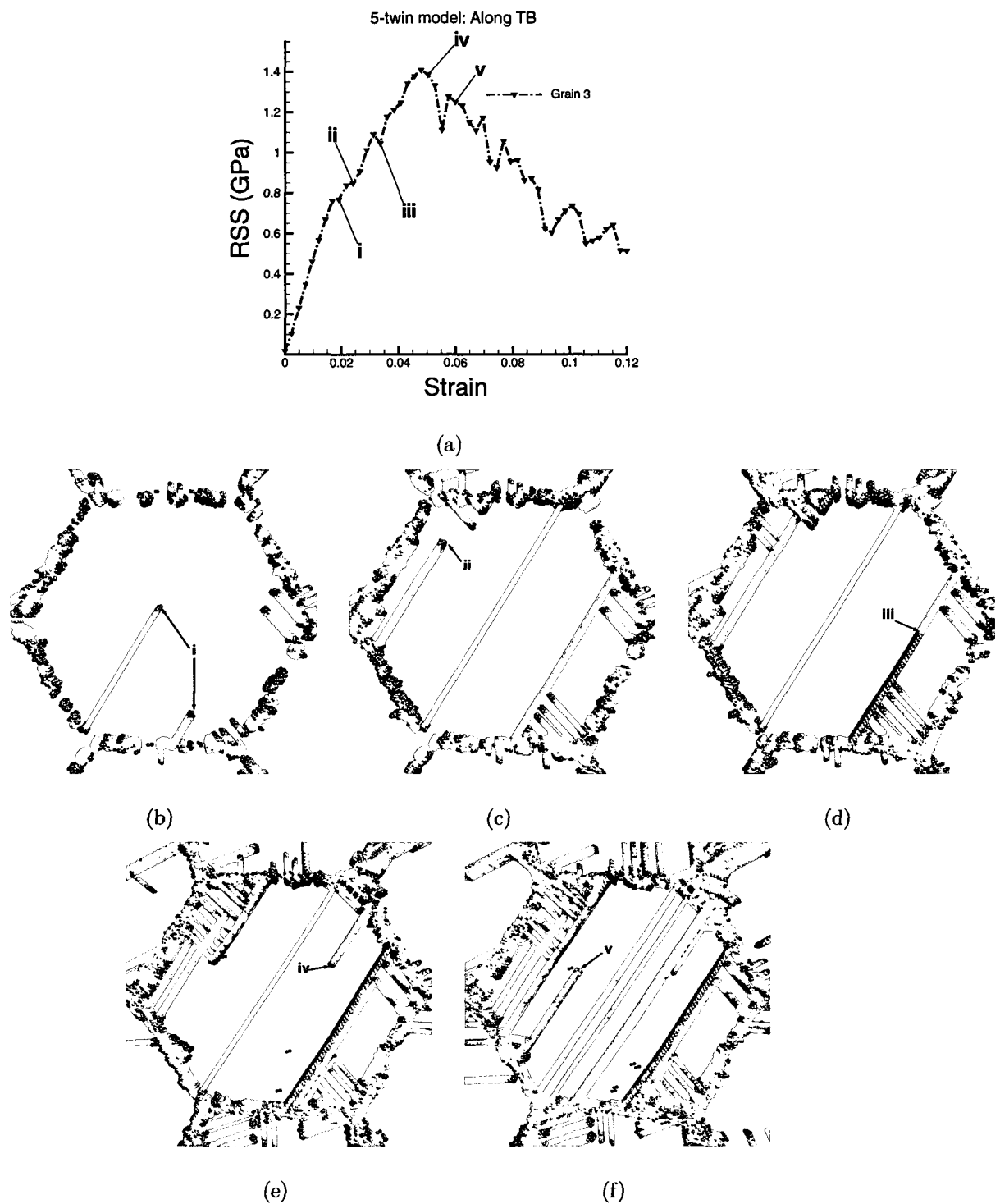


**Figure 4.15** (a) Resolves shear stress vs. strain along the TBs of grain 3 of the 5-twin model. The key points (i-v) marked in (a) correspond to the deformation behaviors shown in (b-f).

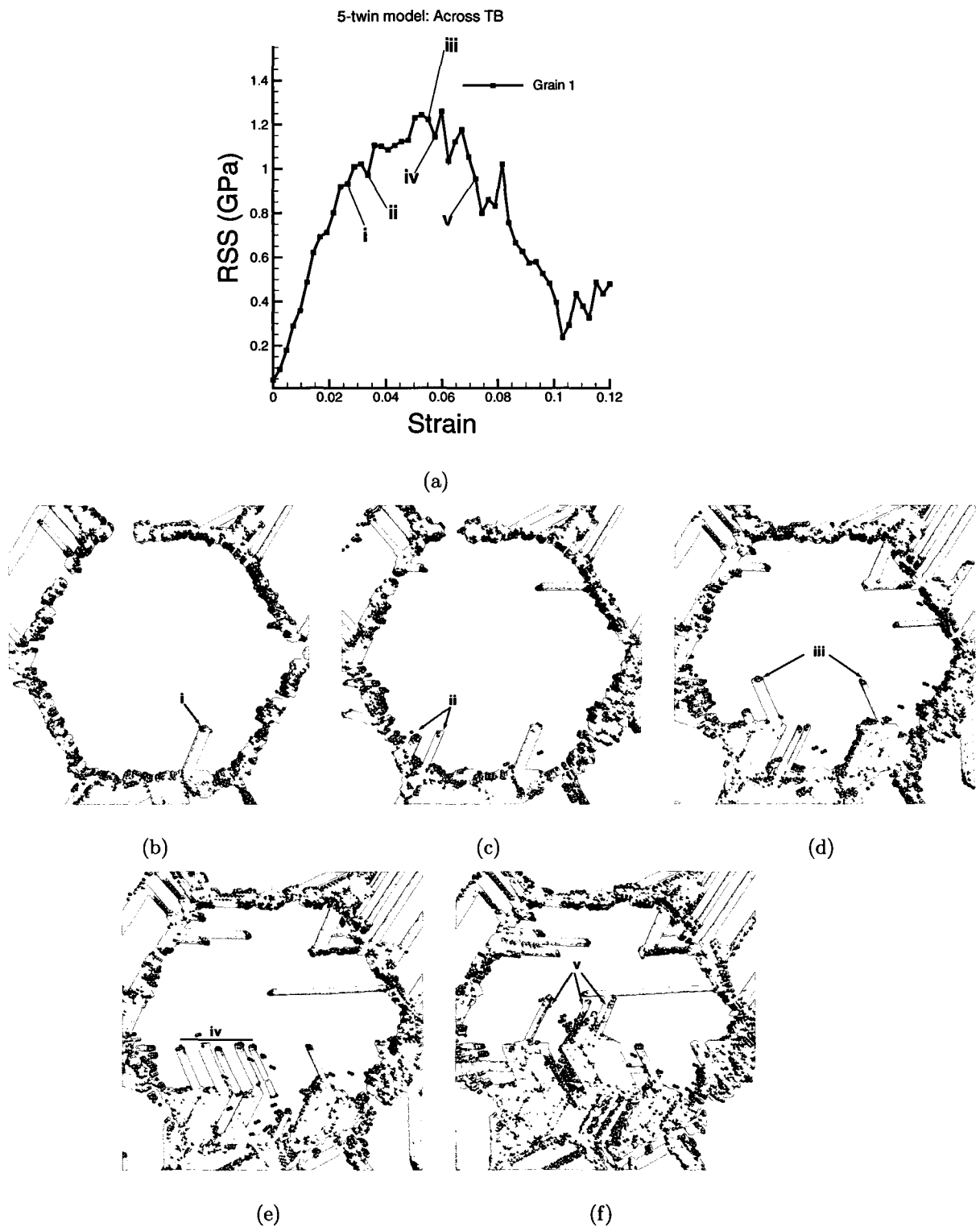


**Figure 4.16** (a) Resolves shear stress vs. strain across the TBs of grain 1 of the 5-twin model. The key points (i-v) marked in (a) correspond to the deformation behaviors shown in (b-f).

## Chapter 5

# Effects of twin width, grain size, and temperature on toughness

In the last chapter we discussed about the deformation behavior and stress-strain response of nanotwinned copper. Also the maximum strength exhibited by various models were analyzed, and the effect of twin width were tested. The focus of this chapter is to examine materials toughness of the nanotwinned copper. The effect of twin width, grain size and temperature will also be analyzed. We will also examine both grain size and twin refinement, and try to evaluate how to refine both these to parameters to optimize the strength and toughness.

We focus primarily on ‘toughness’ because we hope to understand the unique behavior of nanotwinned samples exhibiting both enhanced strength and ductility with decreasing twin width. Due to the nature of the loading of the simulation (tensile strain along one direction combined with volume-conserving compressive strains in the other two directions), it is not feasible to explicitly measure the uniaxial yield strength and ductility of the samples. At the same time, this controlled loading will not lead to the abrupt, catastrophic failure of a purely uniaxial test. We select an alternate

measure (toughness) to quantify the effects of adding nanotwins on both strength and ductility of the samples. We feel that the calculated toughness can therefore be a better measure of the multi-axial stress state. We also want to emphasize that in the property comparison we have used both the maximum von Mises stress and the toughness of various nanotwinned samples.

## 5.1 Toughness measurement

Nanotwinned material's toughness (T) is calculated by summing up the areas under the global normal stress vs. strain curves of all three directions of each model using the following expression

$$T = \int_0^{\epsilon_{x\max}} \sigma_x d\epsilon_x + \int_0^{\epsilon_{y\max}} \sigma_y d\epsilon_y + \int_0^{\epsilon_{z\max}} \sigma_z d\epsilon_z, \quad (5.1)$$

where  $\sigma_x, \sigma_y, \sigma_z$  denote the global normal stresses, and  $\epsilon_x, \epsilon_y, \epsilon_z$  denote the normal strains along the x, y, and z directions, respectively. For an example, the first term on the right hand side of Equation 5.1,  $T_x$ , is shown in Figure 5.1(a). Note that since the simulations are under approximately uniaxial conditions,  $T_x$  dominates  $T_y$  and  $T_z$ . Figure 5.1(b) depicts the effects of length scale on the toughness of nanotwinned models at three different temperatures (0K, 100K, and 300K) and at a strain rate of  $4.0 \times 10^8 s^{-1}$ . The toughness values are plotted against the inverse root of twin width (t), as shown in Figure 5.1(b). From this plot several important observations can be made- (i) at any temperature, the twinned models exhibit higher toughness than the twin-free model, (ii) the toughness increases with decreasing twin width, and (iii) the toughness of the nanotwinned models increases with decreasing temperature. These observations are in good agreement with the simulation results obtained by [46, 48] and the experimental observations by [18, 19, 41]. In the next few sections we will

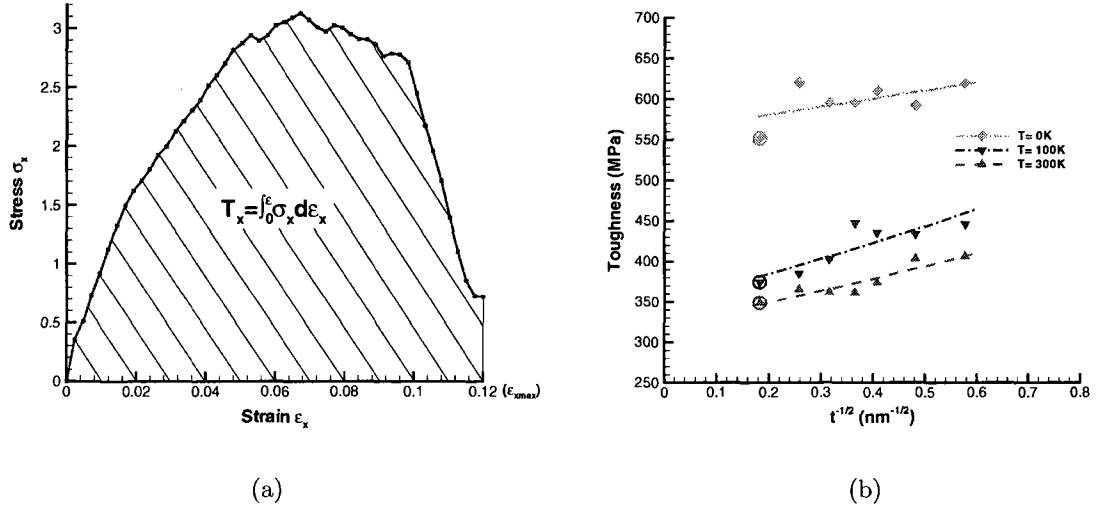


**Figure 5.1** (a) The area under the global normal stress and strain curve along the x-direction, representing toughness along this direction, and (b) toughness variation with inverse root of twin width ( $t$ ) at three different temperatures and a strain rate of  $4.0 \times 10^8 s^{-1}$ . Toughness values of the twin-free models are marked with circles, and plotted against the grain size  $d$  (30nm), instead of  $t$ . The rest of the data points are for various twinned models of grain size 30nm, and plotted against the twin width,  $t$ .

present some key atomistic deformation mechanisms that are contributing to these observed behaviors.

## 5.2 Effects of Twin Width

To understand the above behavior, let us revisit our grain orientations and corresponding deformation pattern in each grain. Due to the columnar structure of the model, all dislocation lines are parallel to the  $\langle 110 \rangle$  columnar axis ( $z$ -direction), and following their nucleation dislocations can glide only on either of the two active  $\{111\}$  slip systems in each grain. Therefore, deformation in each grain can be either ‘along the TBs’ (along the  $(111)$  slip planes), or ‘across the TBs’ (along the  $(11\bar{1})$  slip planes),

or both. In grains 1 and 4, the TBs ((111) planes) are aligned along  $0^\circ$  and  $90^\circ$  from the loading axis, respectively, and represent the lowest Schmid factor planes. On the other hand, the  $(11\bar{1})$  planes represent the highest Schmid factor planes. Therefore, deformation is found to be dominant across the TBs. The opposite is true for grain 3. Due to the orientation ( $60^\circ$  from the loading axis), the higher Schmid factor planes are the TB planes, and hence, deformation along the TBs is found to be dominant in this grain. The deformation mode of grain 2 is in-between; deformation along and across the TBs are comparable.

Considering the fact that strengthening arise from obstacles to free dislocation movement imposed by the TBs [17–19, 41, 48], strengthening can be attributed to the deformation behaviors of grains 1, 4, and partially of grain 2. The higher twin density imposes higher resistance on the glide dislocation movement across the TBs, and therefore, strengthen the material. Let us now investigate what grain 3 is contributing to the overall deformation processes. As mentioned before, deformation along the TBs is more prevalent than deformation across the TB planes in grain 3, due to its orientation. After nucleation, dislocations moving along the TBs do not experience any obstacle until they reach the other side of the grain and are blocked by the GBs. Therefore, these free dislocations along the TBs are the major carriers of the plastic strain contributing to the material's ductility. Grain 2 is also partially responsible in this regard. Similar to the dislocation movements across the TBs, dislocation movements along the TBs are also affected by the TB density. After comparing the relative amount of dislocations in the various models, the higher twin density model (i.e., 3nm twin width) is found to have more dislocations moving along the TBs, as shown in Figure 5.2. This is probably because the higher number of TBs creates more TB/GB junctions (or dislocation sources), thereby facilitating dislocation nucleation into the grains.

To investigate further, the resolved shear stress at which the first slip occurs (or the critical resolved shear stress-CRSS), is evaluated both along and across the TB planes of each grain. Figure 5.3(a) depicts the resolved shear stress variation with strain along the TB in grain 3 of a nanotwinned model, where the deviation in the curve marked by the arrow indicates the emission of the first leading partial dislocation or the CRSS along the TB of this grain. The CRSS along the TBs in grains 2 and 3 are compared for different nanotwinned models, and shown in Figure 5.3(b). It is evident from this figure that the CRSS value decreases with decreasing twin width, which means that the higher density of TBs facilitate the deformation process along the TBs. Therefore, the enhanced toughness exhibited by the higher twin density models can be attributed to the hardening effects imposed by the higher density of the twins in some grains, and simultaneously, easy glide of dislocations along the TBs in other grains. The CRSS of various grains with certain twin width is expected to be independent of the grain orientation. However, in most of the cases in Figure 5.3(b) we notice a significant difference in the CRSS between grains 2 and 3. This discrepancy arises due to the dominant deformation mechanism that initiate the slip; deformation via either emission of extended partial dislocations along the TBs or TBM. Recently, Zhu *et al.* [20] attribute TB mediated slip transfer (TB acts as a sink or source of dislocations), and gradual loss of coherency of TBs with deformation for the relatively high ductility of nanotwinned materials. Here we propose another mechanism of improved toughness: the nanotwinned sample acts like a “composite” material. When loaded in a certain direction, grains that are favorably oriented to allow dislocation motion “along” the TBs act as the “ductile phase”, while the other grains allowing dislocation motion “across” the TBs act as the “strengthening phase”. Therefore, a random polycrystalline nanotwinned sample gains toughness through this ‘bi-modal’ deformation behavior (both along and across the TBs) of

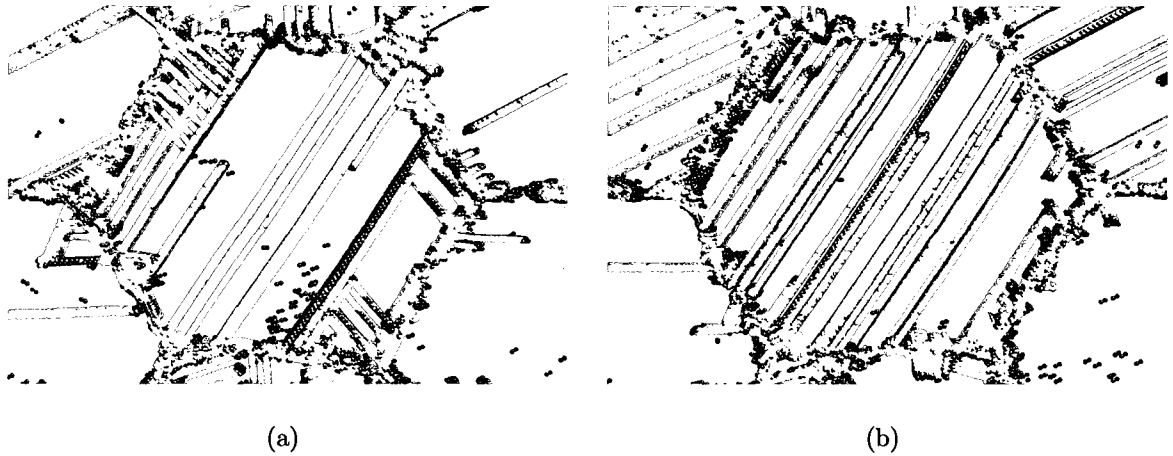


**Figure 5.2** Slip vector plot showing relative amount of dislocations at 300K in grain 3 of a nanotwinned structure with (a) 6nm, and (b) 3nm twin spacings. Dislocation movements along the TBs ( $60^\circ$  from the horizontal) are mostly visible for the higher twin density model.

variously oriented grains.

### 5.3 Grain size and twin width refinement

It has always been a challenge for the researchers to find the size limit below which the properties of materials can no longer be improved. As discussed before, nc materials exhibit elevated strength and reduced ductility with grain size refinement. On the other hand, nanotwinned structures exhibit increase in both strength and ductility with twin width refinement. To obtain a clearer picture about the effects of grain size and twin width refinements, we investigate several nanotwinned models with a larger grain size (60nm). The orientation of the grains are the same as we have reported earlier in Section 4.1 for the 30nm model, as shown in Figure 4.1, but the twin spacing is varied between 3nm to 12nm. The periodic simulation box dimensions along the x- and y-directions are  $100\text{nm} \times 120\text{nm}$ , and contains approximately 1.6 million atoms. For comparison with the smaller grain size model (30nm), the strain

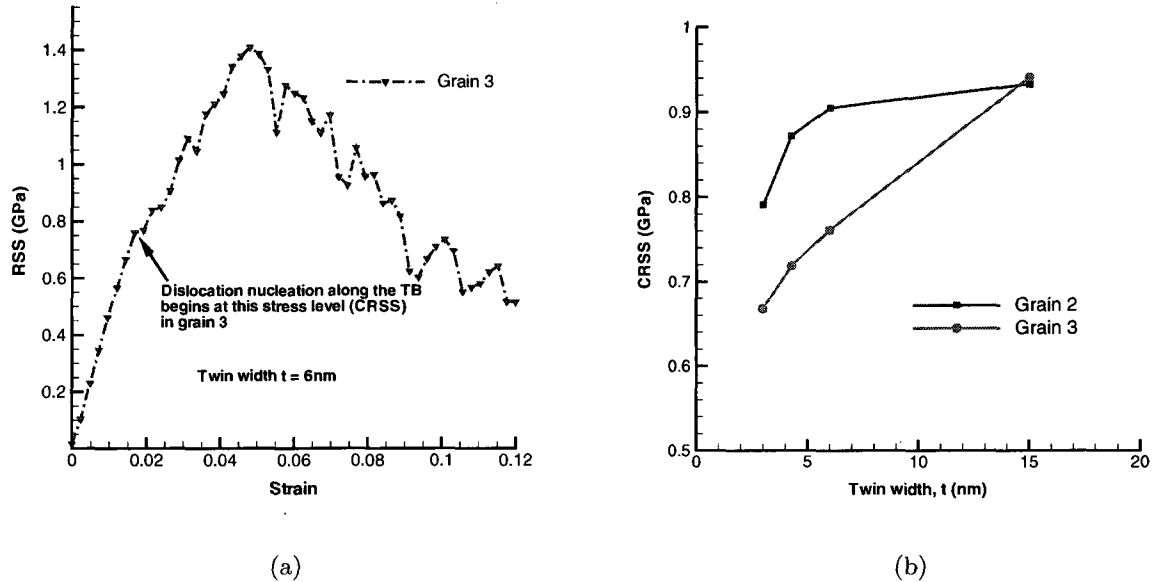


**Figure 5.3** (a) Resolved shear stress variation with strain along the TB in grain 3 of 6nm twin width model. The deviation in the curve marked by the arrow denotes the emission of the first leading partial dislocation or the CRSS along the TB of this grain. (b) Variation of critical resolved shear stress (CRSS) with twin width. It is evident that CRSS decreases with twin width.

rate and temperature are set fixed at  $4.0 \times 10^8 s^{-1}$  and 300K, respectively. Two different grain size models with various twin spacings will allow us to examine the effects of three different types of refinements (as illustrated in Figure 5.4) on the properties of nanotwinned structure. In the first refinement (from  $A$  to  $A'$ ), the grain size ( $d$ ) is held constant while the twin width ( $t$ ) is reduced by half. In the second refinement (from  $A$  to  $B$ ), the grain size has been reduced by half, while keeping the twin width constant. Lastly, in the third refinement (from  $A$  to  $B'$ ), both the grain size and twin width have been refined by half. The two plots shown in Figure 5.5 depict the strength and toughness variations with inverse root of twin spacing ( $t$ ) for two different grain size models. For simplicity, we selected four data points (joined

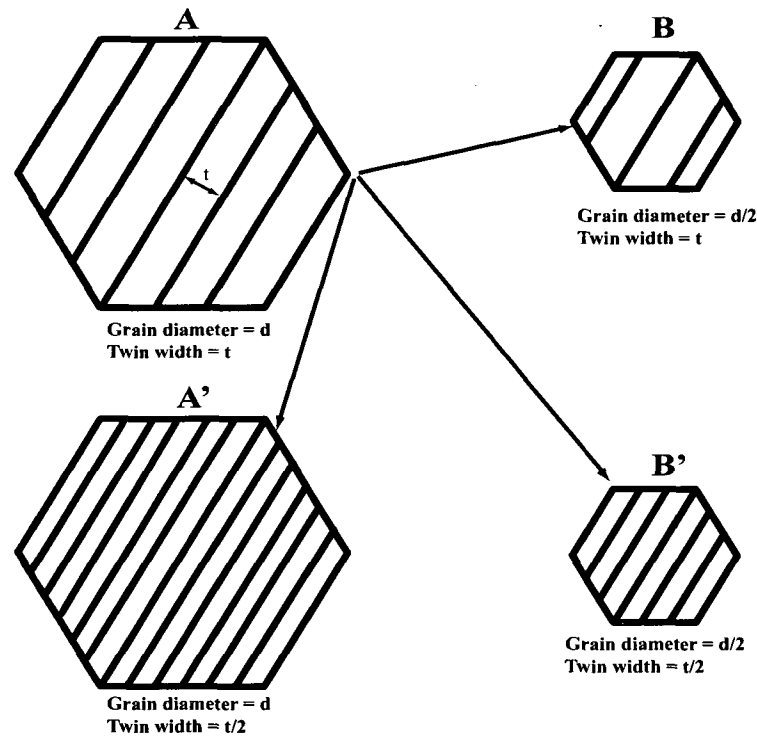


**Figure 5.4** Schematic diagram showing three types of refinements considered for property comparison.  $A$  is the reference configuration, while  $A'$ ,  $B$ , and  $B'$  are the configurations obtained from three different types of refinements.

by three different line types) to demonstrate the effects of various refinements on the properties of nanotwinned materials. Figure 5.5(a) shows that all three refinements yield enhanced strength of various magnitudes. It is apparent that the most significant enhancement is achieved by the  $A$  to  $B'$  refinement. However, this enhancement can be attributed to the simultaneous effects of two refinements,  $A$  to  $A'$  and  $A'$  to  $B'$ , inside the grain. Comparing the other two refinements, the twin refinement ( $A$  to  $A'$ ) is found to cause better enhancement in strength than the grain refinement ( $A$  to  $B$ ). Figure 5.5(b) shows that the toughness values are higher for the bigger grain models (reduces 2 – 5% as the grain size is reduced or due to the  $A$  to  $B$  refinement). As discussed earlier, the toughness of the nanotwinned materials can be attributed

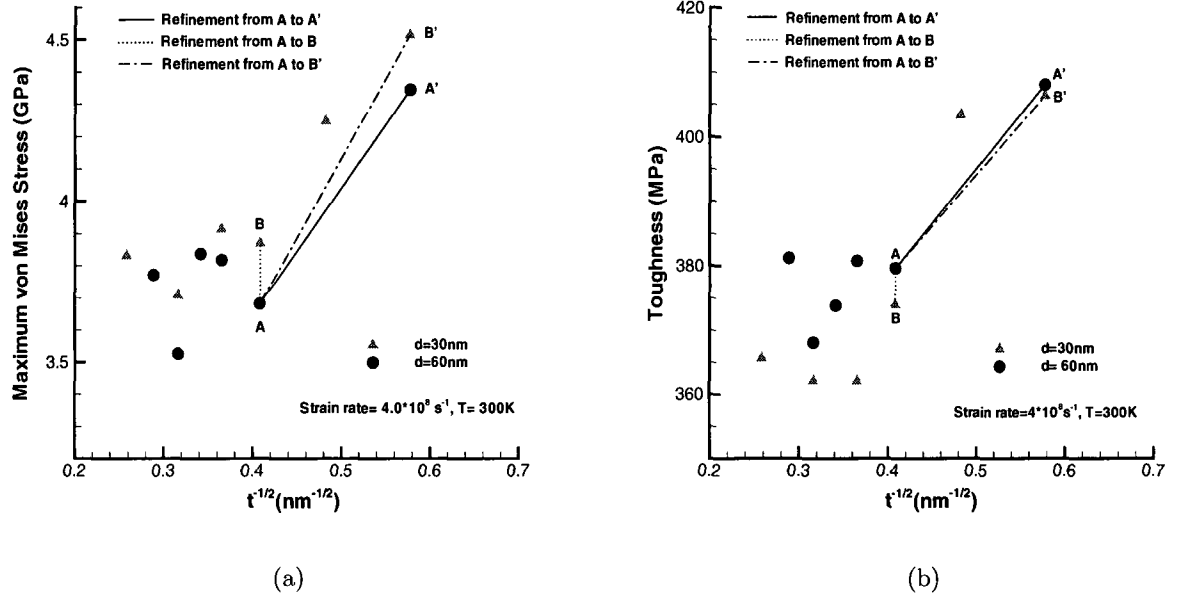


**Figure 5.5** Strength and toughness comparison between two different grain size models. The four data points joined by three different line types demonstrate the effects of three types of refinements, described in Figure 5.4, on the properties of nanotwinned Cu.

to free dislocation movement along the TBs in each grain. Therefore, the larger grain models ensure longer free paths, and hence, exhibit higher toughness. On the other hand, simultaneous refinement of the grain size and twin width by half ( $A$  to  $B'$  refinement) results in a 7 – 8% enhancement in toughness. Simultaneous refinement of both of these two sizes may not always yield better properties. For example, Figure 5.5(b) shows that simultaneous refinements of grain size (from 60 to 30nm) and twin width (from 6 to 3nm) yield similar toughness as achieved by refining only the twin width from 6 to 3nm inside the 60nm grains ( $A$  to  $A'$  refinement). Based on these observations it can be concluded that twin refinement (down to 3 – 4nm) always yields better properties, however, the choice of the grain size depends more on the optimization between strength and toughness. Our observations agree well

with the speculations made by Dao *et al.* regarding the optimization of strength and ductility versus grain size and twin spacing [18]. In addition to this, we want to emphasize that the grain orientations should also be taken into consideration to optimize nanotwinned materials' properties. The macroscopic properties of materials depend on the microscopic deformation mechanisms in each grain, which in turn depend on the orientation of the grains with respect to the loading axis. Therefore, we speculate that the dominant deformation modes in each grain (either along or across the TBs) can be altered by controlling the grain orientations, which will ultimately help optimize the properties.

Lu *et al.* [83] investigate the yield strength of various nanotwinned copper samples of average twin thickness ranging from a few nanometers to about 100nm. They report an increase in yield strength with decreasing twin spacing down to 15nm, however, below that a softening is observed. They attribute this softening to the increased dislocation array associated with the GBs and pre-existing dislocation density at the TBs (TB steps), both of which can act as potential dislocation sources to facilitate macroscopic yielding. The resolved shear stress analysis of the grains, as shown in Figure 5.3(b), shows a similar microscopic response along the TBs, where yielding is facilitated with decreasing twin width due to the increased number of GB dislocation sources. However, the macroscopic strength (maximum von Mises stress) of the samples shows an opposite trend with decreasing twin width, as shown in Figure 5.5(a). The source of this discrepancy could be the number of pre-existing dislocation sources and the average grain size of the samples (30nm in the simulation vs. 400-600nm in the experiment). The atomistic samples of the same twin thickness (between 4-15nm) used in our study have lower number of GB dislocation sources, and are also free from any pre-existing dislocations at the TBs (or the TB steps). Therefore, the softening or macroscopic yielding with twin refinement due to easy dislocation motion from

the TB steps has not been seen in our cases. In other words, the TBs within our simulation models act more like dislocation barriers than dislocation sources. Moreover, at the smaller grain sizes, the grain boundary contribution to the macroscopic strengthening is more significant, and it is possible that this surpasses the apparent microscopic softening/yielding with twin refinement.

## 5.4 Effects of Temperature

As depicted in Figure 5.1(b), the nanotwinned materials exhibit elevated toughness with decreasing temperature for all twin spacings. After analyzing the deformation behaviors of the nanotwinned model with 3nm twin width, the following observations have been made at different temperatures. As temperature rises- (i) deformation in each grain begins earlier, (ii) a higher number of dislocations becomes more evident, (iii) dislocations start to cross the TBs earlier, (iv) the TB migration process becomes faster, and (v) full dislocations become more evident at the early deformation stages. Therefore as the temperature drops, various deformation processes are suppressed. Figure 5.6 presents some of the deformation processes, and compares the effects of temperature on those processes at 0K and 300K. It is important to note that, although, the simulation temperature is set at a fixed temperature, the actual temperature of the system does not remain constant during the simulation, rather it fluctuates around the set temperature. In each step, the thermostat measures the actual temperature of the system and tries to bring the system temperature back to the set value. Therefore, the average temperature of the system is slightly different than the set temperature, i.e., for a 0K simulation the average temperature is measured to be 0.18K. The idea behind discussing deformation behaviour at 0K is to present a qualitative comparison of the deformation rate at an extremely low temperature-

close to zero, and at room temperature. In Figure 5.6(a) we present a TB migration process at 0K, and compare the same process at 300K, as shown in Figure 5.6(b). It is evident from these snapshots that the TB migration process becomes faster at the higher temperature. Figure 5.6(c) and (d) are the snapshots taken at the same moment (at 132ps) in grain 1 at 0K and 300K, respectively. Some of the blocked dislocations start to cross the TB at 300K (shown in Figure 5.6(d)), whereas, no such activity is visible at 0K, as shown in Figure 5.6(c). Figure 5.6(e) and (f) compare the deformation states in grain 2 after 120ps. Relatively higher number of dislocations are visible at 300K along with an emission of a trailing partial dislocation.

Therefore, at room temperature, thermally assisted deformations become more active which possibly reduce the dislocation storage capacity, and ultimately affect the toughness of the nanotwinned structures. Ma *et al.* [41] and Wang *et al.* [39,40] discussed in detail the temperature dependence of the dislocation storage capacity, and the corresponding changes in nanostructured materials' properties. Our observations are in accordance to some extent with their experimental observations.

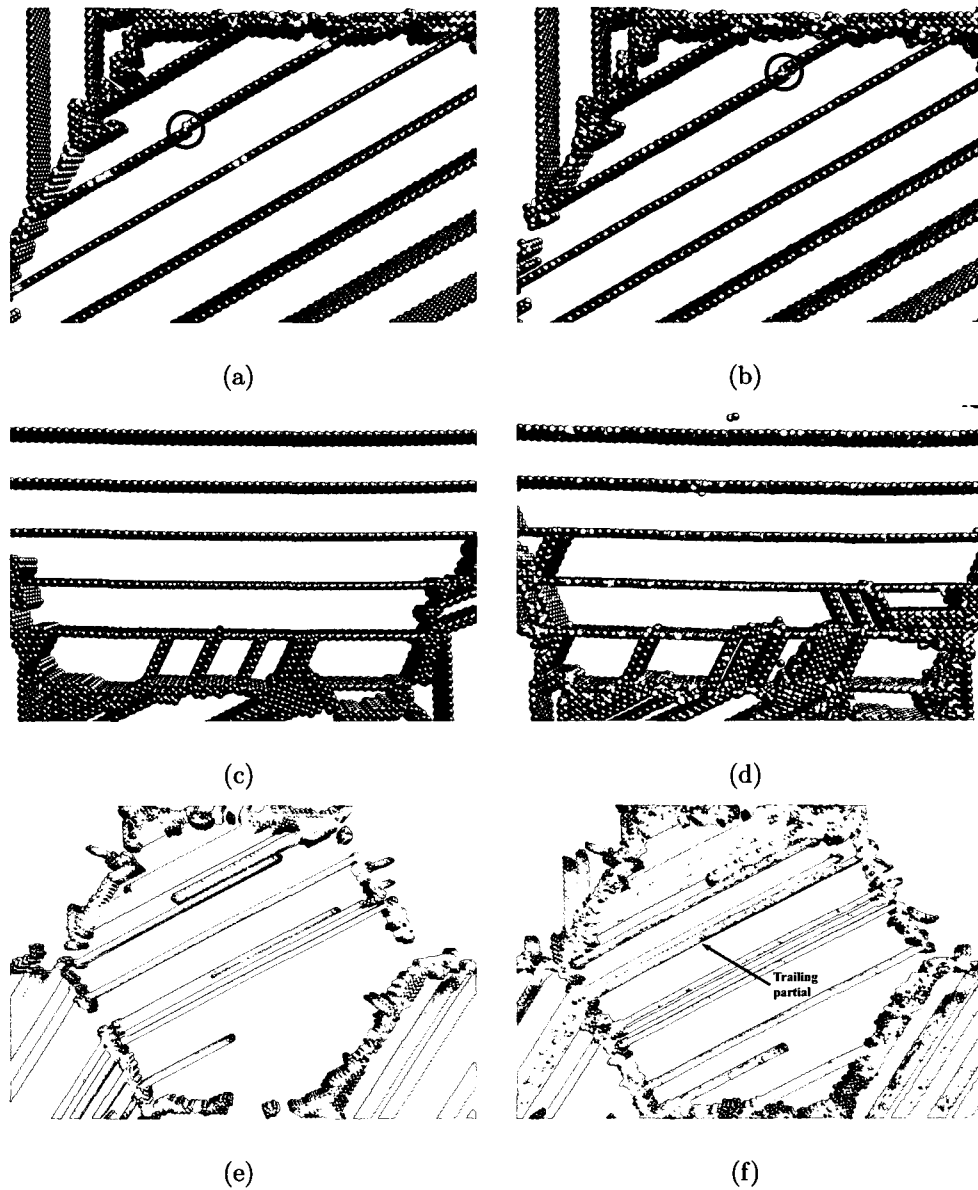


**Figure 5.6** Effect of temperature on various deformation processes of the nanotwinned model with twin spacing of 3nm. The snapshots presented in the left column are taken at 0K, whereas the ones in the right column are taken at 300K. (a) and (b) compare a TB migration process at 0K and 300K, respectively, after 24ps. The migration process of the second TB starts from the upper left side of the GB and is half way through at 0K, and almost complete at 300K. (c) and (d) are the snapshots taken in grain 1 at 132ps, showing early passing of the dislocations across the TB at higher temperature. (e) and (f) show the deformation state of grain 3 at 120ps. Higher number of dislocations are visible at 300K along with an emission of a trailing partial dislocation (the slipped perfect crystal is shown in red).

# Chapter 6

## Conclusions and Future Recommendations

### 6.1 Summary of conclusions

Nanotwinned materials are gaining interest among researchers and scientists, for both modeling and experiment, as they exhibit enhanced and unique mechanical properties which are highly desirable in many engineering applications. The purpose of this research was to develop a complete understanding of the underlying deformation mechanisms that govern the observed macroscopic properties of nanotwinned Cu. We used an atomistic simulation technique (Molecular Dynamics) to simulate a Cu nanotwinned material's response under approximately uniaxial tensile loading condition. Several nanotwinned models of 30nm grain size were constructed with various twin spacings, and their responses were compared with a model of the same grain size but without any nanotwins. The simulation cell was deformed by applying constant engineering strain rate, and the temperature was controlled by the Nosé-Hoover temperature thermostat. Two different visualization techniques, the centrosymme-

try parameter and the slip vector analysis, were used to characterize the nucleated defects. We analyzed the stress vs. strain response (both von Mises stress vs. strain and tensile stress vs. strain) of various models, and also examined the variation of maximum von Mises stress with twin width at various temperatures. The resolved shear stress analysis was performed in each grain to examine the variation of deformation behavior on various slip planes of different grains. We examined the toughness of various nanotwinned models, and also investigated the effects of twin width, grain orientation, and temperature on the microscopic deformation behaviors and properties, such as the strength and toughness, of these structures. Lastly, a detailed analysis was performed to examine an efficient way to refine the twin width and grain size that will help optimize both the strength and toughness of these materials. For property comparison, we considered several bigger grain nanotwinned models of 60nm diameter, and compared their responses with the smaller grain models (30nm diameter). In brief, the following conclusions can be drawn:

1. The GBs, triple junctions, and the intersection points of the TBs with the GBs are found to be the most probable sites for dislocation nucleation. Several interesting deformation mechanisms have been revealed including: extended partial dislocation emission from the GBs and TB/GB junctions, interaction of the partials with the TBs, twinning fault formation, TB migration, dislocation emission from the steps of the TBs, and grain boundary sliding.
2. The dominant deformation mode is determined by the generalized planar fault energy densities for various defects obtained from the EAM Cu potential used in this study. Both extended partial dislocation nucleation and TBM are found to be dominant mechanisms. However, the nucleation of a trailing partial forming a full dislocation is found to be a rare occurrence. Our observations are consistent

with the deformation theory of van Swygenhoven *et al.* [34] and Froseth *et al.* [46,47].

3. From the simulation results, we conclude that several dominating factors are contributing to the overall response of the models. At the initial deformation stages, strengthening is achieved in some grains when free dislocation movements are restricted by the TBs, while the free dislocation movements in other grains contribute to the ductility of the materials. Later, the strengthening effect reaches a maximum and falls off as an increased number of dislocations begin crossing the TBs.
4. The maximum von Mises stress values of various models are found to increase with decreasing twin spacing and decreasing temperature. The maximum tensile strengths of various models also exhibit a similar trend with twin spacing.
5. After resolving the global grain stresses into the two active slip planes we find that the deformation varies in different grains depending upon their orientation with respect to the loading direction. For each model, the grains oriented at  $0^\circ$  and  $90^\circ$  (orientations explained in the discussion of Figure 4.1) to the loading axis exhibit dominant deformations across the TBs, whereas, the grain oriented at  $60^\circ$  shows deformations mostly along the TBs. The overall response of each model depends upon the relative participation of each grain in the deformation processes.
6. Copper nanotwinned structures exhibit enhanced toughness with twin width refinement, and also at extremely low temperature. It has been revealed that free dislocation motion along the TBs in some grains is the primary contributor to the enhanced toughness of these materials. Moreover, depressed dislocation

activities, such as slower TB migration processes and limited dislocation movement, contribute to the enhanced toughness at low temperature. The simulation results also agree well with the experimental observations.

7. We propose a new concept of improved toughness: the anisotropic behavior of the grains along or across the TB means a polycrystalline nanotwinned structure acts like a “composite” material, such that grains allowing deformation predominantly along the TBs act as the “ductile phase”, while, the other grains exhibiting deformation across the TBs act as the “strengthening phase”. The random orientation of the grains ensures that both contribute to the overall mechanical response. This observation in our simplified system sheds light on the way real nanotwinned specimens achieve both strength and toughness.
8. A comprehensive study has also been carried out to reveal which refinement among the two, e.g., grain size or twin width, yields better properties for nanotwinned materials. Twin refinement has been found to enhance both strength and toughness, whereas more careful consideration has to be given to grain refinement, as it may deteriorate the material toughness. To optimize a nanotwinned material’s properties we also emphasize the appropriate selection of the grain orientations, as the dominant deformation modes in each grain (i.e., either along or across the TBs) may ultimately dictate the observed behaviors of the nanotwinned materials.

## 6.2 Future work

There exist a range of possible extensions of the present study to get further insight of the nanotwinned structures.

1. The structure of the simulation model investigated in this present study is essentially 2D. The short periodic length along the z-direction enforces dislocation glide only on two active slip planes- one along the TB and the other across the TB, with dislocation line parallel to the z-direction. Moreover, the limited number of grains in a periodic cell imposes constraints on the plasticity of the model. To get a more realistic picture it is thus important to extend this present work into a 3D model consists of a large number of randomly oriented grains. This would give an opportunity to compare the results with experimental observations. The 3D simulated structure can be built following the Voronoi algorithm, similar to that used by Froseth *et al.* [46]. The effect of other TB structures (such as semi-coherent or incoherent TBs) can also be investigated.
2. Another important aspect that should be addressed in future is to develop an analytical model that would accurately describe nanotwinned materials behavior. The existing twin boundary affected zone (TBAZ) model proposed by Dao *et al.* [18] and interfacial plasticity model proposed by Zhu *et al.* [20] address observed properties to some extent. Dao *et al.* propose a model where they incorporate the idea of soft and hard mode slip system (analogous to our along and across TB slip system), where the critical resolved shear stresses for the soft mode and the hard mode scale approximately with the grain size and inverse root of the twin lamellar spacing, respectively [18]. Therefore, we feel that the hardening law should consider the contributions arising from dislocations, GBs, and TBs, and can be written as

$$\tau = \tau_0 + \alpha\sqrt{\rho_{dis}} + \beta\sqrt{\rho_t} + \frac{\gamma}{\sqrt{d}}, \quad (6.1)$$

where the first term accounts for the lattice friction, the second term arises from dislocation density ( $\rho_{dis}$ ) or dislocation-dislocation interactions, the third

term arises due to dislocation interaction with the TBs or TB density ( $\rho_t$ ), and the fourth term arises due to the dislocation interaction with the GBs or the Hall-Petch relation.  $\alpha$ ,  $\beta$ , and  $\gamma$  are the proportionality constants. Equation 6.1 is similar to the model proposed by Wei *et al.* [84], except that the third term is added. This term signifies the dependence of strength on square root of the twin density or inverse root of the twin lamellar spacing via the Hall-Petch relationship. It is important to note that when the grain size/lamellae spacing is very small, the dislocation density inside the grain becomes insignificant and the second term can be ignored. However, the contributions arising from dislocation interaction both with the GBs and the TBs become dominant with the reduction in grain size/lamellae spacing.

To formulate a model incorporating ductility, Zhu *et al.* propose that the interfacial hardening rate due to dislocation interaction with the TBs controls the macroscopic strain hardening rate, that consequently delays the onset of necking, and leads to the improved ductility of the nanotwinned structures [20]. This means their proposed model attributes both the observed hardening and tensile ductility of the nanotwinned Cu samples to the interfacial/TB dislocation density ( $\rho_{int}$ ). In our simulations we observe that the density of accumulated dislocations against the TBs is higher for the higher twin density models. Hence,  $\rho_{int}$  seems to hold a similar relationship to the macroscopic hardening as the  $\rho_t$  in equation 6.1. In most of the earlier works, the contribution of the easy glide of dislocations along the TB has been neglected. However, our simulation results reveal that, in some grains (depending upon the orientation), a large fraction of the dislocations move along the TBs without experiencing any obstacle either from the TBs or from the other dislocations. Therefore, these dislocations have an important contribution to both strength and ductility of the nanotwinned

structures, and should be considered in formulating the analytical models. Here we want to emphasize that the mechanism of composite behavior of the nanotwinned structures, proposed on the basis of ‘bi-modal’ deformation behavior (both along and across the TBs) of variously oriented grains, is suggested by the results we have obtained from our simulations, and is only speculation at this point. Further study, especially on models with many more grains and with fully 3D character, are warranted before this observation can be definitive.

3. It is also important to conduct experimental research to validate the findings from computer simulations. Although our simulation results agree reasonably well with the experimental findings of other workers, the present work should be extended to experiments involving different materials, sample sizes, and loading types. But there exist several factors that make direct quantitative comparison between simulation and experiment difficult. Simulations are done in a more idealized condition and at a very high strain rate, which is unrealistic in a physical sense, but inherent to every MD simulation. In reality, the experimental loading rates are several magnitudes (7-12) lower than that of the simulations. The nanoscale sample preparation is complex by nature, and the experimental samples are often populated with many pre-existing defects (such as dislocations, voids, pores etc.), which may lead to some unexpected behavior of materials. The simulation samples are free from any such defect. On the other hand, the validity of the simulations depends a lot more on the availability and accuracy of the interatomic potentials. The sample size also has a significant impact on the results. As mentioned earlier, the experimental nanotwinned grain size ranges from 400 to 600 nm, which is almost 10-20 times larger than the simulated grains. This requires tremendous computing capabilities to simulate materials behavior in that size scale range. Therefore, we always have to be careful in

interpreting the results, and the availability of experimental results may only help making qualitative comparison between simulations and experiments.

These proposed enhancements will not only solidify our understanding of the physics behind the unique characteristics of the nanotwinned structures, but also shed light on the potential engineering applications of this new class of material.

# Appendix A

## Conjugate gradient (CG) energy minimization

It is often necessary to perform an energy minimization of an atomic/molecular system during a MD simulation to compute the equilibrium configuration of the atoms/molecules. The idea behind this energy minimization is to obtain a stable state of the system that corresponds to a local minimum of its potential energy. The energy minimization generally begins from an arbitrary configuration of atoms, then an iterative procedure of optimization allows the atoms to move in a way that reduces the net forces (the gradients of potential energy) to nearly zero. Energy minimization does not consider the effect of temperature, and only the final state of the system that corresponds to a local minimum of potential energy is obtained, instead of atomic trajectories. Therefore, this final state of the system corresponds to the configuration of atoms at zero temperature.

The conjugate gradient energy minimization algorithm proceeds by adding an orthogonal vector to the direction of search, and then moves in an another direction nearly perpendicular to this vector [57,85]. Let us consider an arbitrary initial vector

$\mathbf{g}_0$  or the net force on atoms,  $\mathbf{F}(\mathbf{x}_i)$ , that can be calculated as the negative gradient of total potential energy ( $V$ ) of system as follows

$$\mathbf{g}_0 = \mathbf{F}(\mathbf{x}_i) = \frac{-\partial}{\partial \mathbf{x}_i} V$$

Also consider,  $\mathbf{h}_0$  is an initial search direction such that  $\mathbf{h}_0 = \mathbf{g}_0$ . The vectors satisfy the following orthogonality and conjugacy conditions

$$\text{for } i \neq j$$

$$\mathbf{g}_i \cdot \mathbf{g}_j = 0$$

$$\mathbf{h}_i \cdot \mathbf{A} \cdot \mathbf{h}_j = 0$$

$$\mathbf{g}_i \cdot \mathbf{h}_j = 0$$

where matrix  $\mathbf{A}$  is called 'Hessian matrix' whose components are the second partial derivative of the function  $V$  at a particular point  $P$ ,  $[A_{ij}] = \frac{\partial^2 V}{\partial x_i \partial x_j} |_P$ .  $\lambda_i$  and  $\gamma_i$  are two scalars and given by

$$\lambda_i = \frac{\mathbf{g}_i \cdot \mathbf{g}_i}{\mathbf{h}_i \cdot \mathbf{A} \cdot \mathbf{h}_i}$$

$$\gamma_i = \frac{\mathbf{g}_{i+1} \cdot \mathbf{g}_{i+1}}{\mathbf{g}_i \cdot \mathbf{g}_i}$$

$\lambda_i$  signifies how far to move in current search direction, whereas,  $\gamma_i$  signifies how much of the previous search direction to consider in the new search direction. With the current search direction and the value of  $\lambda_i$  the next point  $\mathbf{x}_{i+1}$  and vector  $\mathbf{g}_{i+1}$  are calculated as follows

$$\mathbf{x}_{i+1} = \mathbf{x}_i + \lambda_i \mathbf{h}_i$$

$$\mathbf{g}_{i+1} = \mathbf{g}_i - \lambda_i \mathbf{A} \cdot \mathbf{h}_i$$

If  $\mathbf{g}_{i+1}$  is sufficiently small then the minimization stops and the result is  $\mathbf{x}_{i+1}$ . Otherwise, new search direction is computed using the value of  $\mathbf{g}_{i+1}$  and  $\gamma_i$  as

$$\mathbf{h}_{i+1} = \mathbf{g}_{i+1} + \gamma_i \mathbf{h}_i.$$

# Appendix B

## Velocity initialization algorithm

Before starting the actual dynamics, it is necessary to bring the system to a state of thermal equilibrium at a finite temperature, say  $T = 300K$ , such that the distribution of initial atom velocities satisfies the Maxwell-Boltzmann law [57, 62]

$$f(\mathbf{v}) = \frac{1}{Z_v} \exp\left(-\frac{p^2}{2m_i k_B T}\right) = \frac{1}{Z_v} \exp\left(-\frac{m_i |\mathbf{v}_i|^2}{2k_B T}\right), \quad (\text{B.1})$$

where  $Z_v$  is the partition function,  $k_B$  is the Boltzmann constant. It is a Gaussian distribution with standard deviation  $\sigma = (k_B T / m_i)^{1/2}$  about the mean value of  $\langle v \rangle = 0$  [62]. This equation signifies that the average number of atoms having momenta within  $\mathbf{p}$  to  $\mathbf{p} + d\mathbf{p}$  (irrespective of their positions) is  $N(\mathbf{p})d\mathbf{p}$ , and the fraction of atoms having velocities between  $\mathbf{v}$  and  $\mathbf{v} + d\mathbf{v}$  is  $f(\mathbf{v})$ . However, this velocity initialization may not yield the prescribed temperature of the state at thermal equilibrium. Therefore, MD algorithm often applies a velocity rescaling technique to match the instantaneous temperature,  $T_{inst}$ , of the system with the desired temperature,  $T$ . The  $T_{inst}$  is calculated as

$$T_{inst} = \frac{2}{3Nk_B} E_{kin} = \frac{2}{3Nk_B} \sum_{i=1}^N \frac{1}{2} m_i |\mathbf{v}_i|^2, \quad (\text{B.2})$$

where  $E_{kin}$  is the total kinetic energy of the system, and the rest of symbols have their usual meaning [57]. If  $T_{inst}$  differs from  $T$  then the velocities of all the atoms are rescaled as  $\mathbf{v}_i = \mathbf{v}_i \sqrt{T/T_{inst}}$  for  $(i = 1, \dots, N)$ , and the rescaling procedure is repeated until a match is found.

# Appendix C

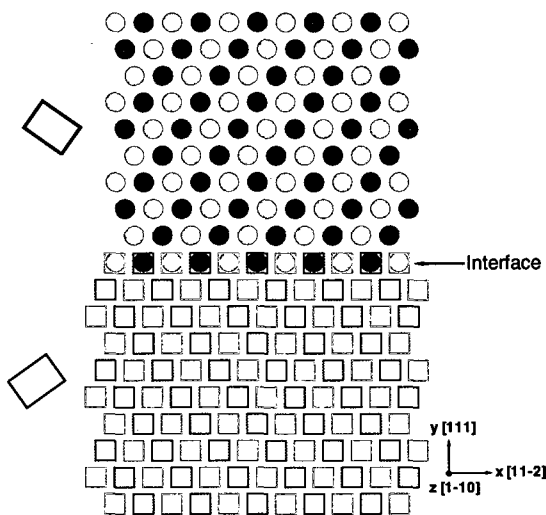
## Coincident site lattice (CSL)

In most cases GBs are disordered structures. However, there exist certain boundaries that have special properties, such as low energy and special crystallography. These special boundaries are formed when a crystal is rotated with respect to the other to certain angle that brings a finite fraction of the lattice sites of these two crystals coincide. The lattice thus formed is known as coincident site lattice (CSL). The more of the lattice points coincide, it is expected that the boundary thus formed between these two crystals is more ordered than the general boundaries. It is important to clarify that, in reality the lattice sites do not actually overlap, rather both crystals share common lattice points at the boundary. Figure C.1(a) shows an example where the rotation of one crystal with respect to the other results in a twin boundary at the interface. The unit cells of the crystals are shown by the black boxes in the figure. An easy way to visualize the CSL is to extend both crystals infinitely, and superimpose the lattice points on top of each other. Figure C.1(b) presents one such example where two crystals shown in Figure C.1(a) are extended infinitely on the x-y plane, and superimposed on top of each other. The circular points belong to one crystal, and the squared points belong to the other crystal. The color of the points (blue

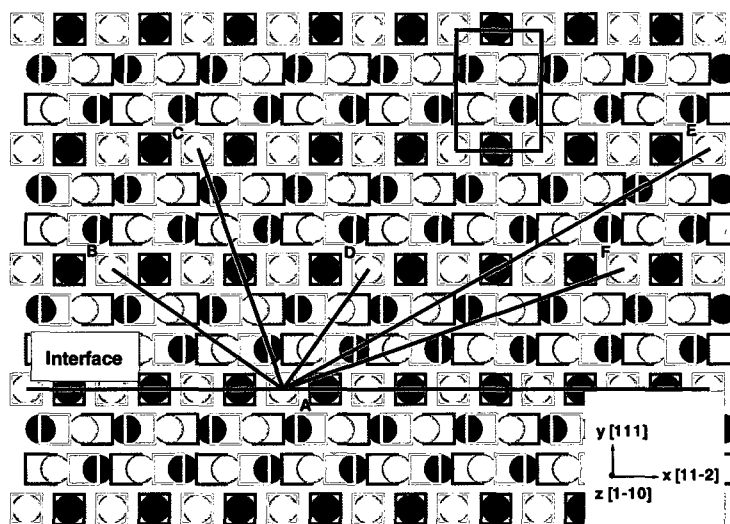
---

or green) varies in order to differentiate their positions on different x-y planes, and the same colored points (either circle or square) are located on the same (110) plane along the z-direction.

$\Sigma N$  is a measure of density of the coincident lattice points in a CSL, and defined as the ratio of the areas enclosed by the unit cell of the CSL (as shown by the black box in Figure C.1(b)) and the unit cell of the crystals forming the CSL. The value of this ratio of the boundary shown in Figure C.1(a) is 3, and therefore, it is known as a  $\Sigma = 3$  type boundary. Another way to measure  $\Sigma$  is to move from one coincident point (*A*) towards any particular direction, and the next coincident point (either *B*, *C*, *D*, *E*, or *F*) can be found after every certain number of atoms, which is the value of  $\Sigma$  (3 in this case). Moreover, after every 3 {111} atomic layers, atoms of both the crystals completely coincide with each other, and form a common interface. A boundary with higher  $\Sigma$  is expected to have a higher energy than the one with lower  $\Sigma$ .



(a)



(b)

**Figure C.1** (a) Two crystals forming a  $\Sigma = 3$  twin boundary at the interface. The unit cells of the crystals are shown by the black boxes. The same colored atoms (either blue or green) are located on the same plane along the  $z$ -direction. (b) The two crystals shown in (a) are extended in the  $x$ - $y$  plane and superimposed on top of each other, forming a coincident site lattice (CSL). From any coincident lattice point  $A$  in the CSL, the next overlapped point (either  $B$ ,  $C$ ,  $D$ ,  $E$ , or  $F$ ) can be found after every 3 atoms in that direction. Also after every 3  $\{111\}$  atomic layers, atoms of the both crystals coincide completely with each other.

# Bibliography

- [1] Yury Gogotsi, editor. *Nanomaterials handbook*. Taylor and Francis, Florida, 2006.
- [2] Yuntian T. Zhu. Deformation twinning in nanocrystalline metals. *Journal of Materials Engineering and Performance*, 14(4):467–472, 2005.
- [3] Z. Shan, E.A. Stach, J.M. Wiezorek, J.A. Knapp, D.M. Follstaedt, and S.X. Mao. Grain boundary-mediated plasticity in nanocrystalline nickel. *Science*, 305(5684):654–657, 2004.
- [4] X.Z. Liao, F. Zhou, E.J. Lavernia, S.G. Srinivasan, M.I. Baskes, D.W. He, and Y.T. Zhu. Deformation mechanism in nanocrystalline Al: Partial dislocation slip. *Appl. Phys. Lett.*, 83(4):632–634, 2003.
- [5] X.Z. Liao, F. Zhou, E.J. Lavernia, D.W. He, and Y.T. Zhu. Deformation twins in nanocrystalline Al. *Appl. Phys. Lett.*, 83(24):5062–5064, 2003.
- [6] J. Schiotz, T. Vegge, and K.W. Jacobsen. Atomic-scale modeling of the deformation of nanocrystalline metals. *Mat. Res. Soc. Symp. Proc.*, 538:299–308, 1999.
- [7] J. Schiotz, Francesco D. Di Tolla, and K.W. Jacobsen. Softening of nanocrystalline metals at very small grain sizes. *Nature*, 391(6667):561–563, 1998.

- 
- [8] D. Wolf, V. Yamakov, S.R. Phillpot, and A.K. Mukherjee. Deformation mechanism and inverse Hall-Petch behavior in nanocrystalline materials. *Zeitschrift fur Metallkunde*, 94(10):1091–1097, 2003.
- [9] Helena Van Swygenhoven. Grain boundaries and dislocations. *Science*, 296(5565):66–67, 2002.
- [10] H. Van Swygenhoven, A. Caro, and D. Farkas. A molecular dynamics study of polycrystalline fcc metals at the nanoscale: Grain boundary structure and its influence on plastic deformation. *Materials Science and Engineering A*, 309-310:440–444, 2001.
- [11] K.W. Jacobsen and J. Schiotz. Computational materials science: Nansoscale plasticity. *Nature Materials*, 1(1):15–16, 2002.
- [12] R. Valiev. Materials science:Nanomaterial advantage. *Nature*, 419:887–889, 2002.
- [13] D. Hull and D.J. Bacon. *Introduction to dislocations*. Pergamon press, New York, third edition, 1984.
- [14] John P. Hirth and Jens Lothe. *Theory of Dislocations*. John Wiley and Sons, New York, second edition, 1982.
- [15] Y.M. Wang, M.W. Chen, F.H. Zhou, and E. Ma. High tensile ductility in a nanostructured metal. *Nature*, 419(6910):912–915, 2002.
- [16] R.Z. Valiev, I.V. Alexandrov, Y.T. Zhu, and T.C. Lowe. Paradox of strength and ductility in metals processed by severe plastic deformation. *J. Mater. Res.*, 17(1):5–8, 2002.

- [17] L. Lu, R. Schwaiger, Z.W. Shan, M. Dao, K. Lu, and S. Suresh. Nano-sized twins induce high rate sensitivity of flow stress in pure copper. *Acta Mat.*, 53(7):2169–2179, 2005.
- [18] M. Dao, L. Lu, Y.F. Shen, and S. Suresh. Strength, strain-rate sensitivity and ductility of copper with nanoscale twins. *Acta Mat.*, 54(20):5421–5432, 2006.
- [19] Y.F. Shen, L. Lu, Q.H. Lu, Z.H. Jin, and K. Lu. Tensile properties of copper with nano-scale twins. *Scripta Materialia*, 52(10):989–994, 2005.
- [20] Ting Zhu, Ju Li, Amit Samanta, Hyoun Gyu Kim, and Subra Suresh. Interfacial plasticity governs strain rate sensitivity and ductility in nanostructured metals. *Proceedings of the National Academy of Sciences of the United States of America*, 104(9):3031–3036, 2007.
- [21] Lei Lu, Yongfeng Shen, Xianhua Chen, Lihua Qian, and K. Lu. Ultrahigh strength and high electrical conductivity in copper. *Science*, 304(5669):422–426, 2004.
- [22] D. Srivastava and S.N. Atluri. Computational nanotechnology: A current perspective. *Computer Modeling in Engineering and Sciences*, 3(5):531–538, 2002.
- [23] J. Hafner. Atomic-scale computational materials science. *Acta Mat.*, 48(1):71–92, 2000.
- [24] A.F. Voter. Interatomic potentials for atomistic simulations. *MRS bulletin*, 21(2):17–19, 1996.
- [25] T.D. de la Rubia and V.V. Bulatov. Materials research by means of multiscale computer simulation. *MRS bulletin*, 26(3):169–170, 2001.

- 
- [26] Dieter W. Heermann. *Computer simulation methods in theoretical physics*. Springer-Verlag, Germany, 1986.
- [27] Ishraq Shabib and Ronald E. Miller. Deformation characteristics and stress-strain response of nanotwinned copper via molecular dynamics simulation. *Acta Mat.*, 57, 2009.
- [28] I. Shabib and R. E. Miller. Molecular dynamics study of twin width, grain size and temperature effects on the toughness of 2D-columnar nanotwinned copper. *Modeling Simul. Mater. Sci. Eng.*, 17:055009, 2009.
- [29] Jr. William D. Callister. *Materials science and engineering : an introduction*. John Wiley, Hoboken, N.J., 7th edition, 2007.
- [30] V. Yamakov, D. Wolf, S.R. Phillpot, and H. Gleiter. Dislocation-dislocation and dislocation-twin reactions in nanocrystalline Al by molecular dynamics simulation. *Acta Materialia*, 51(14):4135–4147, 2003.
- [31] Yulin Lu and Peter K. Liaw. The mechanical properties of nanostructured materials. *JOM*, 53(3):31–35, 2001.
- [32] M.A. Meyers, A. Mishra, and D.J. Benson. Mechanical properties of nanocrystalline materials. *Progress in Materials Science*, 51(4):427–556, 2006.
- [33] M.A. Meyers and E. Ashworth. A model for the effect of grain size on the yield stress of metals. *Phil. Mag. A*, 46(5):737–759, 1982.
- [34] H. Van Swygenhoven, P.M. Derlet, and A.G. Froseth. Stacking fault energies and slip in nanocrystalline metals. *Nature materials*, 3(6):399–403, 2004.

- [35] H. Van Swygenhoven, A. Caro, and D. Farkas. Grain boundary structure and its influence on plastic deformation of polycrystalline fcc metals at the nanoscale: a molecular dynamics study. *Scripta Materialia*, 44(8-9):1513–1516, 2001.
- [36] G.J. Fan, H. Choo, P.K. Liaw, and E.J. Lavernia. A model for the inverse hall-petch relation of nanocrystalline materials. *Mater. Sci. Eng. A*, 409(1-2):243–248, 2005.
- [37] C.E. Carlton and P.J. Ferreira. What is behind the inverse Hall-Petch effect in nanocrystalline materials? *Acta Mat.*, 55(11):3749–3756, 2007.
- [38] H.W. Song, S.R. Guo, and Z.Q. Hu. A coherent polycrystal model for the inverse Hall-Petch relation in nanocrystalline materials. *Nanostructured Materials*, 11(2):203–210, 1999.
- [39] Y.M. Wang and E. Ma. Temperature and strain rate effects on the strength and ductility of nanostructured copper. *Applied Physics Letters*, 83(15):3165–3167, 2003.
- [40] Yinmin Wang, En Ma, Ruslan Z. Valiev, and Yuntian Zhu. Tough nanostructured metals at cryogenic temperatures. *Advanced Materials*, 16(4):328–331, 2004.
- [41] E. Ma, Y.M. Wang, Q.H. Lu, M.L. Sui, L. Lu, and K. Lu. Strain hardening and large tensile elongation in ultrahigh-strength nano-twinned copper. *Applied Physics Letters*, 85(21):4932–4934, 2004.
- [42] Y.M. Wang and E. Ma. Strain hardening, strain rate sensitivity, and ductility of nanostructured metals. *Materials science and engineering A*, A375-A377:46–52, 2004.

- [43] H. Van Swygenhoven and A. Caro. Plastic behavior of nanophase metals studied by molecular dynamics. *Phys. Rev. B*, 58(17):11246–11251, 1998.
- [44] Robert J. Asaro and Subra Suresh. Mechanistic models for the activation volume and rate sensitivity in metals with nanocrystalline grains and nano-scale twins. *Acta Mat.*, 53(12):3369–3382, 2005.
- [45] K. Konopka, J. Mizera, and J.W. Wyrzykowski. The generation of dislocations from twin boundaries and its effect upon the flow stresses in FCC metals. *Journal of Materials Processing Technology*, 99(1-3):255–259, 2000.
- [46] A. Froseth, H. Van Swygenhoven, and P.M. Derlet. The influence of twins on the mechanical properties of nc-Al. *Acta Materialia*, 52(8):2259–2268, 2004.
- [47] A.G. Froseth, P.M. Derlet, and H. Van Swygenhoven. Grown-in twin boundaries affecting deformation mechanisms in nc-metals. *Applied Physics Letters*, 85(24):5863–5865, 2004.
- [48] A.J. Cao and Y.G. Wei. Molecular dynamics simulation of plastic deformation of nanotwinned copper. *J. Appl. Phys.*, 102(8):083511–1–5, 2007.
- [49] V. Yamakov, D. Wolf, S.R. Phillpot, A. K. Mukherjee, and H. Gleiter. Dislocation processes in the deformation of nanocrystalline aluminium by molecular-dynamics simulation. *Nat. Mater.*, 1(1):45–48, 2002.
- [50] S. M. Foiles, M. I. Baskes, and M. S. Daw. Embedded-atom-method functions for the FCC metals Cu, Ag, Au, Ni, Pd, Pt, and their alloys. *Phys. Rev. B*, 33(12):7983–7991, 1986.
- [51] H. Foll. Thompson tetrahedra. [http://www.tf.uni-kiel.de/matwis/amat/def\\_en/kap\\_5/illustr/i5\\_4\\_5.html](http://www.tf.uni-kiel.de/matwis/amat/def_en/kap_5/illustr/i5_4_5.html).

- [52] Z.-H. Jin, P. Gumbsch, E. Ma, K. Albe, K. Lu, H. Hahn, and H. Gleiter. The interaction mechanism of screw dislocations with coherent twin boundaries in different face-centred cubic metals. *Scripta Materialia*, 54(6):1163–1168, 2006.
- [53] A.G. Froseth, P.M. Derlet, and H. Van Swygenhoven. Vicinal twin boundaries providing dislocation sources in nanocrystalline Al. *Scripta Materialia*, 54(3):477–481, 2006.
- [54] Rob Phillips. *Crystals, defects and microstructures : modeling across scales*. Cambridge University Press, Cambridge, UK, 2001.
- [55] A. Nakano, M.E. Bachlechner, T.J. Campbell, R.K. Kalia, A. Omeltchenko, K. Tsuruta, P. Vashishta, S. Ogata, I. Ebbsjo, and A. Madhukar. Atomistic simulation of nanostructured materials. *IEEE computational science and engineering*, 5(4):68–78, 1998.
- [56] L.E. Shilkrot, R.E. Miller, and W.A. Curtin. Multiscale plasticity modeling: coupled atomistics and discrete dislocation mechanics. *J. Mech. Phys. Sol.*, 52(4):755–787, 2004.
- [57] Vasily V. Bulatov and Wei Cai. *Computer simulations of dislocations*. Oxford University Press, New York, 2006.
- [58] Ishraq Shabib. Multiscale modeling of the indentation of Ni-Al nanolayers. Master's thesis, Carleton University, Canada, 2005.
- [59] Ronald E. Miller. *On the generalization of continuum models to include atomistic features*. PhD thesis, Brown University, 1998.

- [60] M. S. Daw and M. I. Baskes. Embedded-atom method: Derivation and application to impurities, surfaces, and other defects in metals. *Phys. Rev. B*, 29:6443–6453, 1984.
- [61] M. S. Daw and M. I. Baskes. Semiempirical, quantum mechanical calculation of hydrogen embrittlement in metals. *Phys. Rev. Lett.*, 50(17):1285–1288, 1983.
- [62] J.M. Haile. *Molecular dynamics simulation: elementary methods*. John Wiley and sons, New York, 1992.
- [63] Ma Xinling and Yang Wei. MD simulation for nanocrystals. *Acta Mechanica Sinica*, 19(6):485–507, 2003.
- [64] YanJuan Zhao. Testing a criterion for dislocation nucleation using molecular dynamics simulations of nano-indentation. Master’s thesis, Carleton University, Canada, 2005.
- [65] Shuichi Nosé. A unified formulation of the constant temperature molecular dynamics methods. *J. Chem. Phys.*, 81(1):511–519, 1984.
- [66] William G. Hoover. Canonical dynamics: Equilibrium phase-space distributions. *Phys. Rev. A*, 31(3):1695–1697, 1985.
- [67] Daan Frenkel and Berend Smit. *Understanding molecular simulation: From algorithms to applications*. Academic press limited, San Diego, CA, 1996.
- [68] G.J. Martyna, M.E. Tuckerman, D.J. Tobias, and M.L. Klein. Explicit reversible integrators for extended systems dynamics. *Molecular Physics*, 87(5):1117–1157, 1996.

- [69] C.L. Kelchner, S.J. Plimpton, and J.C. Hamilton. Dislocation nucleation and defect structure during surface indentation. *Phys. Rev. B*, 58(17):11085–11088, 1998.
- [70] J.A. Zimmerman, C.L. Kelchner, P.A. Klein, J.C. Hamilton, and S.M. Foiles. Surface step effects on nanoindentation. *Phys. Rev. Lett.*, 87(16):165507/1–165507/4, 2001.
- [71] Denis Saraev and Ronald E. Miller. Atomic-scale simulations of nanoindentation-induced plasticity in copper crystals with nanometer-sized nickel coatings. *Acta Materialia*, 54(1):33–45, 2006.
- [72] Ju Li. Atomeye: an efficient atomistic configuration viewer. *Modeling Simul. Mater. Sci. Eng.*, 11(2):173–177, 2003.
- [73] U. Wolf, F. Ernst, T. Muschik, M. W. Finnis, and H.F. Fischmeister. The influence of grain boundary inclination on the structure and energy of  $\Sigma = 3$  grain boundaries in copper. *Phil. Mag. A*, 66(6):991–1016, 1992.
- [74] N. Takata, K. Ikeda, F. Yoshida, H. Nakashima, and H. Abe. Grain boundary structure and its energy of  $\langle 110 \rangle$  symmetric tilt boundary in copper. *Materials Science Forum*, 467-470:807–812, 2004.
- [75] Frank Ernst, Michael W. Finnis, Ansgar Koch, Camilla Schmidt, Boris Straumal, and Wolfgang Gust. Structure and energy of twin boundaries in copper. *Zeitschrift fuer Metallkunde*, 87(11):911–922, 1996.
- [76] C. Schmidt, M.W. Finnis, F. Ernst, and V. Vitek. Theoretical and experimental investigations of structures and energies of  $\Sigma = 3$ ,  $[112]$  tilt grain boundaries in copper. *Phil. Mag. A*, 77(5):1161–1184, 1998.

- [77] N. Chandra and P. Dang. Atomistic simulation of grain boundary sliding and migration. *Journal of Materials Science*, 34(4):655–666, 1999.
- [78] Jonathan A. Zimmerman, Huajian Gao, and Farid F. Abraham. Generalized stacking fault energies for embedded atom FCC metals. *Modeling Simul. Mater. Sci. Eng.*, 8(2):103–116, 2000.
- [79] S. Plimpton. Fast parallel algorithms for short-range molecular dynamics. *Journal of Computational Physics*, 117(1):1–19, 1995.
- [80] V. Vitek and T. Egami. Atomic level stresses in solids and liquids. *Phys. Stat. Sol. B*, 144:145–156, 1987.
- [81] M.F. Horstemeyer, M.I. Baskes, and S.J. Plimpton. Length scale and time scale effects on the plastic flow of fcc metals. *Acta Mat.*, 49:4363–4374, 2001.
- [82] Ajing Cao and Yueguang Wei. Atomistic simulations of the mechanical behavior of fivefold twinned nanowires. *Phys. Rev. B*, 74:214108–1–214108–7, 2006.
- [83] L. Lu, X. Chen, X. Huang, and K. Lu. Revealing the maximum strength in nanotwinned copper. *Science*, 323(5914):607–610, 2009.
- [84] Q. Wei, S. Cheng, K.T. Ramesh, and E. Ma. Effect of nanocrystalline and ultrafine grain sizes on the strain rate sensitivity and activation volume: fcc versus bcc metals. *Materials science and engineering A*, 381:71–79, 2004.
- [85] William H. Press, Saul A. Teukolsky, William T. Vetterling, and Brian P. Flannery, editors. *Numerical recipes in Fortran: The Art of scientific computing*. Cambridge University Press, New Delhi, 1994.